COMPARATIVE ANALYSIS OF FINNED-TYPE LIQUID-COOLED POWER ELECTRONIC MODULES FOR ELECTRIFIED TRANSPORTATION

COMPARATIVE ANALYSIS OF FINNED-TYPE

LIQUID-COOLED POWER ELECTRONIC MODULES FOR

ELECTRIFIED TRANSPORTATION

BY

SEYED SOBHAN KASHFI, B.Sc.

A THESIS

SUBMITTED TO THE DEPARTMENT OF MECHANICAL ENGINEERING

AND THE SCHOOL OF GRADUATE STUDIES

OF MCMASTER UNIVERSITY

IN PARTIAL FULFILMENT OF THE REQUIREMENTS

FOR THE DEGREE OF

MASTER OF APPLIED SCIENCE

Master of Applied Science (2021)   McMaster University

(mechanical engineering)   Hamilton, Ontario, Canada

TITLE: Comparative Analysis of Finned-type Liquid-cooled

Power Electronic Modules for Electrified Transportation

AUTHOR: Seyed Sobhan Kashfi

B.Sc. (Mechanical Engineering),

Sharif University Of Technology, Tehran, Iran

SUPERVISOR: Dr. Ali Emadi

NUMBER OF PAGES: xv, 180

To Iman and Mehdi,

and the beautiful lives who perished in the downing of flight PS752

Abstract

Aggressive demands for high power density and low-cost power modules in the auto-motive sector pose significant challenges to the thermal management systems. These challenges necessitate adopting highly effective cooling technologies in power modules to remain competitive in the semiconductor industry. Furthermore, the thermal management strategy must be simple, easy to integrate, compact, effective, efficient, reliable, and economical.

This thesis is an effort to investigate the impact of fin geometry on the overall performance of finned-type liquid-cooled power electronic modules in electrified transportation. The cooling system's performance metrics, including thermal resistance, pressure drop, pumping power, and mass, are discussed in depth. Various cooling technologies are benchmarked. The finned-type cooling technique is chosen over other methods due to simplicity and low pressure drop. Integrated cooling or direct cooling of the module's baseplate is selected due to considerable thermal resistance reduction because of thermal grease elimination. Potential fabrication techniques are thoroughly explored and compared in terms of mass production and prototyping suitability.

Four different fin shapes, including circular (baseline), drop-shaped, symmetric convex lens, and offset strip in the staggered arrangement, are studied herein. The

cooling agent is Water and Ethylene Glycol 50% volumetric mixture (WEG 50%). Typical operating conditions in electrified vehicles (EVs) such as flow rate and inlet temperature are assumed for the numerical analysis. A grid convergence study is carried out to ensure numerical solutions are within an acceptable error band.

The thermal performance evaluation results showed that, on average, offset strip, drop-shaped, and the convex lens performed 39%, 20%, and 6% better than the baseline design, respectively. Additionally, the design candidates are compared in terms of mass and estimated machining cost. The results of the baseline case are verified against empirical correlations from the literature. The maximum deviation is less than 1% and 1.2% for finned-surface temperature and pressure drop, respectively. The difference is attributed to the end-wall effects.

Acknowledgements

I want to sincerely thank my supervisor Dr. Ali Emadi for his trust, encouragement, constant support, and mentorship throughout my graduate studies. The completion of this thesis would have been impossible without his help. It has been a great honor to work with Dr. Emadi and his amazing team at McMaster Automotive Resource Centre (MARC).

I am grateful to Dr. Romina Rodriguez for her precious time and valuable suggestions on improving the thesis's layout.

I want to thank Dr. John Reimers and Silvio Rotilli Filho, whom I collaborated with in different industrial projects. I also want to particularly thank Ahoora Bahrami and, Hasan Aleian who generously provided significant insight into the electrical modeling and power loss calculation. I want to thank my dearest friend and partner Helia Jamali for reading and providing feedback along the way of completing this thesis. I want to thank all of my friends and colleagues at MARC who made my graduate studies an incredible journey.

Finally, a special thank goes to my family and my dearest parents for their endless support, care, and love throughout my entire life.

Contents

List of Figures

List of Tables

Chapter 1

Introduction

1.1 Background and Motivations

About two-thirds of the world's electrical power is converted to mechanical power by electrical motors for which AC power is needed. Most of the renewable energies can generate power in the form of DC supply [1]. Therefore, DC-to-AC power conversion is required to run AC motors. Power conversion has a broad range of applications in various industries ranging from aerospace, marine, residential, and data centers to the mobility sector. Electric machines and power electronics are some key enablers of sustainable transportation. Due to the increasing concerns regarding Green House Gas (GHG) emissions and their environmental repercussions, fossil-based fuels and Internal Combustion Engine (ICE) vehicles are losing dominance. Sales of ICE passenger vehicles peaked in 2017 and are in decline since then [2]. The most modern ICEs have peak efficiencies around 30-35% at the most. Thus, not only a significant amount of emissions are generated by these engines, but also their inefficient energy consumption causes rapid consumption of energy resources.

It was not until two decades ago that power electronics found their way into automobiles [3]. Although fully-electric vehicles are conceived as the future of mobility, a transitional period must have been considered to allow for the adaptation of grid infrastructure. First, Hybrid Electric Vehicles (HEVs) were introduced. These vehicles had a higher overall powertrain efficiency and reduced emissions. Later, Plug-in Hybrid Electric Vehicles (PHEVs) and Battery Electric Vehicles (BEVs), with higher electrification levels, facilitated the transition towards sustainable transportation. Governmental incentives for electrified vehicles (EVs) market and penalties for fleets with high fuel economy and high CO_2 emissions are some of the driving forces of the paradigm shift. It is projected that by 2040, EVs make up more than 35% of the passenger vehicle market [2]. The aforementioned facts signify the importance of the electrified vehicles' market and its tremendous potential for the semiconductor industry.

There are multiple power converters at the heart of every electrified drivetrain, such as traction inverters and DC-DC converters. Stringent power density and cost targets are being defined for power electronic systems in automotive applications regularly. For instance, the U.S. Department of Energy (DOE) has defined power density and cost targets of 100kW/L and \$2.7/kW (for 100 000 units), respectively, for 2025. Further integration of the inverter sub-components is one of the potential strategies for achieving this target [4]. Achieving the targets is unfeasible without major technological breakthroughs in thermal management and packaging of the switching devices [5]. As power electronics become tightly integrated and smaller in size, advanced thermal management systems (TMS) are required to remove the system's heat effectively. In fact, many failure modes of power electronics are attributed to

mechanical stresses caused by high temperature and thermal cycling [6]. Therefore, the development of reliable, cost-effective, compact power electronics is primarily held back by packaging and TMS. Power electronics can be packaged in discrete devices or modules. Both discrete packages and power modules have been used in automotive applications. The focus of the current study is on module-level TMS.

High-Heat-Flux (HHF) heat removal technologies have received significant attention as the semiconductor industry continues to push heat flux boundaries. Although considerable progress has been made over the past decades, HHF removal still poses significant challenges in the thermal management of power electronics [7]. This is mainly because power density targets are often accompanied by aggressive cost targets in the automotive industry. For example, when comparing DOE targets for 2025 with that of 2020, power density increased 87%, and the cost has reduced 18 % [4]. According to DOE 2025 roadmap, the power module's cooling strategy must be chosen in a way that is compatible with other vehicle thermal strategies and has high effectiveness without decreasing the overall efficiency. Therefore, further investigation of existing cooling technologies is necessary to opt for efficient, inexpensive, and simple cooling solutions. Though passive two-phase cooling has shown high heat transfer capability, the added complexity and cost of additional components such as a condenser is not justifiable. Other cooling solutions such as liquid-cooling microchannel heatsinks have the downside of high pressure drop/pumping power; thus, the overall efficiency may be compromised. Finned-type liquid-cooling heatsinks are simple, effective, and easily implementable. However, the design of these heatsinks has been mostly confined to circular pin-fins. Other geometry configurations can be further evaluated and optimized for better thermal-hydraulic performance, mass, and cost.

Integrated liquid-cooling of the power module has shown promise as a simple and effective cooling solution. For instance, Wang et al. have demonstrated that junction to heatsink thermal resistance can be reduced by more than 50% due to eliminating the thermal grease layer. This results in lower junction temperatures and lower temperature swings compared to conventional liquid cold plates. The power module's lifetime with traditional and direct pin-fin baseplate cooling is evaluated under standard driving cycles. It has been shown that the lifetime of the module will be prolonged in direct cooling [8].

1.2   Thesis Objectives

This thesis's main objective is to investigate the effect of fin geometry on the thermal-hydraulic performance of a power module's integrated liquid-cooling system. The constraint of the comparative analysis is to have fins with the same length scale (hydraulic diameter) with a particular spacing in a staggered arrangement. Individual design cases with a particular fin shape can be optimized so that the optimal set of fin spacing, height, and hydraulic diameter will be obtained based on the objective functions and constraints. However, this is not the intent of the current study. The present study aims at providing power electronic thermal designers with a piece of initial information on how the choice of fin shape with different geometries and the same length scale can affect thermal performance, mass, and cost.

Additionally, it is intended to provide some insight into a comprehensive evaluation of heat sink geometry and its effect on the power module's overall performance in electrified vehicles. Performance metrics such as thermal resistance, pressure drop, pumping power, mass, and manufacturing cost are deemed necessary herein.

The thesis's secondary objective is to investigate potential fabrication methods capable of heat sink fabrication for the specific case of direct finned-type cooling. Benchmark of the fabrication methods in terms of prototyping and mass production capability is deemed important. This is important since the wide-spread adoption of complex heat sink geometries and cooling techniques in the automotive sector is highly dependent on the fabrication cost and production rate of the chosen manufacturing technique.

Furthermore, this study aims to present a comprehensive comparison framework for selecting fin geometry in finned-type liquid-cooling heatsinks. The ideal framework is the one that can take into account all performance metrics such as thermal-hydraulic performance, mass, and cost.

1.3   Thesis Outline

In this thesis, a framework for comparing various fin geometries in liquid-cooled power electronic modules is introduced. The chapters of this thesis are laid out as follows.

Chapter 2 begins with an overview of state-of-the-art power electronic cooling techniques. Cooling techniques of power electronics in electrified vehicles are classified based on the type of cooling agent and packaging/integration of the power module. The advantages and disadvantages of each cooling method are pointed out. Reasons are provided as to why finned-type liquid-cooling is chosen for the current study. The key performance metrics of liquid-cooling systems, including heat transfer rate, pressure drop, pumping power, and mass, are explained. Thermal performance criteria, which are objective functions that incorporate both thermal (heat transfer

rate) and hydraulic (pressure drop) characteristics of the heatsink, are discussed afterward. Lastly, a proper thermal performance index (TPI) is selected and modified using a special treatment that takes the heatsink area into account.

Chapter 3 presents an overview of the potential manufacturing techniques for finned-type heatsinks. First, a classification of the liquid cooling plates in terms of the fabrication and assembly considerations is presented. A brief overview of each type of cooling plate and its characteristics is provided, focusing on pocketed pin fin inset cold plate (PPFCP). Then the potential fabrication methods of the fin insert are discussed. The same fabrication methods can be practiced for finned-type power module baseplates. This is due to the similarity of the fin inserts in PPFCP with finned-type direct cooling baseplates. The fabrication methods are critically reviewed in terms of the capability of producing small feature sizes and high aspect ratios. Challenges in additive manufacturing of aluminum alloys for heatsink manufacturing are reviewed. The review pinpoints the trade-off between thermal conductivity and hardness of the 3D-printed aluminum and identifies it as a bottleneck of this method. Lastly, the fabrication methods are compared in terms of prototyping and mass production suitability.

In chapter 4, first, some assumptions regarding the operating condition of the power module are stated. The electrical model of the power module and power loss calculation are discussed afterward. An overview of the power module's packaging technologies and some assumptions about the chip layout are presented. An overview of the pin-fin geometries that are used in the literature is discussed. Then a set of pin-fin geometries are selected for the comparative analysis. The fin geometries include circular fin, drop-shaped fin, symmetric convex fin, and offset strip fin. The

methodology of the comparative analysis is discussed. Lastly, under the computational fluid dynamics (CFD) section, the CAD model of the design cases, theory, boundary conditions, and turbulent modeling technique are discussed in depth.

Chapter 5 begins with CFD settings and goes through grid topology and numerical errors. Solver settings and computation time are discussed afterward. A grid convergence study is carried out, and discretization errors are obtained using Grid Convergence Index (GCI) and Richardson's extrapolation method. The result of the CFD simulations including, temperature, thermal resistance, pressure, and heat transfer coefficient against flow rate, pressure, and temperature contours of four design cases, are presented. The pressure drop and thermal resistance of four design cases are compared and discussed in the benchmarking section. Modified TPI of different design cases is obtained and compared. Machining cost is estimated as a case study for a fabrication cost comparison. Lastly, four design candidates are compared in terms of TPI, mass, and estimated machining cost. Lastly, the baseline design result (circular pin-fins) is verified using empirical correlations from the literature.

In Chapter 6, a summary of the present work is provided. The contributions of this thesis are outlined afterward. Lastly, potential future work including, transient thermal modeling, data reduction using thermal networks, evaluation of other fin shapes, experimental validation, and advanced heatsink design approaches, are discussed.

Chapter 2

State-of-the-Art Cooling Techniques and Performance Metrics

In this chapter, an overview of the state-of-the-art cooling technologies in automotive power modules is presented. A general classification of power electronics cooling technologies is presented. Following that, a classification of the power module cooling techniques is provided based on the type of integration to the module. We will then focus on single-phase liquid-cooling techniques and further review its subcategories. Additionally, the choice of a single-phase direct liquid-cooled pin-fin baseplate is justified. Under the performance metrics sections, the performance factors of a power module's heatsinks, including heat transfer, pressure drop, thermal performance criteria, and mass, are discussed.
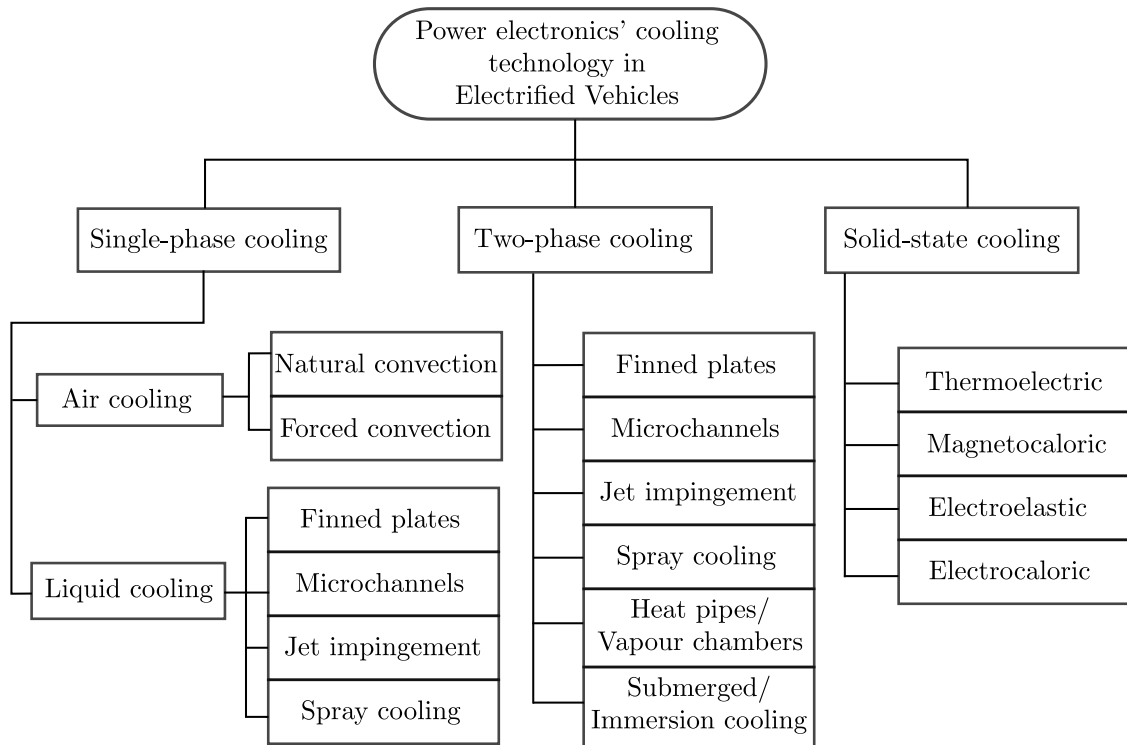
(a) Power electronics' cooling technology in electrified vehicles (adapted from [9] and modified)
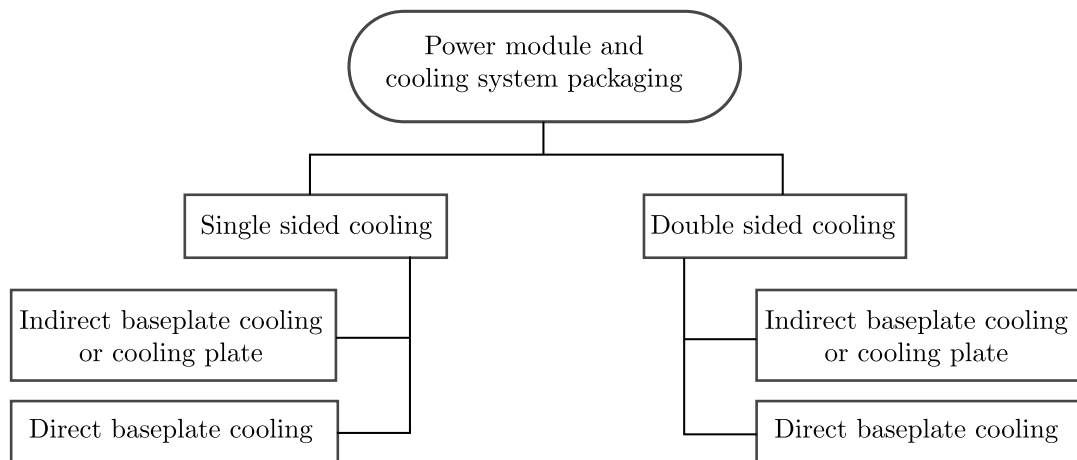
(b) Cooling techniques in terms of integration to the power electronic module

Figure 2.1: Classification of automotive power electronics cooling techniques

9

Based on the cooling agent, cooling systems of automotive power electronics can be categorized into single-phase, two-phase and, solid-state cooling. Figure 2.1ashows subcategories of each cooling method [9].

Figure 2.1b shows the cooling systems classification in terms of the type of integration to the power module. Double-sided cooling takes advantage of both the chips' top and bottom surface to increase the convective heat transfer surface area, whereas single-sided cooling is confined to one side of the chips. Both single-sided and double-sided cooling can have direct or indirect cooling on the baseplate of the module. Regardless of the type of power module mounting on the heatsink, any single-phase or two-phase cooling technology mentioned in 2.1a can be employed. Therefore it is important to distinguish the two categories since they are fundamentally different.

Figure 2.2a shows an example of indirect cooling of the power module. The main components of the power package are highlighted in the figure. The TIM's presence is crucial to the system since it fills the microscopic gaps between the module's case and heatsink's surface and reduces the contact resistance between them. Figure 2.2b shows an example of direct cooling where fins are integrated into the power module's baseplate. It should be noted that the components in the figure are representative schematics, and the size and thicknesses are exaggerated for better demonstration. The schematics shown in figure 2.2 already represent how single-sided cooling layout is as opposed to the double-sided schemes shown in 2.3. Figure 2.3 shows two common double-sided cooling packages used in 2008 Lexus LS 600 (2.3a) and 2016 Chevrolet Volt (2.3b) [6]. It is noteworthy that the coloring scheme is consistent in figures 2.2 and 2.3 so the differences between two double-sided schemes are distinguishable.

Thermal Interface Material (TIM)   Heat sink

Baseplate

Substrate (DBC)   Wire bond   Solder
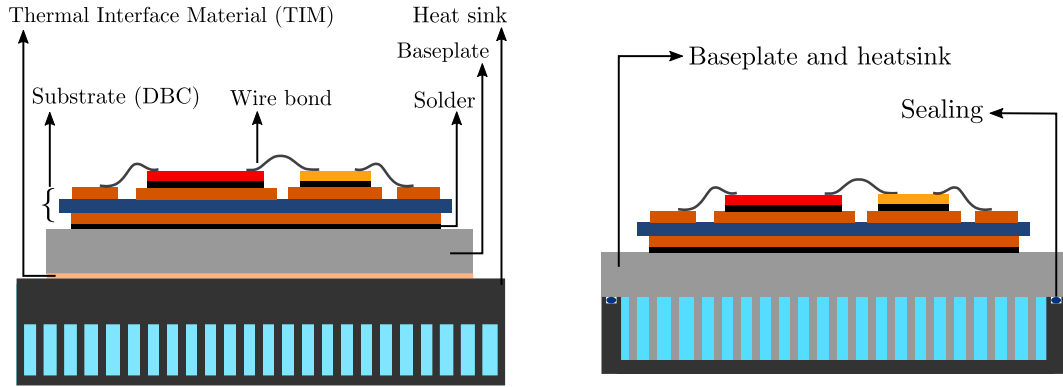
(a) Indirect cooling of the baseplate using cooling plate and TIM

Baseplate and heatsink

Sealing

(b) Direct cooling of power module's baseplate

Figure 2.2: Representative schemes of different power module and cooling system packaging

Cu Emitter
Ceramic

Cu spacer
Cu Collector
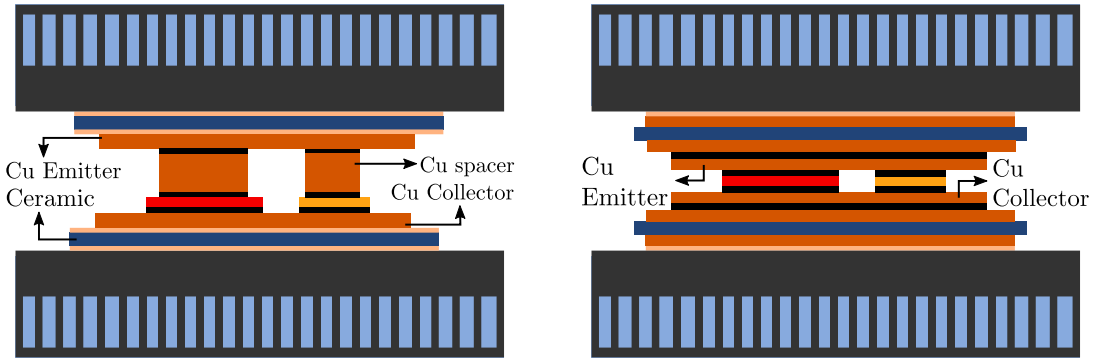
(a) Double-sided cooling (adapted from [6])

Cu
Emitter

Cu
Collector

(b) Double-sided cooling (adapted from [6])

Figure 2.3: Representative schemes of different double-sided cooling packages

The current research focuses on the liquid-cooling technique and introduces a comparison framework for some pin-fin geometries in order to facilitate the development of such heatsinks. In the following sections, an overview of liquid-cooling techniques is presented, and reasons are provided as to why pin-fin cooling technology is chosen over other techniques in this study.

11

2.1   Liquid-Cooling Techniques

Conventional air-cooling systems fall short to meet the expected cooling demands at high power dissipation, particularly when power dissipation is higher than 1500W [10]. The typical heat flux dissipation is 50 W/cm^2 and 150 W/cm^2 for air-cooling heatsinks and liquid-cooling cold plates, respectively [11]. O'Keefe et al. argue that even with a junction temperature of 200°C, natural convection does not meet the 200 W/cm^2 heat flux dissipation target. Advanced forced air cooling with significant area enhancement and cooler outside temperature (rather than underhood temperature) might meet the target [12]. This is the main reason that liquid-cooling is the focus of the current study.

It is worth noting that major high-heat-flux (HHF) cooling techniques shown in figure 2.4 can be employed in two-phase cooling as well. Two-phase cooling comes with the advantages of high heat transfer ability (up to 1000 W/cm^2) due to latent heat of vaporization and lower pumping power due to flow boiling. Despite the apparent advantages of two-phase cooling technologies, there are quite a few downsides associated with them. The condenser's extra weight and the additional modeling and design complexity increase the overall implementation cost of two-phase cooling systems. Moreover, flow instabilities due to rapid bubble growth and critical heat flux (CHF) can result in high-frequency and large-magnitude temperature swings [6], [13] All in all, flow instabilities and critical heat flux are the major barriers to the widespread implementation of two-phase cooling systems in automotive power electronics [7]. It is also worth mentioning that HHF cooling systems are the topic of the current discussion. In general, low-heat-flux (less effective) cooling systems such as macrochannel cooling plates require a large amount of heat spreading to take

place from the power device to the cooling agent. Therefore power module cooling integration (direct baseplate cooling) is not practical for them. HHF cooling systems, on the other hand, have the capability to handle high-intensity hot spots. Thus, they are able to meet cooling demands with the elimination of TIM and power module baseplate, which eventually makes the system more compact and power-dense [6]. This explains why direct cooling is being used in the representation of each cooling method in figure 2.4.
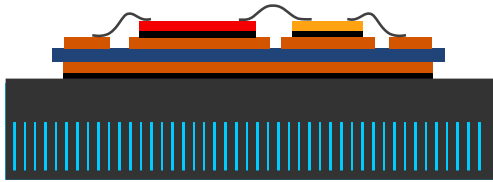
(a) Representative micro channel heat sink(MCHS)
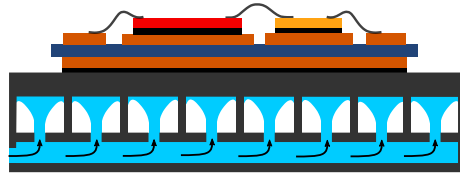
(b) Representative jet impingement heat sink
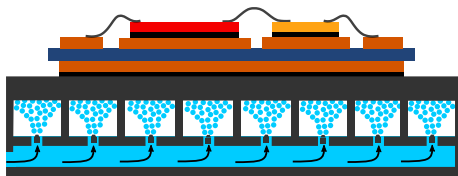
(c) Representative spray cooling heatsink
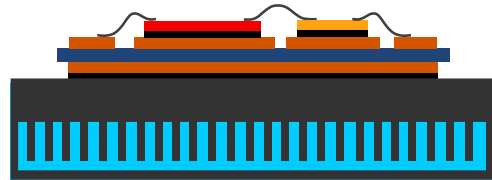
(d) Representative finned-type heat sink

Figure 2.4: Representative schemes of different liquid-cooling heatsinks

2.1.1   Mini/Micro Channels

Kandlikar has arbitrarily defined microchannels and minichannels as having a hydraulic diameter in the range of $10 – 200\mu m$ and $200\mu m – 3mm$ respectively [14]. A

representative microchannel heatsink is shown in figure 2.4a. Anything with a hydraulic diameter above 3 mm should be called macrochannel. Two different types of macrochannel cooling plates are shown in figure 2.5. Macrochannels shown in this figure have the same basic functionality, and the only difference is in their manufacturing method. This will be discussed in-depth in chapter 3.

(a) Representative macrochannel cooling plate type 1	(b) Representative macrochannel cooling plate type 2 (pressed copper tube)
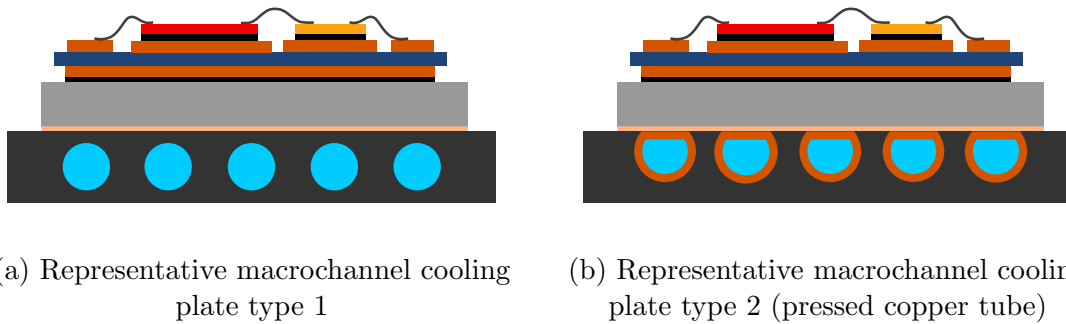
Figure 2.5: Representative schemes of macrochannel cooling plates

Microchannel heatsinks (MCHS) are simple, compact, lightweight with minimal coolant usage [11]. The convective heat transfer coefficient is inversely proportional to the channel's characteristic length. Therefore microchannels can attain extremely high heat flux removal capability [15]. Although it seems hardly practical to do a general benchmark on HHF cooling techniques' compactness, Broughton et al. have claimed that microchannel cooling is generally more compact than jet impingement or spray cooling [6]. Liu et al. have numerically and experimentally investigated the thermal performance of a 600V, 450A IGBT power module with indirect and direct DBC liquid cooling using microchannels. 25% reduction in the total thermal resistance is observed using direct cooling compared to indirect cooling. Moreover, using a microchannel cold plate has reduced thermal cycling and increased the reliability of the power module [16].

As with any other cooling technology, microchannel cooling has its own downsides. High driving pressure and the fouling build-up are two major challenges of microchannel cooling. These two factors are the primary impediments to the application of microchannel cooling in EV power electronics. Fouling would increase the thermal resistance and may eventually cause system clogging and failure [17]. The fouling problem will be lessened when using minichannels since the fouling rate is proportional to the fluid/solid interface area. This way, the reliability of the system will not be compromised. That is why minichannels can be seen more in EV power converters as opposed to microchannels.

2.1.2   Jet Impingement

Jet impingement directs fluid jets toward the target face, which need to be cooled such as the power module's baseplate. In this method, a lower working load will be imposed on the pump in comparison to MCHS. A high heat transfer rate will happen due to the formation of thin boundary layers close to the hot spot region (as high as $52000 \ W/m^2K$) [18]. The fluid jet creates a significant local heat transfer rate, which rapidly decreases when moving away from the jet center. Since the local heat transfer rate does not make an ideal temperature uniformity, an array of multiple jets are often used to enhance the temperature distribution [9], [6], [19], [20], [21], [22], [23]. A representative jet impingement heatsink is shown in figure 2.4b. Modeling the interaction of multiple jets is often an arduous task. It has been shown that when a jet interferes with a neighbouring jet, the overall heat transfer drops significantly [24], [25].

Jet impingement can be further categorized into the free jet and submerged jet

cooling. The jet is surrounded by the liquid in submerged conditions, and it is surrounded by air in free jet impingement. Surface enhancement can also be incorporated in the target face to promote turbulence and improve heat transfer. In such hybrid cooling techniques, pin-fins or mini/macrochannels can exist on the target face [26].

Bhunia et al. have investigated jet impingement cooling on the baseplate of a 450V, 400A (RMS) power module for an HEV inverter. The inlet temperature, maximum allowable junction temperature, flow rate and, pressure drop are 105°C, 125°C, 2.5 GPM and, 1.6 bar (165kPa) respectively. Although two-phase jet impingement cooling is implemented in this study, heat dissipation due to phase change only accounts for 10% of the total power dissipation (1623W). This method showed a heat transfer rate that is approximately 1.8 times improved over a state-of-the-art pin-fin liquid cooling cold plate [27]. Many conclusions could not be drawn from such a comparison since the heatsinking methods are fundamentally different. In jet impingement cooling, the baseplate is being cooled, where in a pin-fin heat sink, indirect cooling is employed along with additional layers.

There are several barriers to the application of jet impingement in cooling systems. First and foremost, jet impingement has an aggressive nature that can cause surface erosion in the long term. Uneven cooling due to locally intensive heat transfer rate is another disadvantage that should be tacked by a proper fluid distribution system and jet arrangement. Complex flow distribution system, fluid removal difficulty, cooling loop leakage, and channel blockage contribute to the overall complexity of this cooling strategy. These factors eventually make jet impingement economically costly and impede its widespread adoption in the EV industry [9], [17].

2.1.3   Spray Cooling

Spray cooing directs one or more spray of droplets towards the target hot surface. A representative spray cooling heatsink is shown in figure 2.4c. The sprayed droplets can either perturb the liquid film formed on the surface (single-phase) or evaporate on the hot surface (two-phase). Two-phase spray cooling lacks models that can widely and accurately capture the physics of the system. Often the models do not take the compound effects into consideration, such as substrate conduction, dissolved gases, and spray angles [28].

Fabbri et al. showed that single-phase spray cooling can obtain a convective heat transfer coefficient as high as 15000 W/m^2K [29]. Spray cooling can create a more uniform cooling compared to jet impingement [17]. Qian et al. has compared the effective heat transfer coefficient of some cooling techniques and have concluded that spray cooling is a potentially great choice for IGBT cooling [19]. Shaw et al. have exploited spray cooling for cooling of IGBT power modules, which drive an 18 hp AC motor. The cooling technique has shown heat flux removal capability of up to 130 W/cm^2 [30].

Like jet impingement, the downsides of spray cooling are primarily due to the system's overall complexity and cost. Difficult fluid distribution and removal, the high pressure loss in the spray and, nozzle clogging are some of the performance issues associated with spray cooling [17]. Mudawar et al. point out the spray nozzle unpredictability meaning that sprays would have dissimilar spray patterns even if they are made in the same manner [31].

2.1.4   Finned Designs

Due to the channel-wise structure of finned-type heatsinks, they are sometimes considered under the category of mini/micro-channel heatsinks [7]. This particularly occurs for cases where straight fins are used with zero clearance between the fin's tip and heatsink's enclosure. Despite the similarity, finned-type heatsinks have their own distinct characteristics and manufacturing methods and must be distinguished from channel-type heatsinks.

Pin-fin arrays (also known as a pedestal) are widely used in gas turbine cooling components as well as electronic devices. Geometrically finned-type heat sinks consist of small cylindrical-type elements that are arranged in a specific configuration. e.g., inline or staggered, with a certain spacing among neighboring fins. Forced flow passes around the fin array in a cross-flow fashion that promotes turbulence and the transport phenomena in the channel housing the arrays. Pin-fins promote heat transfer by adding extra effective surface area and turbulence. Additionally, the pin-fin array promotes flow acceleration when passing through the reduced distance between the fins. This will enhance the local convective transport. Moreover, the accelerated flow from the preceding row of fins directly impinges onto the front side of pin-fins in a staggered fin array, significantly augmenting the heat transfer rate [32]. This is the main reason that the staggered pin-fin array is the focus of the current study.

A representative finned-type heatsink is shown in figure 2.4d. The key element of finned-type heatsinking is the surface enhancement using extended surfaces or fins. There are quite a few characteristics that finned-type heatsinks share with microchannel heatsinks. First and foremost, depending on the cooling demand, the flow rate available to the system, and the inlet/outlet locations, there might be series or parallel

channels to either distribute the flow or increase the flow velocity. The next similarity is the length scale of the channels or extended surfaces. Two characteristic lengths can be defined either based on the fin's hydraulic diameter or based on the hydraulic diameter of the channel created between the fins. Either way, in high-efficiency cooling surfaces, these two characteristic lengths are in the same range. That being said, if we accept the arbitrarily defined range of macro, mini and, microchannels for the fin hydraulic diameter, the channel characteristic length will most likely be in the same range.Therefore, an extended surface with pin-fins with a hydraulic diameter of $3mm$ or above is considered macro pin-fin. Anything with a pin-fin hydraulic diameter in the range of $10 - 200\mu m$ and $200\mu m - 3mm$ will be referred to as "micro pin-fin" and "mini pin fin," respectively.

2.1.5   Discussions

Although it seems practically impossible to present a comprehensive comparative picture of all the available cooling technologies, researchers have made some efforts to provide insight into the overall benchmarking of the methods. Fabbri et al. have experimentally compared spray cooling to microjet cooling. They proved that microjets have superior performance than spray cooling due to lower pumping power [29]. Lee et al. argue that it is unreasonable to compare microchannel cooling to jet impingement because of fundamentally different operating conditions. Microchannel cooling requires a relatively small flow rate while producing a large pressure drop. Jet impingement requires a very large flow rate with a relatively small pressure drop. They argue that a fair comparison should be made so that the optimal design of each cooling method (in its own operating condition) is compared to one another. Based

on their analysis, it turned out that jet impingement's thermal performance without spent flow treatment is significantly lower than microchannel cooling. With proper treatment of spent flow, jet-impingement becomes quite comparable to microchannel cooling. Furthermore, it has been proved that microchannel cooling is better for smaller target plate dimensions while jet impingement is comparable or better for larger target plates [25]. Kandlikar et al. have assessed the thermohydraulic performance of jet impingement, spray cooling, and microchannel heatsinking for high heat flux removal. They have highlighted that single-phase microchannel cooling such as offset strip fin shows superior performance relative to other methods and is the most viable option for electronics cooling due to structural and leakage consideration [26]. It is noteworthy that, as mentioned earlier, in all of the mentioned studies, surface enhancement using pin-fins is considered under the category of microchannel cooling due to the channel-wise structure.

It is of utmost importance to note that the power electronic industry is technology-driven in cooling system integration. In a given application, e.g., automotive power electronics, the technology-driven trend does not necessarily achieve gain in terms of cost, reliability, or manufacturability [25], [33]. This is particularly true in the automotive sector, where cost-oriented product development strategies exist. That is why despite the proven capability, we have not seen cutting-edge cooling technologies, e.g., two-phase, jet-impingement, and spray cooling, being employed in vehicles in production so far. More than a decade ago, one could argue that this is because of the lag between R&D and production, whereas now these technologies have become mature enough.

2.2   Performance Metrics

2.2.1   Heat Transfer

The most important characteristic of a power module cooling system is to conduct away the power loss dissipated by the power module with the minimum temperature difference between the junction and the fluid. It is of utmost importance to distinguish the heat removal capacity from a cooling system's heat transfer capability. Heat removal capacity is sometimes reported in the datasheet of cooling plates and does not convey any important information about a cooling system's effectiveness. Briefly speaking, heat removal capacity is related to the specific heat and flow rate of the cooling fluid flowing through the heatsink. The fluids with a higher heat capacity (higher flow rate or higher specific heat) will be able to carry away a certain amount of heat with less coolant temperature rise from inlet to outlet. This is discussed more in section 4.5.3. On the other hand, heat transfer capability is a measure of how effectively the heat is being conducted away from the heat generation area so that junction temperatures lower than a certain threshold can be achieved. This can either be described in terms of the convective heat transfer coefficient on the fluid/solid interface wall, heat flux removal, or the cooling system's thermal resistance.

Heat Transfer Coefficient

Heat transfer coefficient on the fluid/solid interface can be defined as:

$$h_{avg} = \frac{\overline{q''}}{T_{i,avg} - T_{f,avg}} \tag{2.2.1}$$

Where $\overline{q''}$ is the dissipated heat flux on the interface wall, $T_{i,avg}$ is the average temperature of the interface wall and $T_{f,avg}$ is the average fluid temperature. $T_{f,avg}$ is often defined by:

$$T_{f,avg} = \frac{T_{f,in} + T_{f,out}}{2} \tag{2.2.2}$$

Where $T_{f,in}$ and $T_{f,out}$ are fluid inlet and outlet temperatures respectively. Other averaging methods, such as volume-average fluid temperature, are also acceptable.

Heat Flux Removal

Another useful measure of a power electronic cooling system is the heat flux removal capability. This term refers to the highest heat flux (W/m^2) that a cooling system can handle while maintaining the junction temperature below the required level. Some researchers refer to this as power density [19]. Heat flux in automotive power devices are as high as 200 W/cm^2 and will continue to grow as power module's technology advances. Heat flux removal requirement will become higher as the power device manufacturing technology reaches higher power density targets. Over the past decade, heat flux in power electronics has reached and surpassed the 500 W/cm^2 target, which was projected in the late 2000s [11], [34], [35], [36]. Air cooling techniques have reached their limit as the power packages became smaller in size and higher heat fluxes became present. O'Keefe et al. present an overview of the heat flux removal capability versus effective convective heat transfer coefficient for different power module packages such as integrated heatsink (IHS), single-sided and double-sided cooling [12].

Ebadian et al. have reviewed the High Heat Flux (HHF) heat removal technologies in power electronics cooling. Based on their work, jet impingement, microchannel, and spray cooling have been proved to have better heat flux removal, respectively

[7], [37], [38], [39]. Figure 2.6 shows the comparison. However, such a comparison is not comprehensive since it does not include any information regarding the pumping power/pressure drop of the cooling technique.
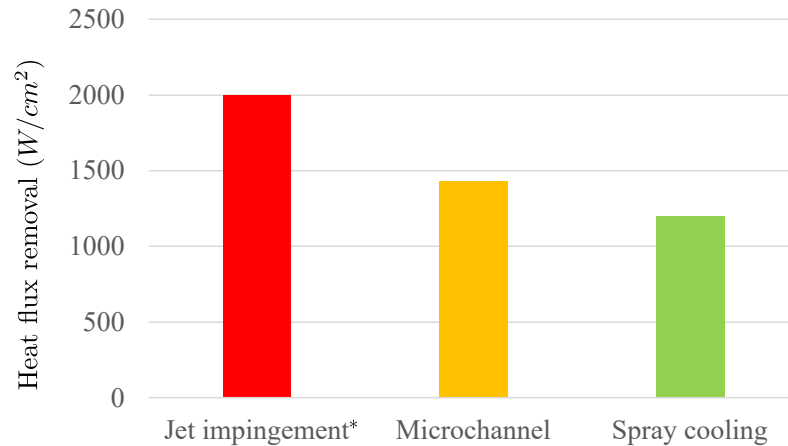
*This heat flux is achieved in combination with liquid metal.

Figure 2.6: Maximum heat flux removal capability of different cooling options (adapted from [7])

Thermal Resistance

Figure 2.7 demonstrates the idea of the thermal resistance based on the temperature of various components of a power module package. The equivalent 1D thermal network is shown on the left side of the figure along with the common nomenclature. Assuming that there is no contact resistance between different components, each of the thermal

resistance in the figure will be obtained as follows:

$$R_{th,j-c} = \frac{T_j - T_{module\ case}}{P} \tag{2.2.3a}$$

$$R_{th,TIM} = \frac{T_{module\ case} - T_{case\ heatsink}}{P} \tag{2.2.3b}$$

$$R_{th,c-f} = \frac{T_{case\ heatsink} - T_{fluid}}{P} \tag{2.2.3c}$$

The total thermal resistance from junction to the fluid can be defined similarly and will be the summation of all of the thermal resistances in series:

$$R_{th,j-f} = \frac{T_j - T_f}{P} = R_{th,j-c} + R_{th,TIM} + R_{th,c-f} \tag{2.2.4}$$

Generally, heatsink design and optimization problem target lower case to fluid thermal resistance ($R_{th,c-f}$) as other parts of the thermal resistance depend on the power module's manufacturing technology and the TIM used. In liquid-cooling techniques with high heat flux removal capability, the TIM's thermal resistance becomes the bottleneck [6], [40]. That is why direct cooling is the preferred option in comparison to indirect cooling in most cases. A higher chance of leakage is the only downside of the direct cooling method that can be properly tackled. Broughton et al. has observed a trend towards the elimination of various layers, including TIMs. However, the penalty of using TIMs in double-sided cooling configuration seems to be lessened because these systems are much more efficient in heat removal than single-sided systems. This explains why thermal grease is being used frequently in double-sided systems. A migration to double-sided cooling has been seen in the fourth generation of Toyota power converters [6]. Qian et al. has claimed that direct cooling can introduce up to a 30% reduction in thermal resistance instead of conventional indirect

cooling [19]. For the case study of the current work, a representative power module with direct cooling is selected. Even though the case study is carried out for direct cooling, the methodology and results maintain generality and can be very simply applicable to indirect cooling cases with minimal modification.

It is worth mentioning that diode, and semiconductor switches operate with different power dissipation rates. Since the dissipated power and temperature of these two chips are different, different thermal resistance values should be used. If we consider the diode temperature and diode power dissipation in equation 2.2.4, the diode thermal resistance will be obtained. Semiconductor's thermal resistance can be obtained similarly.
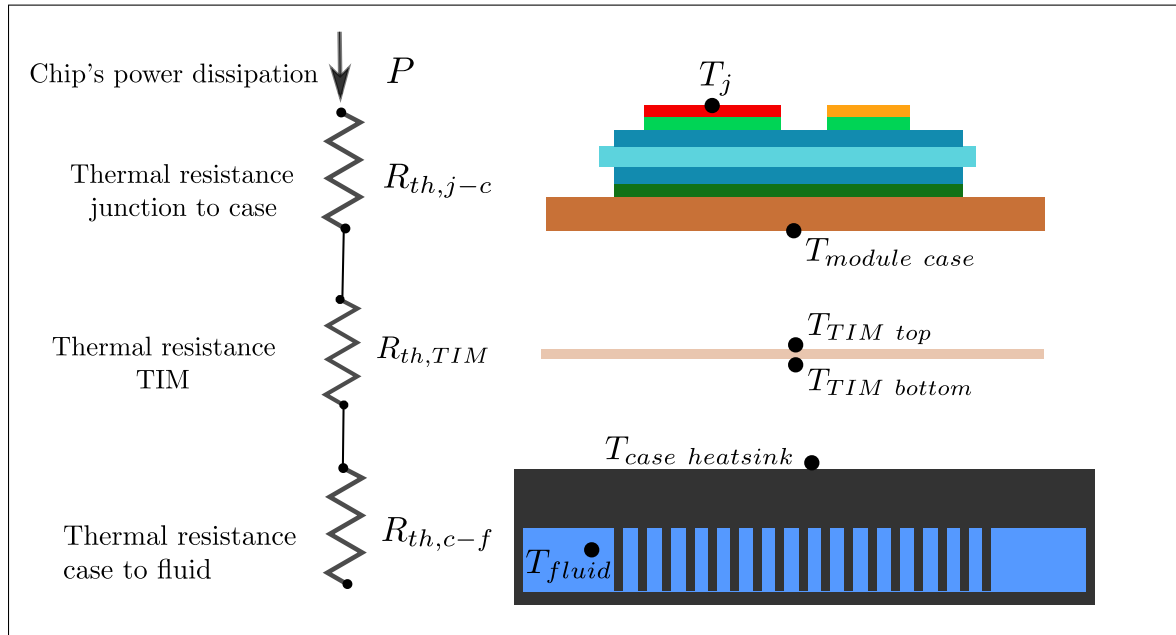
Figure 2.7: 1D thermal resistance definition for a typical power electronic module and cooling system

As informative as thermal resistance values are, they do not reflect the actual complexity of the system. First of all, they are based on the components' average

temperature and neglect the temperature distribution. Additionally, they do not capture the heat spreading effect on the module's substrate since the thermal network is one dimensional. Even though thermal resistance values are widely used in power module and cold plate datasheets to obtain an initial guess of the devices' junction temperature, high fidelity models such as CFD should be used to further characterize thermal design concepts and operating temperatures.

Another downside of thermal resistance definition is that it cannot capture transient effects of the system. In reality, a thermal capacitance should be considered in parallel with each component's thermal resistance to be able to model transient conditions. In such conditions, each component's transient behaviour and time constant are extremely important to predict each component's temperature cycle and see how fast each component can conduct the heat away . The combination of thermal resistance and capacitance is called thermal impedance. More complex RC thermal networks such as *Foster* and *Cauer* networks are developed to address this issue [41], [42]. Even though these thermal networks do not have the accuracy of CFD, they are very cheap for real-time implementation due to lower computational time compared to CFD. CFD is very time consuming and remains practically impossible in real-time application. There is no need to mention that the fast nature of these thermal networks enables coupling to the system's electrical model. This has resulted in more accurate consideration of thermal effects in the control of the power module [43]. Significant gains can be obtained in the power converter's overall lifetime by incorporating the thermal network into the power converter's control to reduce the junction temperature variation [44].

A significant trend towards using high heat transfer capable designs using micro-channels and nano-channels is visible in the literature. This trend is quite under-standable because as we move towards small-scale pin-fins or channels, the ratio of surface area to volume of the conductive solid domain grows. Growth of such ratio means that the surface area of the convective heat transfer increases, which results in higher heat transfer with less conductive material (less mass). However, as mentioned earlier, cooling techniques with higher heat transfer rates definitely come with higher pressure drop and higher design complexity and higher manufacturing and in-service costs.

2.2.2   Pressure Drop

Pressure drop is the amount of pressure loss from the inlet to the outlet of a cooling system. Generally, pressure drop increases as the flow rate increases (or equivalently, inlet velocity increases). The pressure drop is a measure of the system's thermal performance as it dictates how much pumping power is required to circulate the flow into the cooling system at a certain flow rate.

$$P_p = Q\Delta p \qquad (2.2.5)$$

Where Δp is the pressure drop, and Q is the volumetric flow rate. Pressure drop can be obtained as follows:

$$\Delta p = (\frac{1}{Q} \int_{inlet} p \ dQ) - (\frac{1}{Q} \int_{outlet} p \ dQ) \qquad (2.2.6)$$

Since the mass flow rate is proportional to the volumetric flow rate ($\dot{m} = \rho\, Q$) for constant density cases, each term of the right-hand side of the equation 2.2.6 will be equal to the mass average pressure. Therefore, the pressure drop will be the difference of mass-weighted average pressure in the system's inlet and outlet sections.

Ideally, we want to have the least possible pressure drop in a cooling system to pump the flow into the system with minimum pumping power. However, this is limited because a minimum amount of flow rate is required to achieve the thermal targets in a certain cooling system. Therefore there is always a trade-off between the heat transfer enhancement in a cooling system and the pumping power. The more we enhance the heat transfer coefficient, the higher the system's pressure drop will be. A higher pressure drop (or pumping power at a certain flow rate) means that a larger pump is required to circulate the flow into the system.

Friction Factor

Another way of describing a heatsink's pressure drop is through friction factor. The friction factor (also known as Darcy's friction factor) was originally defined for pressure loss in pipes. Such friction factor was then used along with extensive experimental data to develop moody's chart, which is the friction factor as a function of pipe surface roughness and Reynolds number. Another coefficient is also defined for cases where more complex geometries such as valves or fittings are involved. This coefficient is called the loss coefficient and is defined by [45]:

$$f = \frac{2\Delta p}{\rho V^2} \tag{2.2.7}$$

Where V is the inlet velocity, and Δp is the pressure drop between inlet and outlet sections. Generally, friction factor in high height-to-diameter ratio pin-fins ($H/D > 8$) referred to as tube boundles or fin boundles seems to be insensetive to H/D ratio. The end-wall effects become more significant as we move down to low aspect ratio pin fins ($H/D < 1/2$). Intermediate aspect ratio fin banks ($1/2 < H/D < 8$) are proved to show the same insensitivity to H/D ratio in friction factor in transitional and turbulent flows. It is also worth mentioning that it has been shown that the end-wall effects also become insignificant in high Re number flows. This is because fin-wall interaction height becomes lower at higher Reynolds numbers [46], [47], [48].

Cylindrical pin fins with intermediate height-to-diameter ratio (typically $1/2 < H/D < 4$) are significantly useful in turbine cooling systems and has been in use for decades [49]. There are many studies on the effect of fin spacing and H/D ratio on friction factor for intermediate H/D ratio pin fin banks in macro or mini length scales [50], [51]. These studies show similar trends regarding insensitivity to H/D ratio for intermediate ratios which is also in agreement with the findings of Jakob [52] for long tubes [53]. Armstrong et al. compared the experimental data from [50], [51], [52] and, [54] and concluded that the correlation developed by Metzger et al. has the best agreement with the experimental data [55].

Besides the general friction factor of equation 2.2.7 another definition of friction factor has been used, which is specific to pin-fin heatsinks. Such friction factor is

defined by [56], [57]:

$$f = \frac{2\rho \, \Delta p_{fin}}{N_L \, G^2} \tag{2.2.8a}$$

$$G = \frac{\rho \, Q}{A_{min}} \tag{2.2.8b}$$

Where Q is the volumetric flow rate and Δp_{fin} is the pressure drop of the pin-fin section. A_{min} is the minimum cross-section of the fluid within the pin-fin section, which is dependent on the fin arrangement and spacing. This will be discussed more in the result section. Equation 2.2.8 is basically the same equation as 2.2.7 except that the maximum flow velocity within the pin-fin section is used in the denominator instead of the inlet velocity.

Pressure Drop in a Cooling Circuit

It is noteworthy that the cooling circuit's overall pressure loss is what dictates the size of the pump, whereas the heatsink is only one of the components of the cooling circuit. Other components such as the radiator and potentially other powertrain components of the vehicle (electric machines for instance) also exist in the cooling circuit (e.g. Toyota Prius MY 2004 cooling circuit is shown in figure 2.8). It should be noted that factors such as head loss due to the friction in the piping and fittings also contribute to the total pressure drop. It is worth mentioning that the other components of the cooling loop specify how critical the heatsink's pressure drop is to the overall system's performance and mass. For simplicity, let us assume that the radiator's pressure loss is the dominant loss of a cooling loop. We assume 70% of the

overall pressure drop is caused by the radiator, and only 20% is due to the heatsink. Additionally, other factors account for 10% of the losses. In this case, assume that we pushed the limits of the heatsink's thermal design and introduced a 50% less pressure drop with a new heatsink. The heatsink's pressure drop enhancement effort will only introduce a 10% reduction in the cooling system's overall pressure loss. Even though the pumping power will reduce 10%, the pump's size is less likely to change. All in all, it is of paramount importance to precisely consider all of the trade-offs, including mass and power consumption of the cooling circuit in a real-world heatsink design for automotive application.
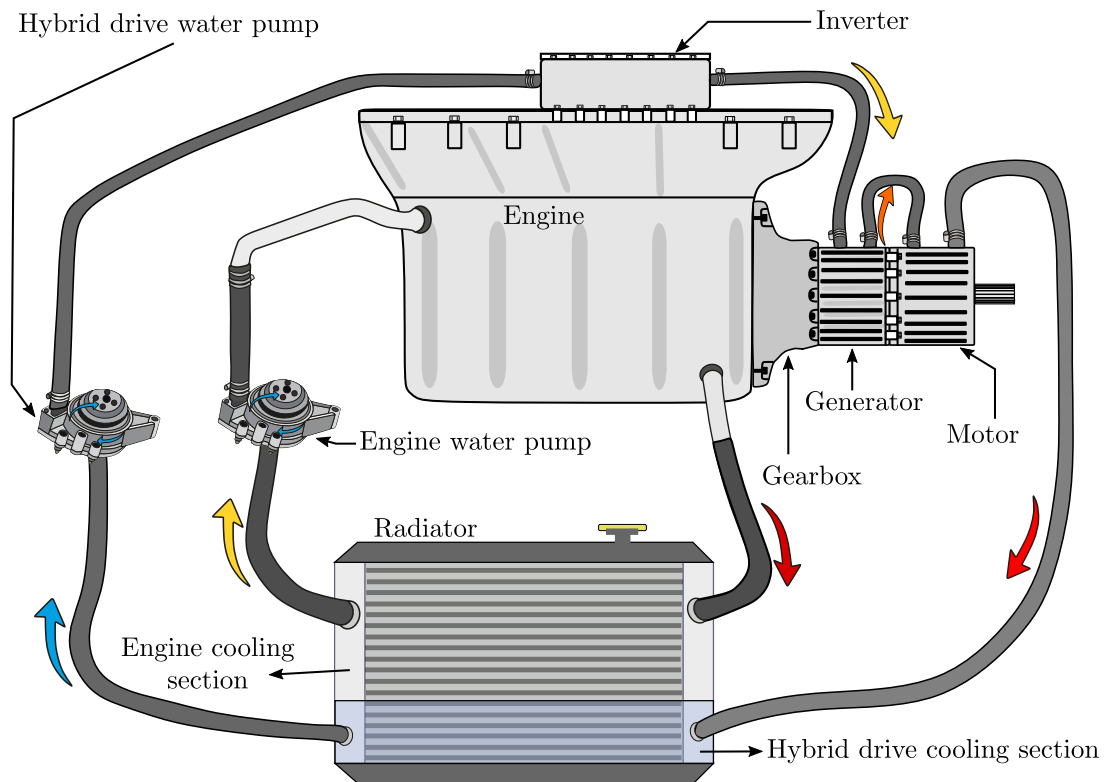
Figure 2.8: Schematic of cooling loops of Toyota Prius (adapted from [58])

In the current study's scope, the cooling system of a traction inverter is viewed as a standalone component, and pump sizing trade-off is not investigated. Different pin-fin designs will be compared in terms of heat transfer efficiency, pressure drop, and mass. Mass and thermal performance trade-off is left to the thermal designer's decision. This decision includes trading off a little of the pumping power (and/or pump mass) to achieve a lighter or more efficient cooling system, which in turn increases the life-time of the power electronics.

2.2.3   Thermal Performance criterion

It is imperative to consider a thermal performance criterion when performing a comparative analysis or heatsink optimization. Otherwise, the effect of pressure drop/thermal resistance trade-off would not be considered. This could potentially make the design improvement end up in the wrong direction. Kosar et al. have compared different micro pin-fin shapes using performance criteria such as thermal resistance at constant pressure drop and constant pumping power. The performance evaluation result shows that different designs were concluded as superior design using various performance evaluation criteria [59].

Although using different thermal performance criteria results in different conclusions in comparative analysis, the criterion seems to be rather incoherent and disperse in the literature. Duangthongsuk et al. have used the following definition as the thermal performance criterion [60]:

$$\eta = \frac{h/h_0}{\Delta P/\Delta P_0} \tag{2.2.9}$$

Where h_0 and ΔP_0 are the heat transfer coefficient and pressure drop of the baseline

case, respectively.

Another definition that other researchers have used more widely is the Thermal Performance Index (TPI) defined as follows [56], [57], [61], [62].

$$\eta = \frac{Nu/Nu_0}{(f/f_0)^{1/3}} \tag{2.2.10}$$

Where Nu_0 and f_0 are the Nusselt number and friction factor of the baseline case, respectively. The characteristic length used in the Nusselt number definition ($Nu = hD_h/k$) is simply the fin's hydraulic diameter.

There is an important factor of thermal performance that both thermal criteria are not able to capture. When considering the nusselt number and the average heat transfer coefficient, the effect of the area enhancement is being neglected. The penalty of heat transfer coefficient reduction by area enhancement will often get compensated by the increase in surface area. Equation 2.2.9 and 2.2.10 are incapable of capturing the area enhancement effect. We believe that such thermal performance criteria need to be revised to give a clearer picture of the thermal design improvement. That is why a modification to equation 2.2.10 is suggested herein. There is a way out of this dilemma by incorporating an effective heat transfer coefficient in equation 2.2.10. It is worth mentioning that this criterion is selected since the research community in the field has more widely adopted it. Area enhancement as defined by [12] is:

$$EA = \frac{A_{b,0}}{A_b} \tag{2.2.11}$$

Where $A_{b,0}$ is the surface area of the plain baseplate with no fins and, A_b is the baseplate total surface area with pin-fins. The total average heat heat flux dissipation

$(\overline{q''})$ rate can be obtained from the following equations:

$$\overline{q''} = \overline{h_{eff}}\Delta T \tag{2.2.12a}$$

$$\Delta T = \overline{T_{b,0}} - \overline{T_f} \tag{2.2.12b}$$

$$\overline{h_{eff}} = \eta(\overline{h}.EA) \tag{2.2.12c}$$

Where $\overline{h_{eff}}$, $\overline{T_{b,0}}$, $\overline{T_f}$, and η are average effective heat transfer coefficient on the baseplate surface (without fins), average temperature of the baseplate (without fins), average fluid temperature, and efficiency of the pin-fin respectively. If we substitute $\overline{T_{b,0}}$ with $\overline{T_b}$ (avergae baseplate temperature with pin-fins), we can remove the pin-fin efficiency from equation 2.2.12c. Thus we can rewrite 2.2.12 equations in the form of below:

$$\overline{q''} = \overline{h_{eff}}\Delta T \tag{2.2.13a}$$

$$\Delta T = \overline{T_b} - \overline{T_f} \tag{2.2.13b}$$

$$\overline{h_{eff}} = EA. \overline{h} \tag{2.2.13c}$$

Where $\overline{h}$ is the average heat transfer coefficient on the interface wall with fins. If we use equation 2.2.13c when computing Nusselt number for equation 2.2.10, the resultant TPI can capture the area enhancement effect.

2.2.4   Mass

Power density (both volumetric and gravitational) is an important factor in power module packaging technology. As mentioned earlier, a few trade-offs must be looked into when considering the power density of the power module. The first component-level trade-off is the thermal resistance and thermal capacitance trade-off. In general thermal designers are looking at increasing the thermal performance by reducing the case to fluid thermal resistance. In cases where thermal resistance reduction is achieved by reducing the channel length scale (such as microchannels), the improved design almost exclusively comes with a lower mass. The mass reduction associated with the thermal resistance enhancement comes with the cost of thermal capacitance reduction. Thermal capacitance acts as a thermal inertia that damps the power device's temperature fluctuations due to power dissipation cycling. Power cycling is dependent on the load profile of the inverter and is caused by both the switching losses and conduction losses. Power modules and cooling systems with higher mass are capable of handling higher transient loads. Thermal resistance reduction will lead to lower average junction temperature, whereas thermal capacitance reduction will result in more junction temperature swings due to power cycling. Zhou et al. pointed out that in cases where the average junction temperature is below the required level, the power device's lifetime is more dependent on the junction temperature variation than average junction temperature [44]. Therefore mass reduction below a certain threshold jeopardizes the reliability.

Maysenc et al. have presented a very insightful analysis of the power electronics cooling effectiveness versus thermal inertia. It Initially highlights the relationship

between cooling system effectiveness and thermal inertia and states that augmentation of cooling effectiveness reduces the thermal inertia. Then it is discussed how low thermal inertia causes high temperature variation around the average junction temperature under load cycling conditions. Such temperature fluctuation considerably increases the stress in the device packaging (wire-bond lift-off, solder fatigue, substrate delamination) and accelerates device aging, eventually causing failure. Furthermore, a technique is introduced to consider the loss variation in the selection of the cooling technique at the initial design stage. The technique is based on the thermal impedance of the cooling system and frequency of the loss variation. It can determine whether a certain cooling system can damp the fundamental harmonics of temperature variation under a certain load cycling condition. The technique can quantify whether the extra cost of increasing cooling effectiveness is worth the price or not introducing much gain due to compromising reliability. [33]

Another trade-off in the system-level thermal management is the power module and cooling system's mass versus the overall mass of cooling circuit components. When the power module and its corresponding cooling system are optimized for better thermal performance and lower mass, the resultant power converter may need a larger pump or higher power consumption. In reality, it is challenging to look into both of these trade-offs with little to no information about the cooling circuit and its requirements. Therefore the mass and thermal performance trade-off analysis herein is confined to the component-level instead of the system-level.

Chapter 3

Manufacturing Considerations of Finned-Type Heat Sinks

In this chapter, an overview, as well as a classification of liquid-cooled heatsink manufacturing techniques, are presented. Then the study focuses on direct liquid-cooled heatsinks and their manufacturing techniques. The critical review does not aim to compare the techniques but rather highlight each technique's strengths and shortcomings for the particular case of pin-fin geometries. Conventional manufacturing techniques such as machining, casting, and powder injection molding are reviewed. Then we will go through advanced manufacturing techniques such as Electric Discharge Machining (EDM), etching, and 3D-printing and discuss their potentials and challenges.

3.1 Classification of Liquid-cooled Heatsinks

As mentioned earlier, depending on the type of heatsink integration to the power module, the liquid-cooled heatsink can be divided into indirect cooling heatsinks (cold plate) or direct cooling heatsinks. Figure 3.1 shows a general overview of different types of cold plates in terms of the manufacturing method.
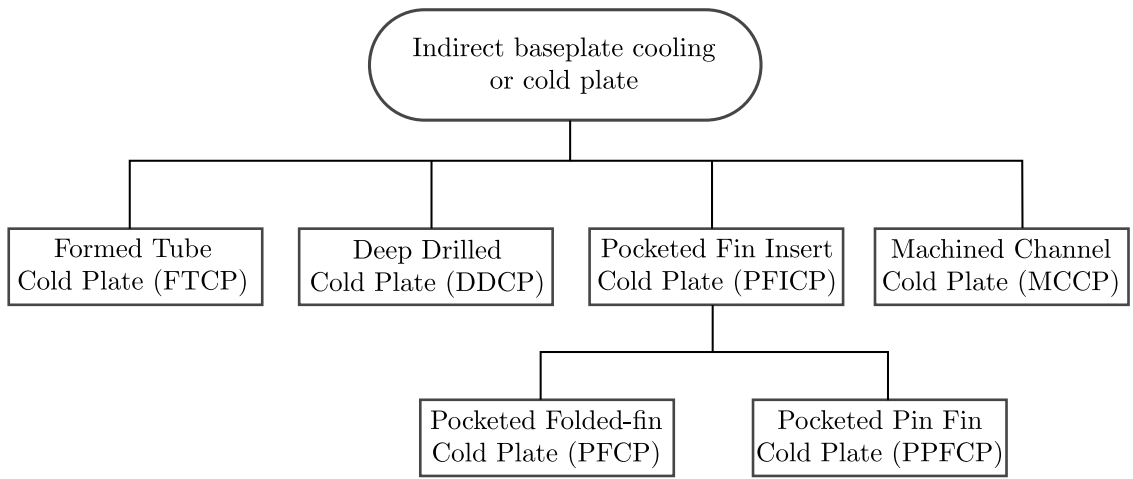
(a) Classification of cold plates (adapted from [10] and modified)
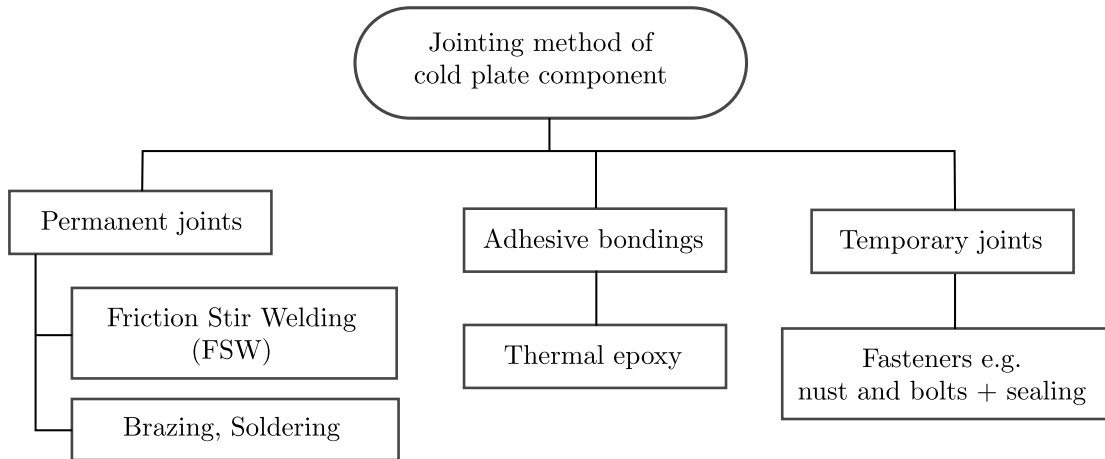
(b) Jointing method of multi-component cold plates

Figure 3.1: Overview of different types of liquid cooling plates in terms of manufacturing and assembly consideration

An example of formed tube cold plates is shown in figures 3.2a , and 2.5a. In this method, tubes, usually made of copper, are attached to the cold plate's machined surface by soldering or thermal epoxy. This type of cold plates are not very effective and are mainly used for low power application.

An instance of deep drilled cold plates (DDCP) is shown in figure 2.5b. The cold plate is usually made of copper or aluminum, depending on the mass and thermal capacitance requirement. This type of cooling can be more effective than FTCP. The unwanted hole ends are capped using end caps or plugs. The channel/hole can be designed in parallel or series. Series configuration usually has a better heat transfer rate than parallel configuration at a certain flow rate. However, higher pressure drops are encountered in series cooling. One of the challenges of parallel flow arrangement is flow maldistribution, which leads to non-uniform thermal cycling of the power devices [10]. An optimized flow distribution passage should properly tackle flow maldistribution [63].

Pocketed Fin Insert Cold Plates (PFICP) are made of an enclosure with some pockets where the finned inserts will be placed. The enclosure contains the coolant liquid and provides passages for fluid distribution and removal. Finned inserts promote turbulence and provide surface enhancements beneath the power module's mounting place where it is needed the most. An efficient surface enhancement should be centered around the heat dissipation area. Thus, these types of cold plates are normally made of two or more pieces. Additionally, single-piece heatsinks with cavities are costly to manufacture. Each piece may be manufactured with a variety of manufacturing techniques, and the pieces should be jointed together. The common jointing

methods are summarized in figure 3.1b. It is worth mentioning that solid-state welding techniques such as FSW have been significantly utilized in off-the-shelf cold plates as a primary means of permanent jointing due to superior mechanical and thermal performance over fusion welding techniques. Examples of different types of PFICP such as PFCP and PPFCP are shown in figure 3.2b and 3.2c, respectively. Folded-fins are primarily manufactured through sheet-metal working. Examples of folded-fin geometries include honeycomb, herringbone, ruffled and lazy ruffled, offset, lanced, lanced and offset, perforated, and triangular [10].
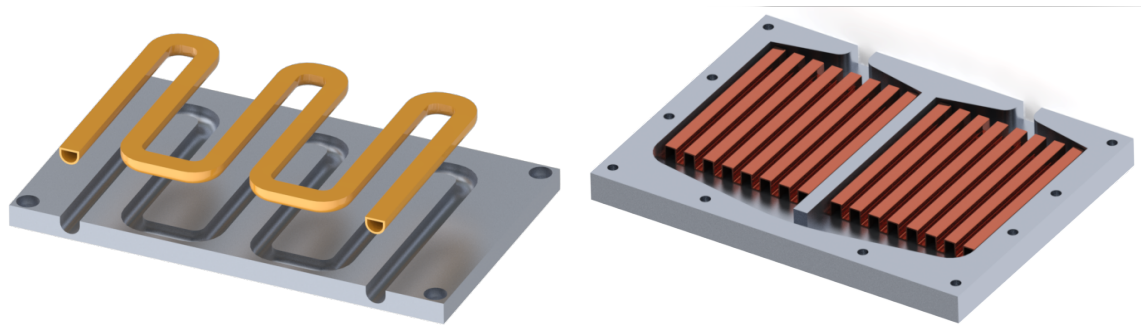
(a) Representative Formed Tube Cold Plate (FTCP)

(b) Representative Pocketed Folded-fin Cold Plate (PFCP)
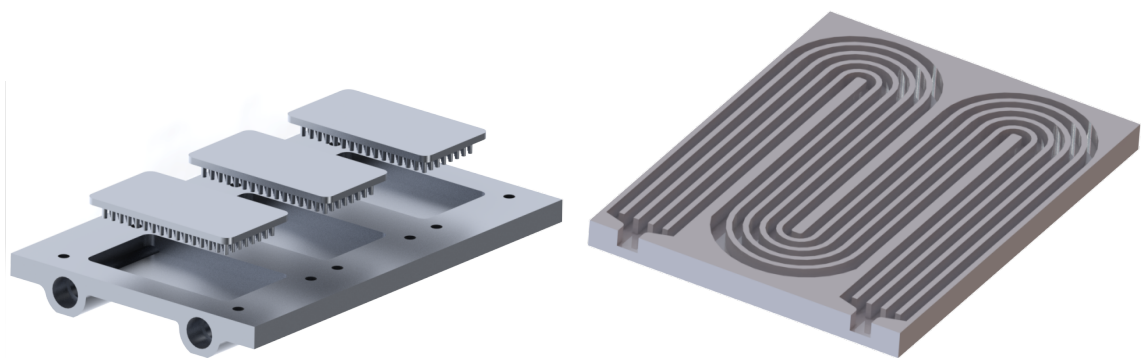
(c) Representative Pocketed Pin Fin Cold Plate (PPFCP)

(d) Representative Machined Channel Cold Plate (MCCP)

Figure 3.2: Various types of cold plates

40

Machined Channel Cold Plates (MCCP) are similar to PFICP in many ways. The only difference is that the finned section is a single machined piece instead of folded-fins or multiple fin inserts. Should the length scale of the channels used in this type of cooling be in the micro range, it can be referred to as micro-channel heatsinks as discussed in chapter2. An example of representative MCCP is illustrated in figure 3.2d. Well-known serpentine style channels are used in this particular MCCP. PFICP, together with MCCP, can be defined as finned-type cold plates.

Direct baseplate cooling of the power module share many characteristics with finned-type cooling plates. The only difference is that the area enhancement (fins) is integrated into the power module's baseplate. Numerous advantages such as simplicity (less number of components), elimination of TIM, and etc., have been introduced by such integration. When it comes to direct baseplate cooling, only temporary jointing methods such as fasteners are feasible since the cooling enclosure/jacket design is left to the user's decision and application-specific requirements. Therefore, reliable sealing becomes important. Since this thesis's focus is on power module heatsinks, the heatsink integrated into the baseplate is the focus of the discussion. The fabrication methods are similar to that of fin insert cold plates. Thus, from now on, whenever we are referring to heatsink fabrication, fabrication of the finned base plate is intended. Conventional manufacturing methods such as machining, casting, injection molding, electric discharge machining (EDM) are first discussed. Then advanced manufacturing processes such as etching and metal 3D-printing are investigated. It is noteworthy that extrusion is excluded from the current discussion because this method can only produce heatsinks with a constant cross-section such as straight finned heatsinks.

3.2   Conventional Manufacturing Methods

3.2.1   Machining

Machining techniques for heatsink manufacturing can be categorized into two primary techniques: 1-slot/form milling 2-end-milling/micro end-milling

Slot/Form Milling

In form milling or slot milling, a cutting saw with some flutes on the outer edge will be moved against the workpiece to form straight channels/fins. Despite the effectiveness of this method for manufacturing straight channels, it is incapable of pin-fin fabrication. Thus, it is not a potential manufacturing technique for the heatsink design candidates available in this thesis.

End-milling/Micro End-milling

End-milling is one of the most suitable ways to heatsink prototyping for low-volume production. It is the process of removing material by end-mills as the cutting tool. Depending on the small feature sizes available in the heatsink, the end-milling process can be considered macro-machining, mini-machining, or micro-machining. The machining process will be called micro-end-milling if the end-mill diameter is in the range of 5-1000 μm.

The cutting speed in the end-milling process is dependent on the workpiece material and tool material. The cutting speed is defined as the linear velocity of the

cutting tool edge with respect to the workpiece. In order to keep a certain cutting speed as we decrease the tool diameter, the spindle speed (RPM) must be increased. Therefore, the spindle speed in micro-end-milling is generally much higher than macro-end-milling. Machining is not entirely economical for mass production of heatsink due to high machining time in micro-machining. Interested readers are referred to the work of Jasperson et al. for more information on the process parameters of micro-machining [64].

3.2.2   Casting

Casting in its basic form includes pouring molten metal into a mold where solidification takes place and then removing the part from the mold. Since heatsinks are almost exclusively made of thermally conductive materials such as copper or aluminum, the discussion focuses on metal casting processes. A general classification of metal casting techniques categorizes the casting methods into two types: (1) expandable molds and (2) non-expandable or permanent molds. Expandable molds are often made of one piece that is not reusable and will be destructed after solidification to remove the part. Permanent molds are usually made of two sections (halves) that are precisely designed for opening and closing. Common mold materials include but are not limited to steel and cast iron. Sufficient allowance must be considered for shrinkage and machining. Amongst numerous casting methods, die casting (permanent mold) and investment casting (expandable mold) have shown the highest levels of quality and are able to create the finest feature sizes [64]. In macro-scale casting, die casting and investment casting are able to produce parts with tolerances as tight as $\pm 0.12mm$ [65]. Thus, these casting methods have a high potential to be exploited when it comes to small

feature sizes and mini/micro-scale casting. Due to the aforementioned reasons, we will focus on these two casting techniques herein.

Die Casting

Die casting is a permanent-mold casting method where the molten metal is injected into the mold cavity under high pressure. The pressure is typically in the range of 7-350 MPa and will be maintained until the solidification process is complete. The high-pressure injection of molten metal distinguishes die casting from other permanent-mold casting techniques [65]. Microcasting is capable of producing feature sizes as small as 200 μm [66]- [67], and aspect ratios as high as 8-9 [68]. High production efficiency, high part production repeatability, and mold reusability come together in the die casting process. These characteristics make die casting one of the most suitable ways of high-volume heatsink production. However, the process is not economical for low-volume production due to the cost of the permanent mold. Die casting poses some limitations on the features that could be available in the part, such as undercuts. This is due to the fact that the part should be removed from the mold in a non-destructive fashion. Another downside of casting processes is that cast parts generally have a lower density than extruded or forged billets. Therefore, lower thermal conductivity can be achieved compared to the machining process [64].

Investment Casting

Investment casting is a manufacturing process in which a pattern/dummy [1] made of wax or plastic is coated with a layer of refractory material (usually ceramic powder)

---

[1]"A full-sized model of the part, enlarged to account for shrinkage and machining allowances in the final casting." [65]

to form the mold. The mold is then held in an inverted position and heated. The sintering process increases the ceramic mold's strength and melts out the pattern (the process is also known as lost-wax process). Once the mold is preheated, molten metal is poured into the mold, where it solidifies. The mold is then broken away from the part [65]. Normally, in high-volume production, multiple patterns are located on a spur to make a pattern tree, and the mentioned steps are applied to the tree to make multiple parts at the same time. A step by step illustration of this process is shown in figure 3.3.
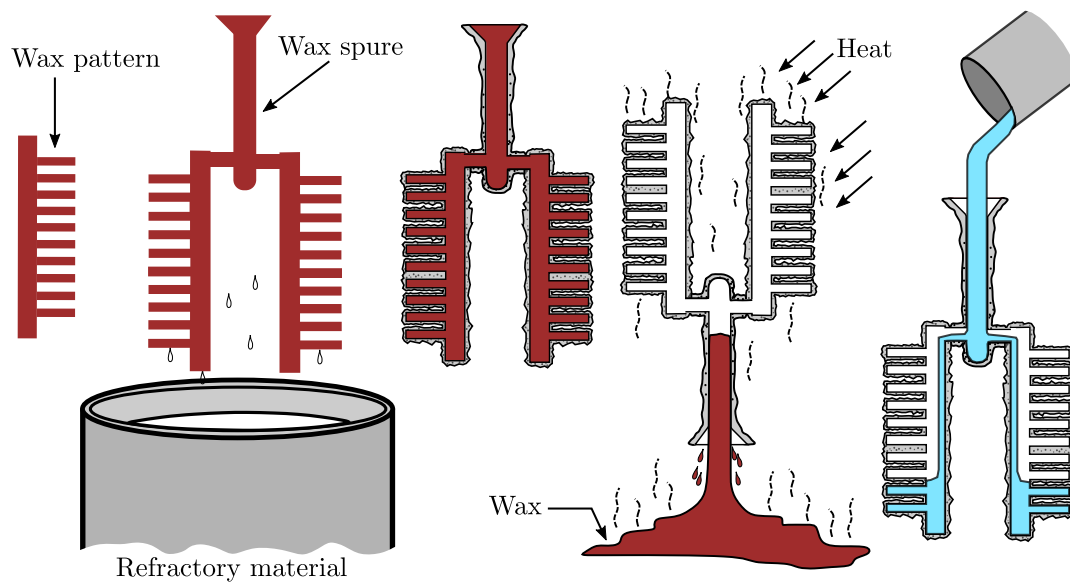
Figure 3.3: Schematic of investment casting processes (adapted from [65])

3.2.3   Powder Injection Molding (PIM)

This method consists of three main processes: (1) Mixing and blending of the powder metal and binder in a blending device such as a screw mixer. (2) The mixture is then heated to the mold temperature and injected into a mold cavity. Then the part will be cooled and removed from the mold. (3) The binder is removed using thermal

or chemical solvent techniques. (4) The part is sintered. The binder has two main objectives in the process: (1) To give the powder metal proper flowability, and (2) Keep the powders in the mold shape until the part is sintered. PIM and μPIM are suited for small complex parts that have a high value [65]. The process of PIM is illustrated in figure 3.4. A screw mixer is used in this illustration. Normally, the powder is heated while it is moving forward in the screw mixer using some heaters on the periphery of the screw. The screw maintains pressure on the filled up mold so that the powder and binder are properly compressed.

As with casting, shrinkage and porosity exist in PIM parts due to the nature of the process. However, PIM has the advantage of lower mold temperature due to the fact that mold temperature does not have to be as high as molten metal. This allows for using a wide variety of materials for the mold [64]. It has been shown that μPIM is capable of creating stainless steel cylinders as small as 100 μm in diameter and 200 μm in height [69].
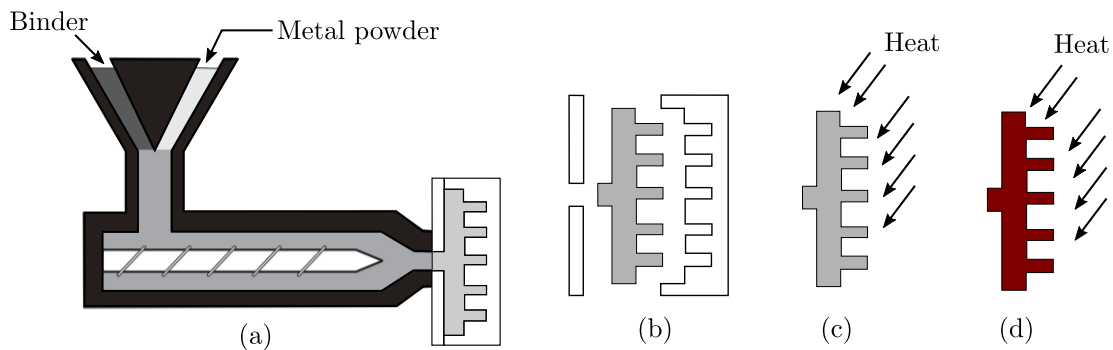
Figure 3.4: Schematic of powder injection molding process:
(a) Injection of powder binder mixer into the mold cavity, (b) Removing the mold,
(c) Removing the binder by heating, (d) Sintering of the part (adapted from [64])

3.3   Advanced Manufacturing Methods

3.3.1   Electric Discharge Machining (EDM)

Electric Discharge machining (also known as EDM) is one of the most widely used advanced manufacturing processes. Wire EDM, EDM milling, and die-sinking EDM are three well-known categories of EDM. EDM, in its most basic form, includes an electrically conductive material (such as graphite, brass, copper, copper tungsten, silver tungsten, and etc.) that acts as an electrode and a blank workpiece. An electric voltage is applied between the electrode (tool) and the workpiece while two parts are moving against each other and maintaining a small gap in between. The process takes place in the presence of a dielectric fluid. The electric discharge causes a spark between the material and the workpiece that makes the dielectric ionized. The ionized fluid creates a path for discharging energy to be directed toward the workpiece. This energy creates a local high-intensity hot spot that removes material from the workpiece. The dielectric fluid washes the chips/particles away from the workpiece and cools down the heat-affected zone. The tool is now at a greater distance with respect to the workpiece. Therefore the tool moves down step by step, and the same process happens over and over again until the workpiece is eroded to the final desired shape. The surface finish of the fabricated part is dependent on the discharge current and frequency [65].

Die Sinking/Sinker EDM

In die-sinking EDM, the tool has the inverse shape of the cavities in the final part. Die sinking is able to create complex geometries repeatedly in high-volume [64]. In

cases where circular pin-fin shapes are used in a heatsink, the die shape becomes the opposite of the pin-fin array. Therefore, die fabrication can be done quite conveniently by drilling some holes into the tool. This is illustrated in figure 3.5a. Once we use this shape as the tool, the pin-fin array can be manufactured in a single operation, as shown in figure 3.5b. It is noteworthy that the tool does not necessarily need to be as large as shown here. In fact, a smaller tool that can make only a portion of the pin-fin array will work as well. The entire heatsink can be fabricated by repeatedly sinking such a tool in the workpiece to make the desired pattern.

Die sinking tool

Blank workpiece

Pin-fin heatsink

(a) Plunging female die into workpiece

(b) After die sinking when male part is created
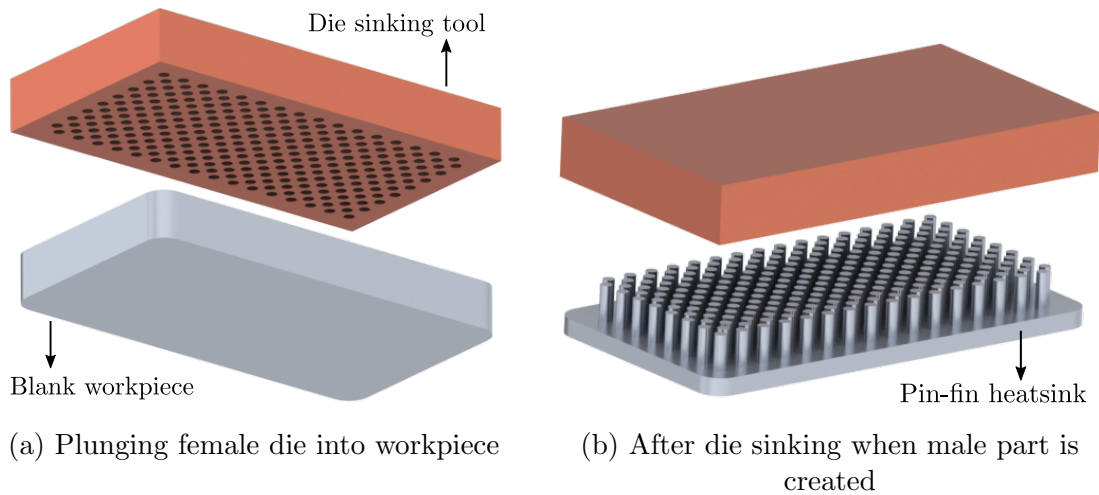
Figure 3.5: Die sinking EDM process

Other fin geometries are also manufacturable with die sinking methods such as offset strip pin-fins with rounded edges. In the following section, we will see that such fin geometry is considered as a design candidate for the comparative analysis. Typically, machining is utilized to fabricate the tool/die. Therefore, pocket milling is the dominant method of die fabrication. Since internal sharp edges are not manufacturable in pocket milling, fin geometries that have sharp edges pose a limitation

to die fabrication. However, wire EDM can be used to tackle this problem.

Wire EDM

Electric Discharge Wire Cutting (EDWC), also known as wire EDM, utilizing a small diameter wire to cut the workpiece. The basics of cutting operation are the same as what is already mentioned. The most important feature of this type of EDM is that it can only create through-thickness cuts or slots. Figure 3.6a is an illustration of the wire EDM process. The tool/workpiece interface is either submerged in the fluid or impinged by a fluid jet. The wire is continuously fed from a supply spool to refresh the cutting electrode. Wire EDM is analogous to bandsaw operation, although it is much more precise than bandsaw with much narrower overcut [65]. Wires can have diameters as small as 20 μm so, the process is well capable of producing feature sizes both in mini and micro scale fin manufacturing [70].

As seen from figure 3.6a , non-standard fin shapes can be created using this method. These fins can then be plunged into a die to form a die-sinking tool. That is why theoretically, any irregular geometry with sharp edges can be created using EDM. However, in the case of non-standard fin shapes, it is more sensible to use machining or casting to reduce the number of manufacturing steps.

EDM Milling

EDM milling, in its essence is quite similar to typical end-milling except that instead of mechanical material removal, an electrical discharge is used to mill out the workpiece. The tool apparently is a cylindrical electrode. According to [64], micro-EDM milling and drilling can have electrode diameter as tiny as 5-10 μm and high aspect ratios

(a) Wire EDM process (adapted from [65])   (b) EDM milling process
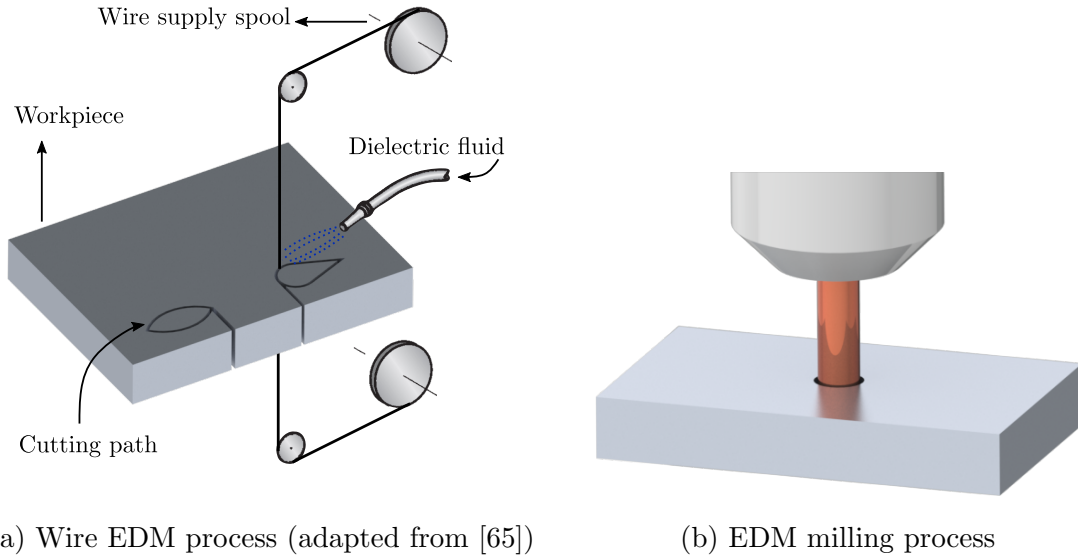
Figure 3.6: Illustration of two EDM processes

such as 20 have been achieved. Figure 3.5a represent the EDM milling process.

3.3.2   Etching

Etching is generally referred to photo-lithographic-bases methods. The family of these processes are primarily utilized for microfabrication and are widely used in the fabrication of integrated circuit boards and microelectromechanical systems. A well-known technique of this family that is suited for metallic heatsink manufacturing is the lithography electrodeposition-based technique of LIGA [2].

The LIGA process consists of four main steps: (1) A thick layer of radiation-sensitive resist (usually x-ray radiation is utilized) is applied to an electrically conductive substrate. A common material for the resist layer is Polymethyl Methacrylate

---

[2] "LIGA" stands for the German expression "LIthographie, Galvanoformung, und Abformtechnik" [65].

(PMMA). The resist is then exposed to x-ray radiation through a mask. (2) The irradiated areas of the positive resist are then removed from the substrate. (3) The regions where the resist has been removed from a cavity just like a mold. These regions are filled with metal using electrodeposition or electroplating. (4) The remaining resist mold is then removed or dissolved, resulting in the final 3D metal component [64], [65]. Different steps of the LIGA process are illustrated in figure 3.7.
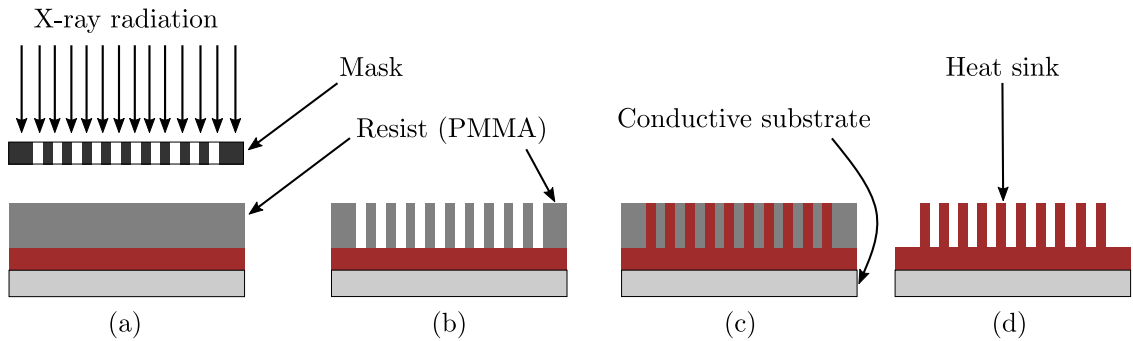
Figure 3.7: LIGA processing steps: (a) Expose photoresist to high energy x-ray radiation, (b) x-ray exposure removes material from the resist layer and forms a mold, (c) metal is deposited into the mold using electrodeposition, (d) remove the remaining resist (adapted from [64])

Common metals produced using the LIGA process include nickel and copper. Moreover, LIGA is capable of producing complex nonstandard geometries with aspect ratios as large as 60. This makes the LIGA process well suited for the fabrication of complicated optimized finned heatsink geometries [64]. Additionally, a wide range of part sizes ranging from micrometers to centimeters can be manufactured in this process. However, the LIGA process is significantly expensive, making it hard to have a sensible return on investment (ROI) for low-volume production. Thus, this method can only be justified for high-volume production [65].

3.3.3   Metal 3D-printing

Metal 3D-printing is capable of producing complex heatsink geometries as a single piece, which is a significant advantage over other traditional fabrication methods mentioned herein. Due to the conductive nature of the heatsinks in general and the power module's baseplates in particular, high thermally conductive materials should be used for the heatsink's base section, making it hard to use any material other than copper or aluminum. Additive manufacturing (AM) of these metals is yet premature to entirely overthrow conventional manufacturing methods. A substantial amount of research on the AM methods of these metals and their thermo-mechanical properties is ongoing for the mentioned reason.

The most common aluminum alloys for 3D-printing are AlSi10Mg and AlSi12. Aluminum has both high reflectivity and thermal conductivity. High thermal conductivity makes it hard to focus the laser energy in a particular area (melt pool) for material deposition. High reflectivity causes a significant amount of laser energy to be reflected off the powder bed. These two characteristics of aluminum cause a high level of porosity and poor thermo-mechanical properties in 3D-printed aluminum alloys [71]. To decrease aluminum's reflectivity and thermal conductivity, Silicon is added to the composition; therefore, silicon is an integral part of these alloys. However, as mentioned, silicon content reduces the aluminum alloy's thermal conductivity, which makes it less favorable for heatsinking application [72]. In conclusion, due to having a lower level of silicon content, AlSi10Mg is more favorable than AlSi12 for our purpose.

As mentioned earlier, aluminum has a high reflectivity; however, this reflectivity

depends on the wavelength of the laser as well, making some AM methods less favorable than others. For example, aluminum has a high reflectivity for the wavelengths usually applied in Laser Beam Melting (LBM) and Laser Metal Deposition (LMD). Thus, these processes are not entirely desirable for AM of aluminum. LBM is , however, LBM is more desirable than LMD since the low viscosity of molten Al makes it limited to small melt pool sizes. The combination of AlSi10Mg and LBM is one of the most dominant combinations in AM of Aluminum. [71].

Selective Laser Melting (SLM) is also one of the most common 3D-printing methods of Al alloys. Full melting happens in SLM, whereas in Selective Laser Sintering (SLS), local metal sintering happens at low temperatures to initiate fusion of the powder. Therefore, for enhanced thermo-mechanical properties, SLM is preferred over SLS [73].

Wu et al. compares the material composition of 3D-printed AlSi10Mg against the composition of Al6061, which is widely used in power electronics heat sink application and states that the 3D-printed version is the equivalent of Al6061 in terms of the composition [74]. Moreover, Madhu et al. have concluded that the strength of additively manufactured AlSi10Mg is quite similar to 6061 alloys [75]. Aluminum 3D-printing creates a huge potential for the fabrication of complex heatsink geometries that would not have been manufacturable otherwise. However, this advantage is accompanied by the downside of poor thermal and mechanical properties compared to other fabrication methods. Thus, more research should be focused on enhancing the material properties of the as-built sample through post-processing, such as heat treatments.

3.3.4   Post-processing Heat Treatments of AM Samples

In general, metal AM research can be classified into preprocessing, processing, and post-processing. Preprocessing emphasis is on enhancing powder metal technology. The processing research emphasizes the optimization of the process parameters such as laser power intensity, laser velocity, etc., to enhance the material properties. AM post-processing research relies on the fact that neither pre-processing nor processing step of metal 3D-printing is flawless. The post-processing treatments are there to reduce imperfections and enhance the final properties of the as-built sample. The focus of this research is to investigate potential treatments for specific heatsinking applications. The objective herein is to understand what steps have to be taken towards commercializing metal 3D-printing for electronics' cooling.

A study shows that unlike conventionally manufactured aluminum alloys, SLM counterparts are softened after T6 like heat treatments. This happens because of the difference in the microstructure at the beginning of the heat treatment. The as-built SLM sample shows a high micro and nano hardness due to the extremely fine microstructure produced during the melting process. Once the sample is heated up, the well-distributed Si will be diffused, and coarser particles will form, which might be the reason that the heat treatment acts differently in these alloys. The same inverse effects happen for mechanical strength since the tensile and compressive strength also drops as a result of treatment. The microhardness of the as-built sample (125 HV) was found to be higher than the die-cast counterpart (95-105 HV). However, T6 treatment bumps up the die-cast sample's hardness to (130-133 HV), making it comparable to the as-built AM sample. It is noteworthy that the hardness of the as-built AM sample will reduce roughly 20% after the treatment [76], [77].

Experimental results [78] also corroborate [76] that the very fine structure produced during the SLM process gives the as-built sample a microhardness as high as 127 ± 3 Hv0.5. The study attributes the hardness characteristic of the as-built sample to the fine dispersion of Si in the Al phase [78].

Aboulkhair et al. explain that thermal post-processing has been mostly confined to the conventional heat treatment methods, whereas AM alloys have a completely different microstructure than their conventional counterparts. Since these thermal post-processing treatments such as annealing, solution heat treatment , and precipitation hardening (T6 solution heat treatment and then water quenching and artificial aging) are particularly tailored for traditional Al grades, the resulting behavior of AM samples to these treatments is unlike the behavior of conventional Al. The study specifically elaborates on why this happens from the microstructure perspective. According to Aboulkhair's conclusion from a comprehensive review of literature, almost all of the studies show that micro-hardness monotonically decreases as the as-built sample is heat-treated regardless of the heat treatment procedure (annealing, solution heat treatment , and precipitation hardening) [79].

As mentioned in [75] and [79], a similar research shows that in general, hardness, tensile and compressive strength reduces with solution heat treatment and aging. The research states that precipitation hardening leads to the lower solution of Si in Al matrix that causes lower strength and high ductility. The paper explains that the eutectic microstructure of as-built AlSi10Mg gives rise to significantly better tensile properties and Vickers microhardness compared to cast Al [80]. Another study also supports the fact that the hardness goes down as precipitation hardening happens to the SLM sample, which is dissimilar to conventional cast aluminum's behavior [81].
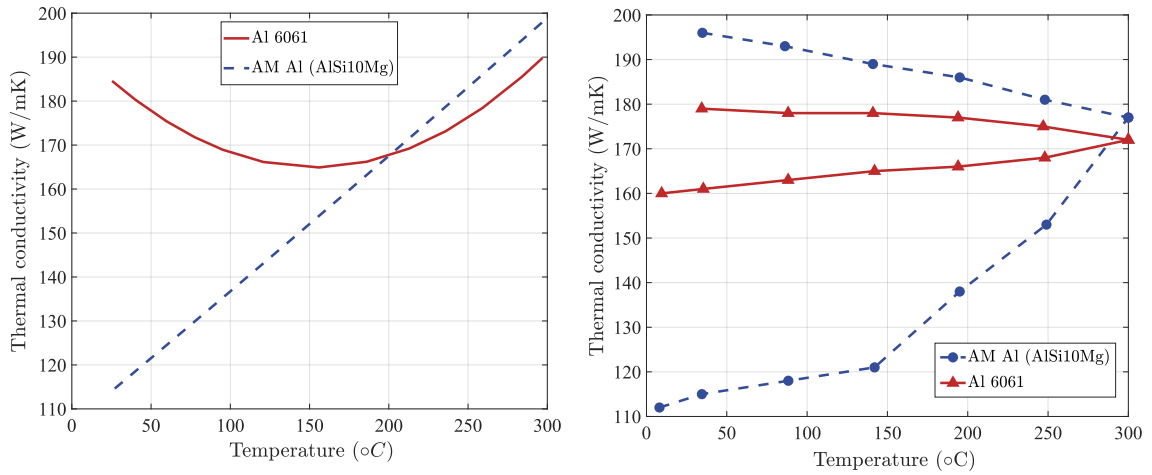
(a) Effect of temperature on thermal
conductivity of AM aluminum and Al6061

(b) Heat treatment effect on thermal
conductivity of AM aluminum and Al6061

Figure 3.8: Thermal conductivity against temperature (adapted from [74])

Another challenge in the way of using 3D-printed AlSi10Mg is the thermal conductivity. As discussed before, high thermal conductivity is desired for the cold plate's baseplate. However, due to the Si phase available in the AM alloy, thermal conductivity is lower than that of conventional alloys such as 6061 or cast Al. The solution heat treatment leads to the lower solution of Si in Al matrix; therefore, it will be expected that the thermal conductivity would increase with solution heat treatment. A thermal conductivity experiment is done in [74] that proves the latter point. The result of the test is shown in figure 3.8a. As shown in figure 3.8a , as the AM part is heated up, the thermal conductivity becomes close to the conductivity of Al6061. Nearly above 190 ℃, the AM aluminum has a thermal conductivity close to and even higher than that of 6061. Since the operating temperature in power electronics heatsinks is often lower than 190 ℃ , the researchers have come up with a heat treatment method to permanently improve the thermal conductivity of AlSi10Mg. As shown in figure 3.8b , the sample is first annealed up to 300 ℃ and then subsequently cooled down.

56

As it turned out, this method's resulting thermal conductivity is even higher than Al6061 in the operating temperature of the device.

However, the effect of this treatment on hardness and other mechanical properties were not taken into consideration in the previous study. This investigation is of paramount importance when it comes to productionizing such a design in the automotive sector. Hardness and other mechanical properties significantly contribute to the durability of the design because of the harsh operating condition for the mounting in terms of vibration. The effect of the proposed heat treatment on mechanical properties and where the trade-off lies between thermal and mechanical properties, and how each one is compromised are some important questions. The questions raised are some potential topics of interest for future investigation. Advancements in answering these questions may be a key enabler for widespread adoption of metal 3D-printing in heatsink manufacturing.

3.4   Discussions

Potential fabrication methods that are capable of heat sink manufacturing are discussed. Particular attention is given to baseplate (integrated pin-fin) manufacturing. Therefore, fluid enclosure manufacturing was not the topic of discussion. Possible feature sizes and aspect ratios that are feasible in each fabrication method are discussed. The advantages and downsides of each technique are briefly mentioned. A separate section is dedicated to metal 3D-printing and the potential heat-treatment processes that can enhance the thermo-mechanical properties of as-built additively-manufactured samples. This is due to the fact that additive manufacturing is capable of manufacturing complex geometries as a single piece and is becoming more common

as a mass production manufacturing method. It is worth mentioning that normally a heatsink is fabricated using a combination of the mentioned fabrication techniques. Depending on the required tolerance and surface finish of the part, two or more manufacturing method may be used to achieve the target quality. It is worth mentioning that the list of fabrication methods discussed herein is non-exhaustive. Other fabrication methods such as extrusion, rolling and stamping, and forging are employed in heat sink manufacturing. It is of paramount importance to precisely consider the production rate and capacity when selecting each one of these techniques. Figure 3.9 represents a summary of the production suitability of each of the fabrication techniques both for prototyping and mass production.
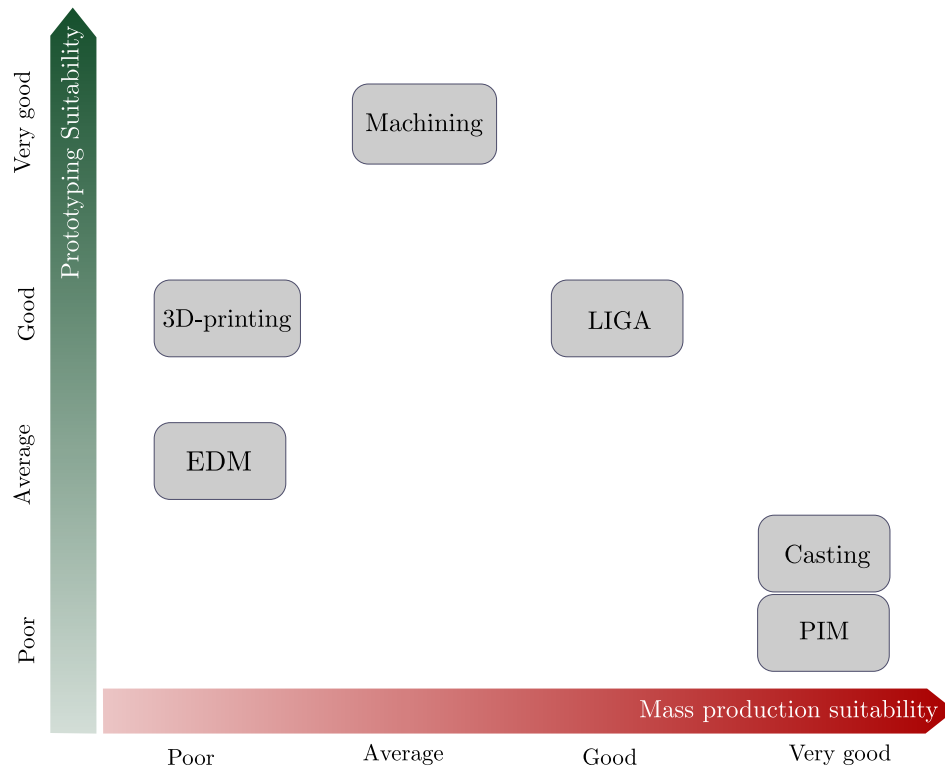
Figure 3.9: Production suitability of various heat sink fabrication processes (adapted from [64])

Chapter 4

Finned-type Heatsink Design for Power Electronic Modules

Finned-type heat sinks are extremely beneficial in the power electronic industry in general and specifically in the automotive sector. In this chapter, an electrical model of a power module for traction inverter application is first provided. The power loss is then obtained using the representative power module datasheet along with PLECS and Matlab simulation. An overview of the power module's state-of-the-art packaging technologies is presented afterward. Then some assumptions about the substrate of the power module are outlined. A comprehensive overview of pin fin shapes is then presented, and some shapes are selected for the comparative analysis. Then the methodology of the comparative analysis is discussed. The CFD simulation, including the CAD model, theory, turbulent modeling method, and boundary conditions, is discussed in depth in the next few sections.

4.1   Power Loss Calculation
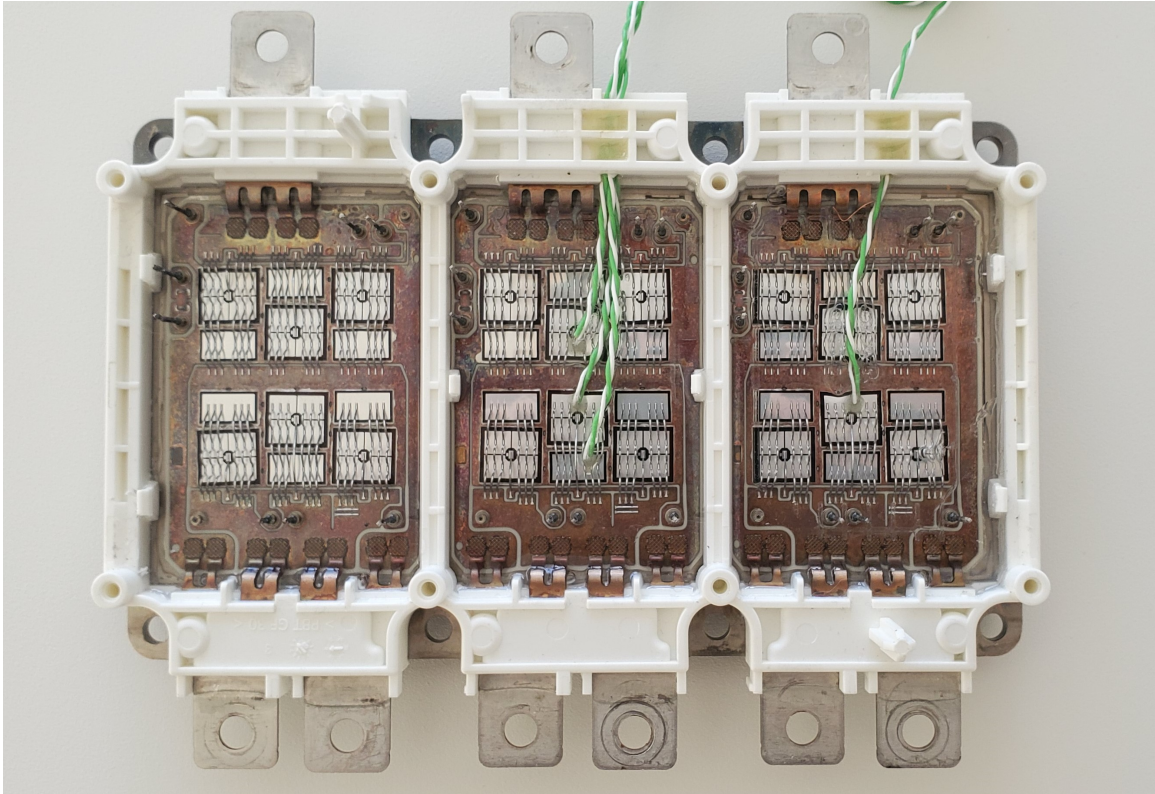
Figure 4.1: An unpacked representative power module

4.1.1   Assumptions

First and foremost, it is assumed that the power module will be used in automotive traction inverters. Thus, the module's power and current rating, efficiency, power loss, operating condition, and cooling medium are specifically tailored for such application. It is also noteworthy to mention that the power module's power losses are calculated based on the assumption that the traction inverter will run a 160 kW (continuous power rating) permanent magnet electric machine. Consequently, the power factor
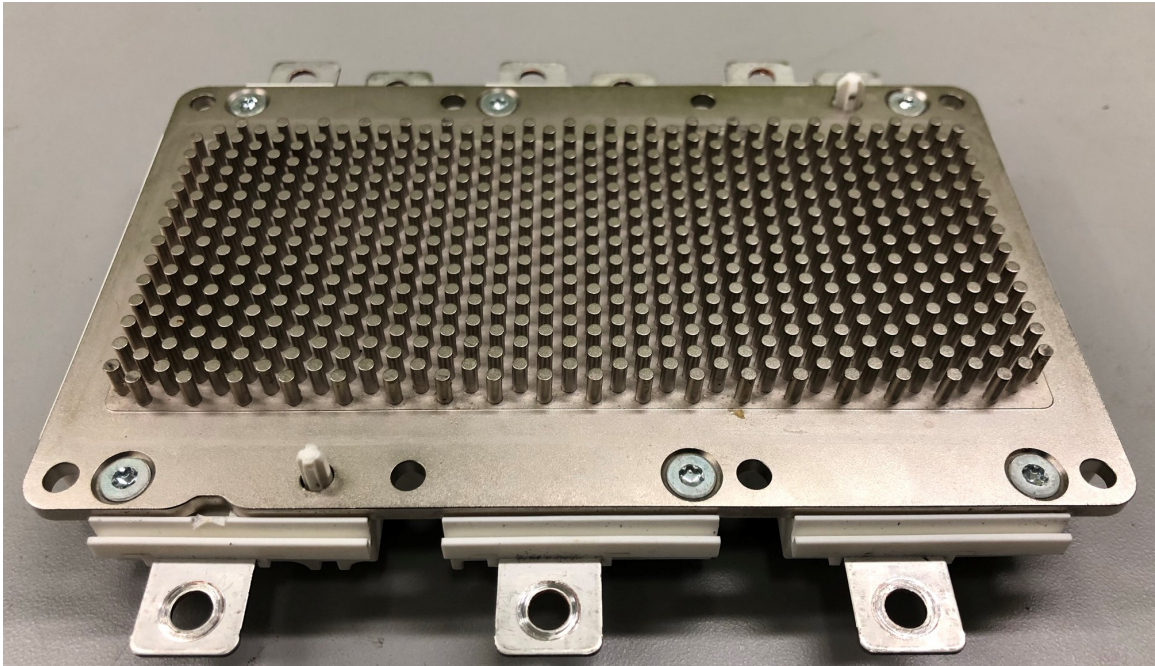
Figure 4.2: Pin-finned baseplate of the representative power module

is assumed to be 0.9. A power module manufactured by Infineon technologies will be used as a representative power module for the current study's simulation-driven heatsink design (*Infineon* FS380R12A6T4B HybridPACK™ Drive Module) [82]. The machine is going to be run with a three-phase two-level inverter in voltage source configuration, which is the primary configuration in which the module has to operate. The dc-link voltage is assumed 800 V. The switching frequency is assumed to be 10 kHz. The required RMS phase current rating is 200 A RMS. A schematic of the inverter topology is shown in figure 4.3. As shown in the figure, there are three phase legs in the inverter. Each phase leg contains an upper and a lower switch that is turned on and off alternately. Additionally, a diode is antiparallel to each semiconductor switch. The upper and lower switch does not conduct current simultaneously during operation to prevent the DC source from being shorted [1].

The inverter power loss consists of conduction and switching power losses. These types of power losses are briefly discussed in the next sections, and the power loss calculation method is outlined.
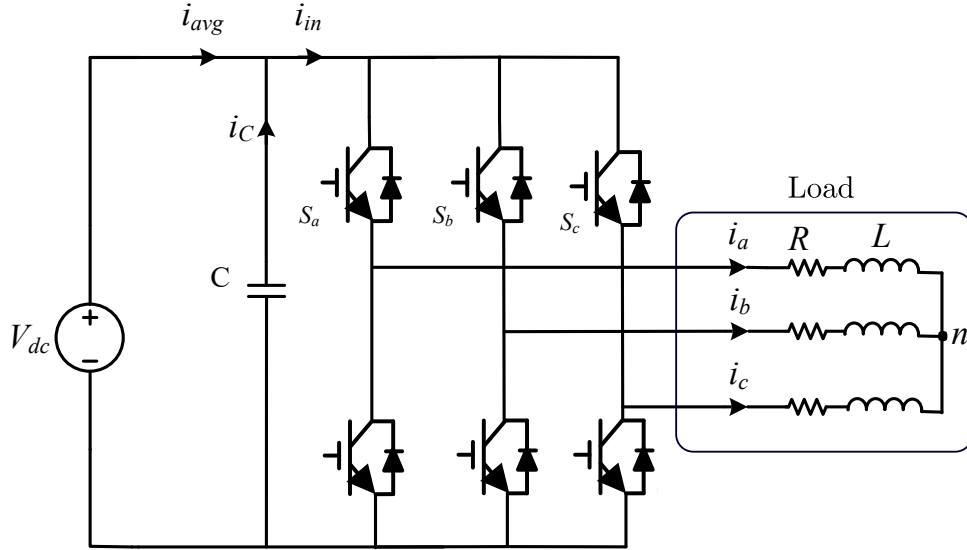
Figure 4.3: Topology of three-phase two level voltage source inverter

4.1.2   Conduction Losses

The conduction power loss is the portion of the power loss that is created when the semiconductor device (Insulated-Gate Bipolar Transistor (IGBT) in this case) is on.

During the on-state condition, the equivalent circuit of IGBT consists of a junction temperature-dependent resistor connected to a DC voltage source in parallel. The schematic of the equivalent circuit is illustrated in figure 4.4 The diode has a similar equivalent circuit in the on-state condition.
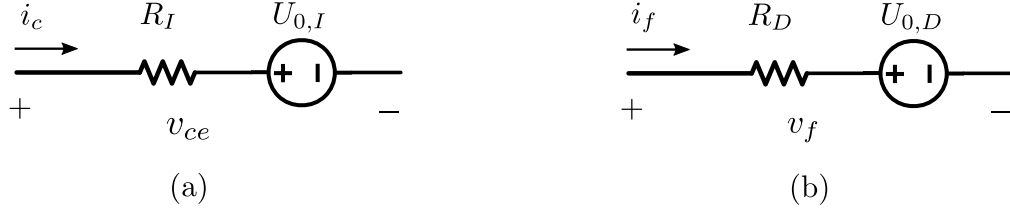
Figure 4.4: a) Equivalent circuit of an on-state IGBT, b)Equivalen circuit of an on-state diode (adapted from [1])

IGBT and diode conduction losses can be obtained in a similar fashion from the following equations:

$$P_{c,I} = I_{rms,I}^2 \cdot R_I + U_{0,I} \cdot I_{ave,I} \tag{4.1.1a}$$

$$P_{c,D} = I_{rms,D}^2 \cdot R_D + U_{0,D} \cdot I_{ave,D} \tag{4.1.1b}$$

Where $U_{0,I}$, R_I, $U_{0,D}$, and R_D are given by the module datasheet. $I_{rms,I}$ and $I_{avg,I}$ are RMS and average switching currents. $I_{rms,D}$ and $I_{avg,D}$ are RMS and average currents of the diode. Average and RMS currents of IGBT and diode can be obtained from the following equations [1]:

$$I_{ave,I} = \frac{I_{rms}}{\sqrt{2} \cdot \pi} \cdot \left(1 + \frac{\pi \cdot M \cdot \cos\phi}{4}\right) \tag{4.1.2a}$$

$$I_{rms,I} = \frac{I_{rms}}{2} \cdot \sqrt{1 + \frac{8M \cdot \cos\phi}{3\pi}} \tag{4.1.2b}$$

$$I_{ave,D} = \frac{I_{rms}}{\sqrt{2} \cdot \pi} \cdot \left(1 - \frac{\pi \cdot M \cdot \cos\phi}{4}\right) \tag{4.1.2c}$$

$$I_{rms,D} = \frac{I_{rms}}{2} \cdot \sqrt{1 + \frac{8M \cdot \cos\phi}{3\pi}} \tag{4.1.2d}$$

Where I_{rms}, M, and $\cos\phi$ are inverter output RMS current, modulation index, and power factor, respectively.

4.1.3   Switching Losses

The switching power loss refers to the power losses generated during the switching transient (on/off). The inverter's total power loss is equal to the amount of power loss generated by the six switching devices and six diodes all together.

IGBT switching power losses can be obtained from the turn-on and turn-off energy losses ($E_{on,I}$, and $E_{off,I}$) and switching frequency (f_{sw}) through the following equation:

$$P_{sw,I} = (E_{on,I} + E_{off,I}). \ f_{sw} \qquad (4.1.3)$$

Average $E_{on,I}$, and $E_{off,I}$ values can be obtained as follows:

$$E_{on,I} = \frac{\sqrt{2}}{\pi} \frac{I_{rms} \cdot U_{dc}}{U_{ref} \cdot I_{ref}} \cdot E_{on,ref} \qquad (4.1.4a)$$

$$E_{off,I} = \frac{\sqrt{2}}{\pi} \frac{I_{rms} \cdot U_{dc}}{U_{ref} \cdot I_{ref}} \cdot E_{off,ref} \qquad (4.1.4b)$$

Where U_{ref} and I_{ref} are the reference operating conditions in which the reference values of turn-on and turn-off energy ($E_{on,I}$ and $E_{off,I}$) are reported in the module's datasheet.

Diode switching losses are mainly due to the reverse recovery during the turn-off transition. The diode turn-on energy loss is negligible compared to the reverse recovery energy loss (E_{rr}). The method of determining E_{rr} is similar to the method of deriving $E_{on,I}$ and $E_{off,I}$. Thus, the average reverse recovery energy can be obtained as follows [1]:

$$E_{rr} = \frac{\sqrt{2}}{\pi} \frac{I_{rms} \cdot U_{dc}}{U_{ref} \cdot I_{ref}} \cdot E_{rr,ref} \qquad (4.1.5)$$

Where U_{ref} and I_{ref} are the reference operating conditions in which the reference

value of reverse recovery energy ($E_{rr,ref}$) is reported in the module's datasheet. The total power loss of the inverter can be computed using the following relations [1]:

$$P_c = P_{c,I} + P_{c,D} \tag{4.1.6a}$$

$$P_{sw} = P_{sw,I} + P_{sw,D} \tag{4.1.6b}$$

$$P_{loss,inverter} = 6(P_c + P_{sw}) \tag{4.1.6c}$$

The electrical model of the inverter is implemented in Matlab Simulink using a PLECS blockset. The temperature-dependent properties of the power module such as $E_{on,I}$ are imported to PLECS blockset. An open loop control is emplemented using SVPWM modulation scheme. A simple 1D thermal network is used based on the datasheet's thermal resistance characteristic curves to predict the junction temperature. The junction temperature is fed back to the electrical model to compute temperature-dependent variables. Lastly, proper averaging operations and power loss calculations are done. Table 4.1 is the summary of the power loss calculation results. It is worth noting that the power loss calculation is done for the worst-case power loss scenario.

Table 4.1: Power loss calculation results

Power loss	IGBT	Diode
Conduction (W)	137	10
Switching (W)	437	163
Total (W)	574	173
Total power loss per phase leg (W)	1494	
Total inverter loss (W)	4482	

4.2   Power Module's Packaging

Conventional power modules' packages consist of several diodes and IGBT chips (also known as dies), which are electrically parallel and soldered (die attachment) to a substrate. The substrate is typically made of a thermally conductive and electrically insulating ceramic sandwiched between two copper layers. This type of substrate packaging technology is called direct copper bond (DBC). Then, the entire package, including the chip, the solder, and the DBC, is soldered to a copper baseplate. Copper busbars and aluminum wire bonds connect the die, substrate, and module terminals. [83], [84]. A soft silicon gel, sometimes along with a hard epoxy resin, contains the dies for protection from humidity and contamination [84]. Copper layers of the DBC and the baseplate spread the heat over a much larger area than the chip surface area to make temperature distribution more uniform and reduce the need for hot spot cooling.

A typical power module package with direct bond copper (DBC) substrate is shown in the figure 4.6 on the left side, with the corresponding power package on the right side. Aluminum wirebond die connections, and silicon gel encapsulation are shown in the figure 4.5.

In general, a wide variety of packaging technologies and bonding materials and methods are being used for die attachments and substrate layers in the power modules. There is a bonding method where a thermally conductive epoxy attaches the semiconductor die directly to the lead frame. Some technologies such as soldered interconnection have been introduced as a substitution to wirebond connections to [83]. Direct Bonded Aluminum (DBA) is also another type of substrate which is less common than DBC substrate. Active Metal Brazing (AMB) is another method of bonding
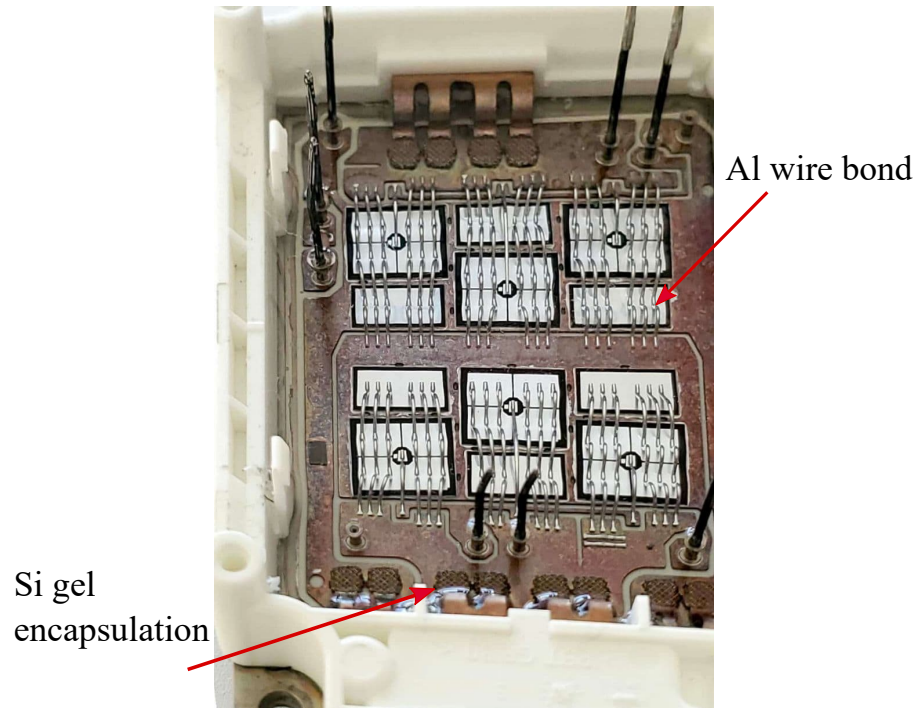
Figure 4.5: A phase leg of the representative power module

the ceramic to metal sublayers. The process removes the oxidation layer therefore, enhances the module in terms of thermal cycling capability [85]. AMB method is specifically useful when it comes to Silicon Nitride (Si_3N_4) ceramic. This combination has shown superior thermal cycling ability in comparison to other ceramic metal bondings. Table 4.2 summarizes some of the most important thermo-mechanical properties of commonly used ceramic materials in power electronic applications [86]. It can be inferred that silicon nitride has almost all of the desired properties of an insulating ceramic such as high strength, low thermal expansion and a fairly high thermal conductivity.

A substantial amount of research is being done on the advanced material, manufacturing, and packaging aspects of semiconductor devices. Conventional silicon(Si)

Table 4.2: Properties of ceramic material in power modules' substrates

Ceramic material	Thermal Conductivity (W/m.K)	Thermal expansion (10^{-6}/K)	Tensile strength (MPa)
Al_2O_3	24	6.8	400
AlN	170	4.7	270
HPS	28	7.1	600
Si_3N_4	60	3.4	800

devices have been dominating power electronic modules for years. However, recent advances in Wide Band Gap (WBG) power semiconductor devices and their manufacturing technology have introduced promising replacements for traditional Si devices. Studies show that WBG semiconductors such as Silicon Carbide (SiC) and Gallium Nitride (GaN) outperform the traditional Si devices by every performance metric [87], [85]. However, due to the challenges in the packaging technology, the potentials of these devices are not yet widely realized in the application [85]. Yang et al. has presented an in-depth review of the current status and future automotive power module packaging technologies [88] trends. Chen et al. have reviewed various packaging technologies and materials for SiC power devices [85].
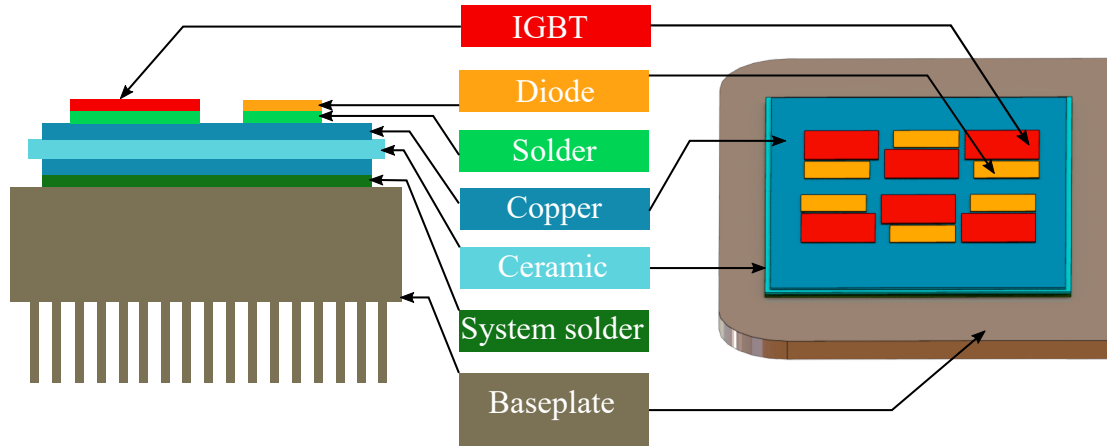
Figure 4.6: Schematic of a the thermal stackup of the representative power device

For this analysis, the chip layout is obtained from the unpacked power module measurements shown in figure 4.1. The off-the-shelf power module has circular pin-fins integrated into the module's baseplate (figure 4.2); therefore, using this module is beneficial in terms of having a baseline design to improve upon it. The material properties and thicknesses of the power devices and substrate layers are based on the typical measures and information available in the literature. Typical values for the DBC substrate thicknesses in IGBT power modules are quite standard. The copper and ceramic layers are generally 0.3 mm and 0.32 mm thick, respectively. Chip solder and system solder (or DBC solder) are typically 0.2 mm, and 0.09 mm thick, respectively [89]. The thickness of the IGBT and diode dies are assumed to be 0.08mm. It is assumed that Silicon Nitride is used for the ceramic layer of the DBC due to the superior thermo-mechanical properties that were mentioned earlier. Table 4.3 shows the thermal and mechanical properties of different layers of the power

Table 4.3: Assumed properties of the thermal stackup for the representative power device

Layer	material	Thickness (mm)	ρ (kg/m^3)	C_p $(J/kg.K)$	k $(W/m.K)$
1	IGBT (Silicon)	0.08	2330	700	130
2	Diode (Silicon)				
3	IGBT Solder	0.09	9000	150	50
4	Diode Solder				
5	DBC (Copper)	0.3	8940	385	385
6	Ceramic (Si_3N_4)	0.32	3290	711	80
7	System solder	0.2	9000	150	50
8	Baseplate (Copper)	3	8940	385	385
9	Pin-fin (Copper)	6			

device that are assumed for the simulations. The table includes assumed thickness, density (ρ), specific heat (C_p) and, thermal conductivity (k) of each substrate layer [86], [89], [6], [90], [91], [92].

4.3   Pin-Fin Designs

This study aims to investigate the effect of the fin shape in a particular layout of fin arrays (staggered pin-fin array) on the thermal-hydraulic performance of the heatsink. Manufacturability constraint is considered in the form of a minimum distance between the fins in the fin array. Ideally, it is desired to compare heatsinks that have rather comparable manufacturing costs. In this case, we have considered machining as the primary way of fabricating the heatsink. Since the machining cost is generally proportional to the machining time and the downtime that is associated with the setup and tooling step. In our case, since all of the baseplate pin-fins can be manufactured in a single setup, the effect of setup time will be ruled out of the cost comparison. The minimum distance between the fins specifies the diameter of the endmill that will be used for the material removal from the baseplate. In general, the minimum distance values that are being used in this study are smaller than the smallest endmill sizes that are handled in typical machine shops. Therefore, micromachining is the appropriate choice for such baseplates. For the comparison, we will use a variety of design shapes as design candidates. Then computational fluid dynamic (CFD) analysis will be conducted on each design candidate, and the results will be compared in terms of the performance metrics discussed in 2.2.

4.3.1   Overview of Pin-fin Shapes

In this study, the main focus is to investigate the effect of five different fin geometries and compare them. The baseline pin-fin geometry is circular. There are a few reasons behind such a decision. The first and foremost reason is that there is a significant amount of research available in the literature for this geometry; therefore, it will be

quite feasible to do analytical-based or experimental-based validation for circular fin arrays.

Circular Fins

The research relevant to circular pin-fin arrays can be found with the "tube bank" keyword in the literature and heat transfer textbooks. In shell and tube heat exchangers, there is usually an array of tubes surrounded by fluid, and the fluid in the tube will be heated up or cooled down by the convection mechanism happening on the tubes' outer surface. In general, based on the flow arrangement, heat exchangers are categorized into concentric-tube and cross-flow heat exchangers. In the concentric-tube heat exchanger, cooling and heating agents are flowing in directions parallel to each other (either in the same direction or in opposite directions). In cross-flow heat exchangers, on the other hand, the flow arrangement of the cooling/heating agent is perpendicular to the direction of the fluid flowing in the tubes. The governing equations in the cross-flow heat exchangers quite resemble the governing equations of the flow around pin-fin arrays. Since the cross-flow heat exchanger is commonly used in HVAC systems, the empirical and analytical expressions for tube banks are pretty mature because they have been validated and used for decades [93], [94].

Circular shaped fin is commonly used in power electronic modules' cooling for the relative ease of manufacturing. However, a major downside of the circular pin is that the flow separation happens quite easily over the fin's surface, which results in a recirculation zone behind the fin. This comes with the high penalty of increasing the pressure drop and decreasing the heat transfer coefficient. This has been rational for thermal researchers to investigate oblong-shaped fins as opposed to circular fins.

Elongated fins are proven to outperform circular fins when the flow direction is parallel to the major axis of the fins [95]. For instance, Li et al. have compared circular and elliptical fins under the condition of having the same fin circumferential area (equivalent to pin fin perimeter in case of extruded fins). They have concluded that not only elliptical pin configuration has a lower pressure drop but also has a lower thermal resistance, which makes it far more favorable than circular fins [96].

Cone Shaped Fins

The definition of cone fin in pin-finned heatsinks is different than the mathematical definition of the cone. In general any shape that is referred to as "pin-fin" or "fin" in this study is an extruded cross section meaning that the cross section of the fin will be kept constant at different heights.

The cone fin as used in [59] consists of a semicircle attached to an isosceles triangle. The attachment is done in a way that the semicircle diameter is lined up with the base side of the triangle. The cross-section of a cone fin is shown in 4.7a along with an isometric view of a cone fin in 4.7b. The authors in [57] and [61] have utilized this definition of cone fin consistently in their work.
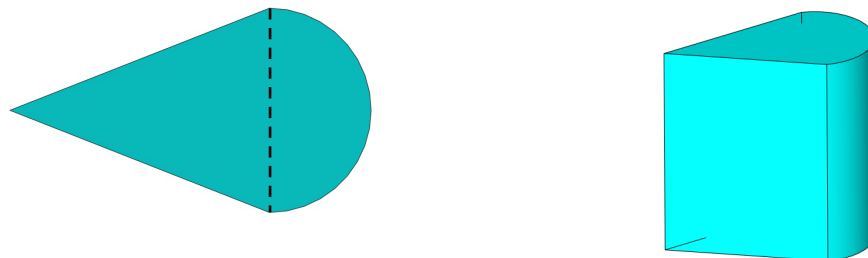
(a) Cone shaped fin (adapted from [59])   (b) Cone shaped fin (adapted from [59])

Figure 4.7: Cone shaped pin-fin

Drop shaped Fins

As it is expected from its name, the drop-shaped fin resembles the shape of a drop of fluid. The study [97] has defined the drop-shaped fin to be consisted of a circle and two lines that are tangent to the circle which coincide at one point. Figures 4.9a and 4.9b demonstrate the drop-shaped fin according to this study. This definition has been adopted and used as a drop-shaped fin by [98] and [99]. An earlier study has referred to the shape shown in 4.9c as drop-shaped fin [100]. Altough this fin geometry seems to be different than what is already shown for drop-shaped fin in fact it is quite consistnet with the previously stated drop-shaped definition. If we set set $r = 0$ in 4.9c it will result in the same geometry as illustrated in 4.9a. Fengming Wang et al. in [101] have come up with three different drop-shaped fin designs that have the same cross-section area with different aspect ratios. The aspect ratio increases respectively from shape a to c in figure 4.8.
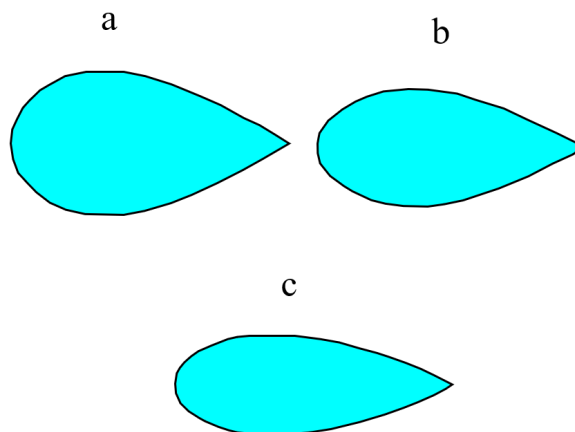
Figure 4.8: Cross section of drop shaped fin (adapted from [101])
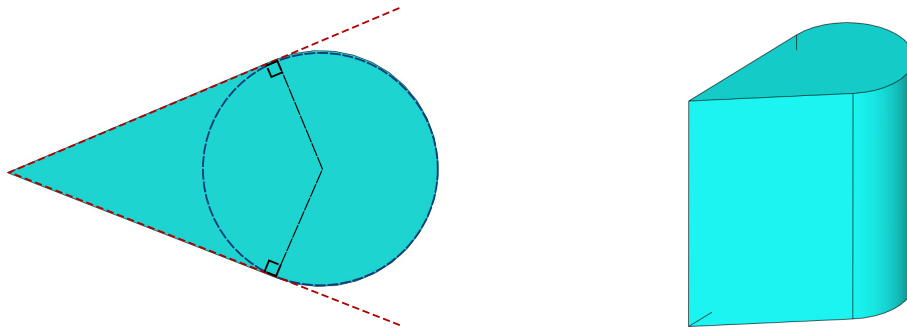
(a) Cross section of drop shaped fin (adapted from [97])

(b) Isometric view of a drop shaped fin
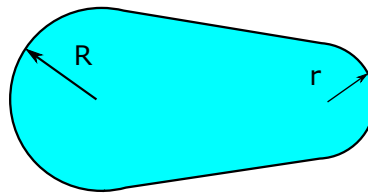
(c) Cross section of drop-shaped fin (adapted from [100])

Figure 4.9: Gometry of a drop-shaped fin

Hydrofoil/airfoil Fins

According to [102]: "A hydrofoil is a shaped blade that is intended to produce lift in exactly the same way as an airplane wing." An airplane wing is essentially an airfoil; therefore, this definition is quite compatible with the "airfoil" definition. Airfoils are also used to produce lift force while minimizing the drag. Hydrofoils and airfoils share the same characteristics, whereas the only difference is that airfoils are built to function in air, and hydrofoils are built to function in a marine application. In

other words, airfoils are being used in airplane wings, and hydrofoils are being used in water wings. For this reason, "hydrofoil" and "airfoil" terms are sometimes used interchangeably. The fact that liquid-cooling performance of pin-fin arrays is the focus of the current study, "hydrofoil" is a proper term when referring to the shapes that are common between hydrofoils and airfoils. However, some researchers have adopted the "airfoil" terminology [95], [103], [104].

It is worth mentioning that in cases where an asymmetrical airfoil/hydrofoil is being used, the asymmetrical shape is there due to the fact that the airfoil is supposed to create a lift force. On the contrary, no lift force is required in the case of using hydrofoil pin-fins for electronics cooling. The point of using such airfoil shapes in pin-fin designs is to increase the surface area in locations where heat transfer happens while minimizing the pressure drop. Thermal designers have come up with the idea of using airfoil/hydrofoil shapes to take advantage of the streamlined character of such shapes to minimize the drag. That is why almost all of the relevant studies have been carried out using symmetrical hydrofoils/airfoils. Symmetrical airfoils/hydrofoils, in general have one or more axis of symmetry. For instance, an asymmetrical airfoil is shown in the figure 4.10 along with a symmetrical airfoil with a horizontal symmetry axis [45].

There are numerous airfoil and hydrofoil standard profiles that are mainly optimized for aerodynamics applications. As mentioned before, the ones that have at least one axis of symmetry are desirable for use as pin-fin shapes. Reddy et al. in [103] have mentioned that the pin fin cross-section is adapted from symmetric NACA00XX series airfoil. Abdoli et al. in [95] have exploited a scaled-down version of NACA0060 symmetric airfoil. Also in [104] the authors have pointed out that a

fin shape resembling NACA00XX airfoils is used.
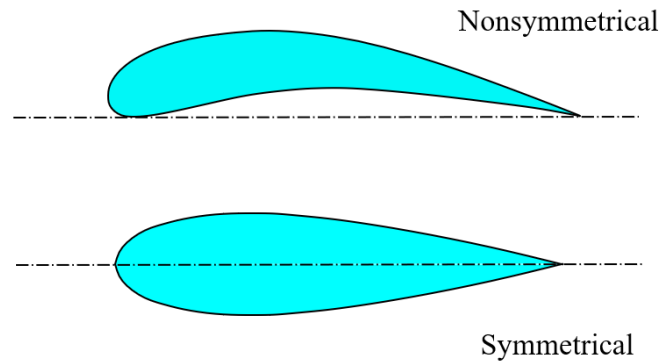
Figure 4.10: Different airfoil types (adapted from [45])

The terminology used for different fin geometries is rather inconsistent in the literature. In the study, [61] authors refer to the shape shown in the figure 4.11a as a "hydrofoil" shape. However, in another study ([105]) the authors refer to the shape shown in figure 4.11b as "hydrofoil." Other research studies also refer to to the same shape like the one shown in 4.11b as hydrofoil shape [106], [107]. There are other investigations in which the shape shown in 4.11c is called a hydrofoil-based geometry [59], [108].
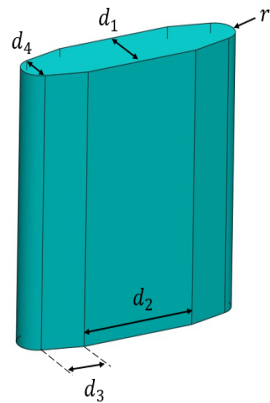
(a) Hydrofoil fin (adapted from [61])   (b) Hydrofoil pin-fin (adapted from [105])
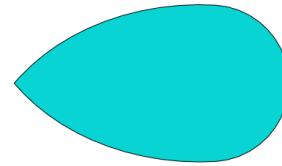
(c) Hydrofoil-based pin-fin (adapted from [59] and [108])

Figure 4.11: Different hydrofoil definitions

Symmetric Convex Fin

According to the definition, a symmetric convex lens is composed of the intersection of two intersecting circles with the same radius. The definition comes from the application of such lenses in optics. The symmetric lens is defined so that the light arrays that come from either side of the lens parallel to the lens's major axis cross one another at a single point on the opposite side of the lens [109]. Such lenses can be fully identified using two geometric parameters, the chord length shown as l and the thickness shown as t in figure 4.12.

Abdoli et al. in [95] have proposed a symmetric lens cross-section for a micro pin

fin array to cool down high heat flux electronic chips. Later other researchers have exploited the same cross-section shape for pin fin arrays [103]. Reddy et al. have done a multi-objective optimization on the symmetric convex micro pin fins. The optimization assumes a fixed distancing between the fins in the pin fin array and considers the inlet speed, pin fin height, pin fin thickness, and chord length [104]. Yang et al. have used a sine-shaped pin-fin for a micro channel heatsink. However, not enough description is provided as to how this sine shape pin-fin is defined. Based on the fin appearance, this fin is quite similar to the convex symmetric fin [105].
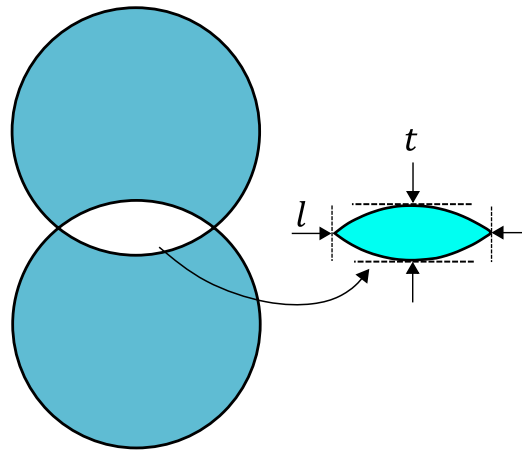
Figure 4.12: Symmetric convex lens cross section

Offset Strip Geometry

Conventional offset strip fins (OSF) are widely used in heat exchangers. They are very favorable in heat exchanging applications due to their superior geometry characteristics. This type of fin consists of a rectangular cross-section cut into strips of a certain length and displaced by half of the spanwise pitch of the fin. Figure 4.13 shows an instance of this fin's geometry [110]. Offset strip pin fin (OSPF) geometry

79

is different from what we used to observe for various pin fin shapes because it is not an independent fin shape but rather a specific layout of rectangular fins in a fin array. Originally offset strip fin (OSF) geometry has not been part of the pin-fin geometry category since the offset strip fins are folded fins that are being added to the heat source surface as an extension to increase the surface area [111]. This is more specifically shown in figure 4.13b. Pin-fin geometries, on the other hand, are integrated into the base section which is in contact with the heat source so there is no extra object such as sheet or folded fin. However, themal designers have been inspired by the folded fin offset strip geometry's layout to come up with a rectangular staggerred pin-fin array that has similar chracteristics to that of the folded fin offset strip design. Figure 4.14a shows the pin-fin version of the offset strip geometry [112]. The folded fin offset strip and pin-fin offset strip geometry difference is that the folded fin can be a double-sided surface extension whereas the pin-fin version is single-sided.

Researchers have referred to the new version of offset strip pin-fin (OSPF) layout as "offset strip fin (OSF)" [113], [114], [115], [116], [117]. However this name convention does not fully reflect that the pin-fin version of offset strip layout (OSPF) is rather different from the original historical version (OSF).

It is apparent that rounding the sharp edges of the rectangular fin will decrease the drag force caused by the fin shape as opposed to keeping the sharp edges. Thus, a modified version of offset strip pin-fin shape with rounded edges will most likely be a more promising design candidate [112]. This pin-fin geometry is illustrated in figure 4.14b.

(a) Isometric view of a folded fin OSF geometry

(b) Front view of folded fin OSF geometry
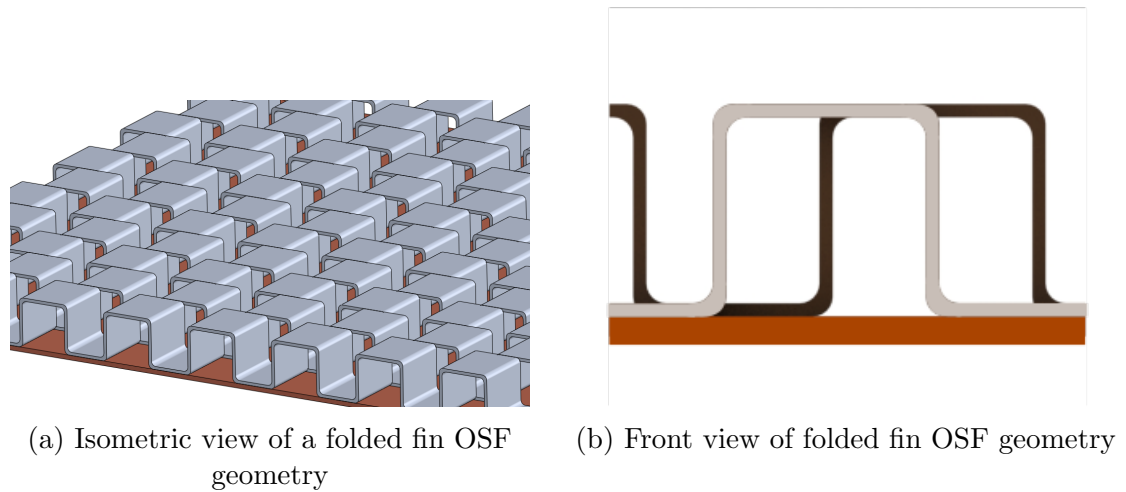
Figure 4.13: OSF geometry

(a) Conventional OSPF geometry with sharp edges

(b) Modified OSPF with rounded edges
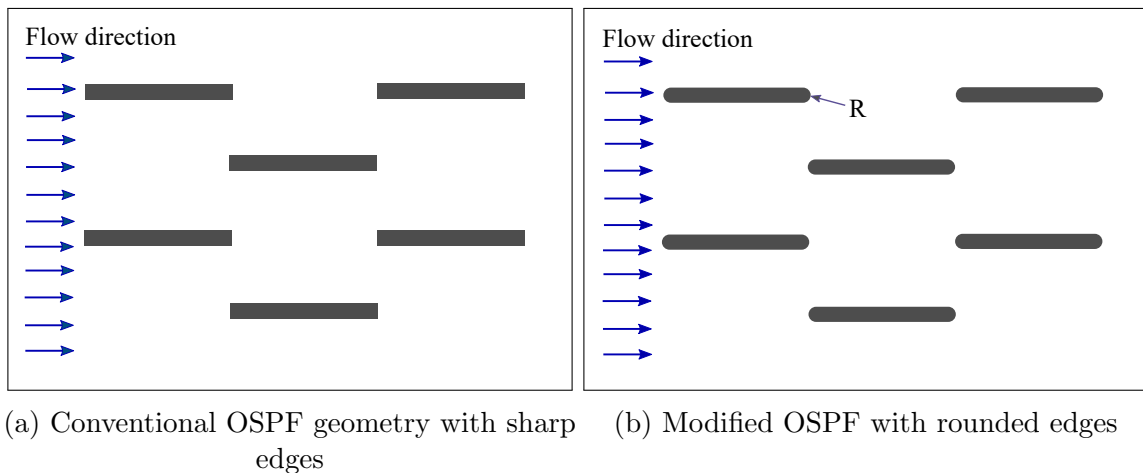
Figure 4.14: OSPF geometry

4.3.2 Selection of Pin-fin Shapes

This section aims to select a few of the above-mentioned pin-fin geometries for the purpose of the pin-fin comparative analysis case study. As different pin-fin geometry

configurations are numerous, it is practically impossible to consider all of the different geometries. Therefore the case study shall be confined to a few selected geometries. However, the methodology that has been used in this case study is applicable to other geometries as well.

Due to the reasons mentioned in the section 4.3.1 under circular fins, this pin-fin configuration will be the main design candidate, which will be treated as a baseline design.

It seems that the extruded-type cone fin is arbitrarily defined and does not have a specific geometrical correlation to the actual mathematical cone. Considering the mentioned fact, one could conclude that the cone-shaped fin can also be defined in another way. In other words, if we modify the cone shaped fin so that the straight lines will be tangent to the circle, the resulting geometry will be the exact same geometry as the drop-shaped pin-fin. The smooth transition from the circle to the straight line on the drop-shaped fins implies the fact that the flow separation could potentially happen later on the surface as opposed to the cone fin. This superiority of the drop-shaped fin made us exclude the cone-shaped fin from this investigation. Hydrofoil/airfoil fins are another choice. These fins, especially the NACA00XX airfoil series, are well-established and have been thoroughly investigated in the literature. However, due to the fact that the most common shape of hydrofoil/airfoil is quite similar to the drop-shaped fin, we will not investigate this geometry in this project. It is expected that the curved profile of hydrofoil fins will be more expensive to manufacture and most likely will not introduce much gain compared to the drop-shaped fin.

Symmetric convex geometry is a promising shape due to the fact that it only

consists of circular curves. This feature makes machining easy since circular inter-polation schemes are already realized in different manufacturing techniques. There are not many researchers who have analyzed this fin shape and compared it to other pin-fin geometry. Therefore this fin configuration will be included in our study.

Offset strip pin-fin (OSPF) configuration is also another interesting option. In fact, many off-the-shelf cooling systems in automotive applications take advantage of such fin configuration due to ease of manufacturing. It provides a high surface to volume ratio due to its high aspect ratio nature, which will enhance heat transfer. At the same time, the high aspect ratio results in a streamlined shape which delays separation and reduces the pressure drop. Considering all the mentioned rationals, this geometry type is included in our analysis. As discussed before, the OSPF geometry with rounded edges will most likely outperform the conventional version with sharp edges; thus, the modified version will be utilized. Figure 4.15 illustrates different design candidates that will be analyzed and compared in the current study.
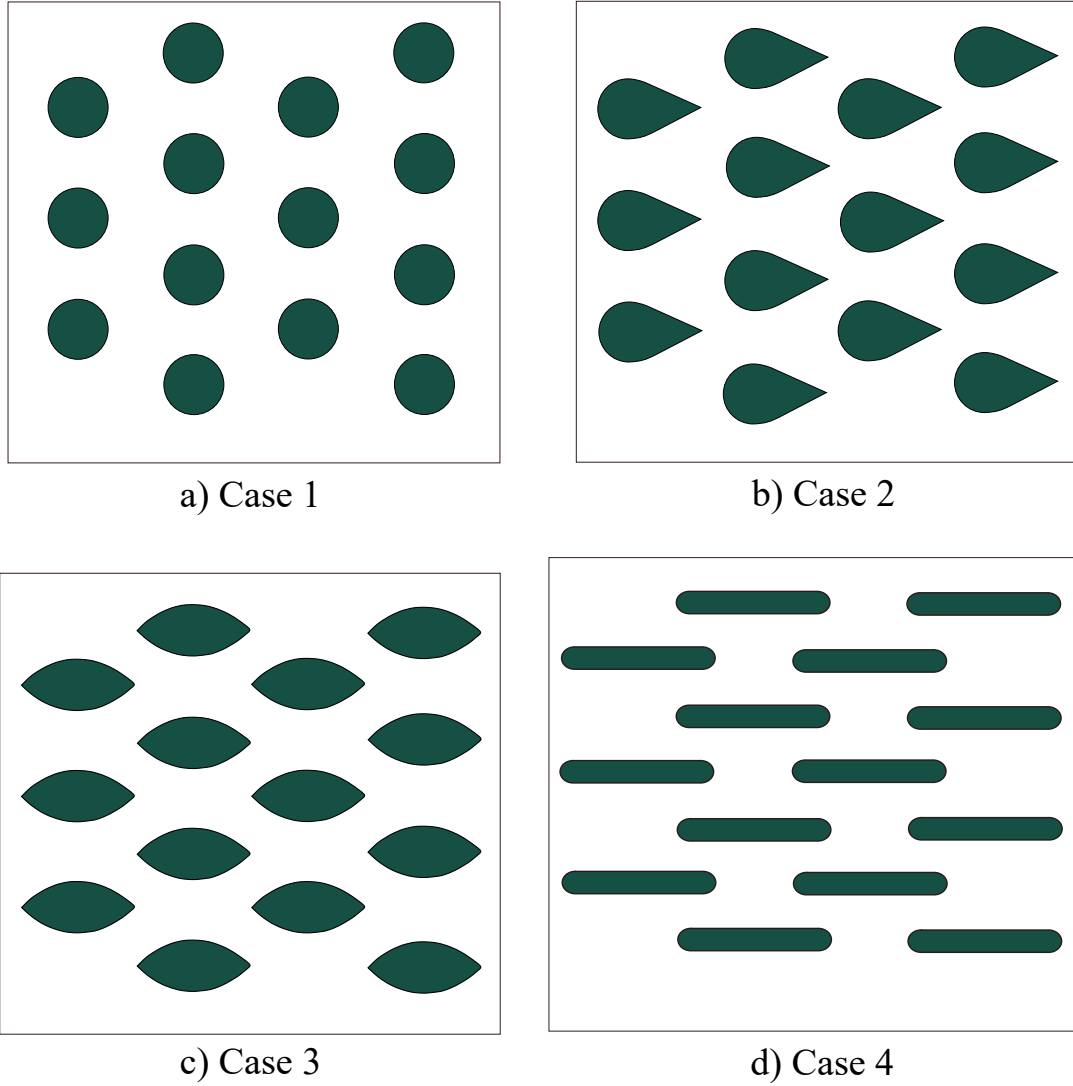
Figure 4.15: **a)Case 1**: circular pin-fins   **b)Case 2**: drop-shaped pin-fins
c)Case 3: symmetric convex lens pin-fins   **d)Case 4**: offset strip pin-fins

4.4   Methodology

The idea of this study is to investigate different pin-fin shapes in the same fin array configuration. The objective here is to isolate the effect of fin geometry on the performance of the heat sink. As it is the case with most of the real-world engineering problems, our problem is a multi-variable problem in which the fin shape is only one aspect of the pin-fin design. As mentioned earlier, the pin-fin array configuration is of paramount importance in the performance of the heatsink. Thus, in this study it has been decided to keep the array configuration the same in all of the design candidates. Considering the definition of the pin-fin density, one can conclude that the abovementioned assumption means that the total number of fins in a certain area is going to be identical in different pin-fin design candidates.

To ensure that the design comparison will be done in a proper manner, a set of constraints shall be imposed on the variables that are of no interest for the comparative analysis. The parameters that are of interest in this study are as follows:

- The shape of the geometry since the aim of the study is to investigate the effect of pin-fin shape in a pre-defined fin layout.

- The hydraulic diameter of the pin-fins to control the length-scale of the design.

- The overall heat transfer coefficient on the fluid/solid interface.

- The total pressure drop of the cooling system.

As with other design challenges, the variables and constraints should be handled carefully so that the problem does not end up being under-constrained or over-constrained. In order to ensure that the system is fully constrained, a basic mathematical calculation will be provided here. The following assumptions are made:

- The total surface area of the fluid/solid interface is assumed to be the same for all the design candidates.

- As mentioned earlier, the layout of the pin-fin array is assumed to be fixed. Therefore, the pin-fin density will be constant. This presumption results in the fact that the number of fins located in a certain area of the baseplate will be the same for any of the design candidates.

- The height of the pins is assumed to be the same for all of the design candidates.

- The hydraulic diameter of the pin-fins is assumed to be the same for two different designs.
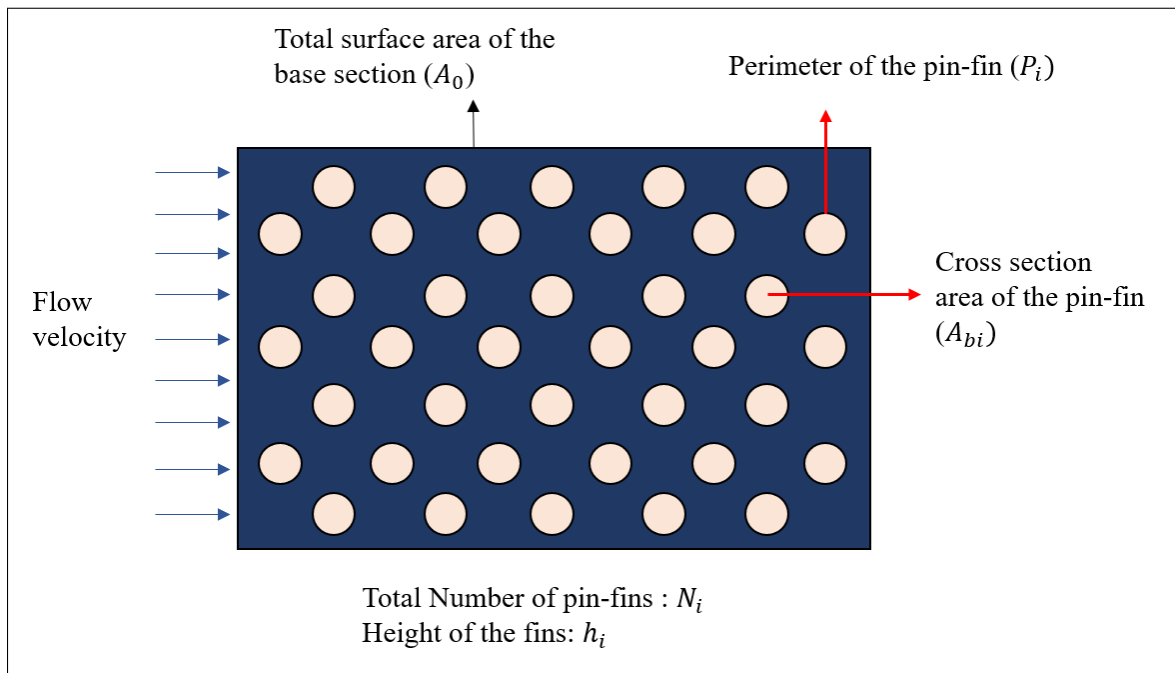
Figure 4.16: A representative pin-fin configuration
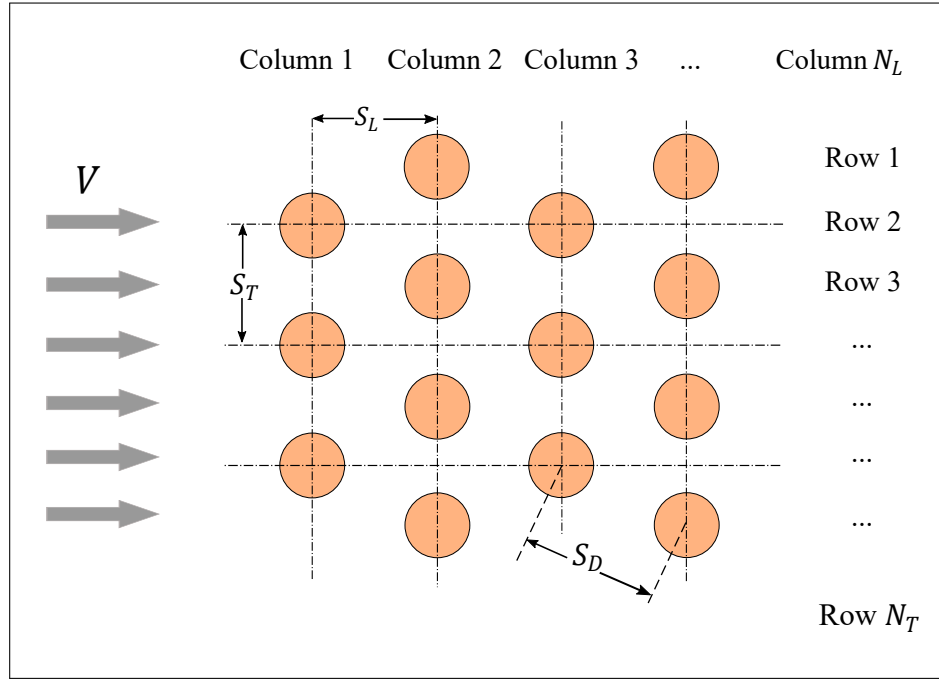
Figure 4.17: Staggered pin-fin array

The purpose of this mathematical analysis is to identify whether the abovementioned constraints will make the problem fully constrained, under-constrained, or over-constrained. The name convention of the following equations is demonstrated in 4.16. The mentioned constraints will result in four equations, respectively.

$$A_0 - N_i A_{bi} + N_i(h_i P_i) = A_0 - N_j A_{bj} + N_j(H_j P_j) \qquad (4.4.1a)$$

$$N_i = N_j \qquad (4.4.1b)$$

$$H_i = H_j = H \qquad (4.4.1c)$$

$$D_{hi} = D_{hj} = \frac{4A_{bi}}{P_i} = \frac{4A_{bj}}{P_j} \qquad (4.4.1d)$$

Equation 4.4.1b and 4.4.1c will be substituted in equation 4.4.1a. The result will

be as follows:

$$HP_i - A_{bi} = HP_j - A_{bj} \tag{4.4.2}$$

If we divide equation 4.4.2 by the non-zero $P_i P_j / 4$ term, the following relation will be obtained:

$$\frac{4H - \dfrac{4A_{bi}}{P_i}}{P_j} = \frac{4H - \dfrac{4A_{bj}}{P_j}}{P_i} \tag{4.4.3}$$

Now it can be seen that the numerator of equation 4.4.3 is a linear combination of equations 4.4.1a to 4.4.1a. As a result, the equation will have an apparent solution of $P_i = Pj$. Considering the hydraulic diameter constraint, the apparent solution of the set of equations results in an identical fin shape (since the perimeter of the fins, as well as the cross-section of the fins, should be the same). Apparently, the problem is over-constrained in this case due to the dependency of the fourth constraint on the other three equations. Therefore, the extra constraint that is being imposed on the system should be eliminated. To do so, one should go back to the underlying reasons behind each assumption and why that particular assumption is in place.

The first and foremost assumption for equality of total surface area in different designs is considered for the fact that the total surface area directly affects the amount of heat transfer at the fluid/solid interface.In fact, if we rule out this assumption, once the comparison of the fin geometries is done, we should compare the performance metrics of each fin against the difference between the total surface area in that particular geometry as opposed to the total surface area of the baseline geometry.

The second assumption is in place in order to make sure that we rule out the effect of fin layout and distancing of the fins from our study. This can not be compromised

for the fact that changing the fin layout, such as switching to inline pin-fin configuration instead of staggered configuration, can significantly change the thermal-hydraulic performance. If the fin layout was changed, one would not be able to distinguish between the effect of layout change and geometry change. Additionally, changing the layout of the fins from one design to the other will change the manufacturability constraint. The primary objective of this project is to ensure that the comparative analysis is done in a way that the design candidates not only are manufacturable but also the manufacturing cost is quite comparable across all of the design candidates. Therefore this constraint can not be touched.

The third constraint is imposed on the height of the fin. The height of the fin specifies the height of the cooling jacket. Ideally, the designer wants to have the cooling jacket height be the same as the height of the fins to avoid bypassing the flow under the fin. The bypass flow does not contribute to the heat transfer; thus, it is of no use to the system performance and comes with the cost of larger heat sinks.

The fourth constraint is the hydraulic diameter constraint, where the characteristic length of the fin is defined as the ratio of the cross-section area of the fin to the wetter perimeter of the fin. Then a multiplying factor of four is introduced to the definition so that the hydraulic diameter of a cylinder can be tied down to the diameter of the cylinder. This characteristic length essentially acts as a length scale of the pin-fin. The designer wants to ensure that the fins with the same length scale or at least length scales within a certain range are compared to each other. For instance, it is not desired to compare a pin-fin with a length scale of 10 μm to a pin fin with a length scale of 1 mm.

As mentioned before, we want to see the effect of fin shape on the heat transfer

coefficient to be isolated from other factors so that we can have a fair comparison between different design candidates. The first and the fourth constraint are the ones that can be reconsidered to either stay in the set of constraints or be removed. The result of the preliminary analysis of this study showed that either one of these constraints could be kept, and the other parameter will stay close enough to and within a certain range of the baseline design. According to the fact that the amount of heat that is being convected away from the heat source is proportional to the total surface area of the fluid/solid interface, this area will not be constrained so that we can see the effect of each shape on both the heat transfer coefficient and surface area. The effect of hydraulic diameter, on the other hand, is more obscure in the heat transfer relations; therefore, it was more sensible to keep the length scale constant.

Table 4.4 summarizes the parameters that are kept the same in the current comparative analysis. Table 4.5 shows the shape parameters of each design candidate. These parameters are selected such that the hydraulic (2.2mm) diameter stays the same for all the design cases. It is noteworthy that the set of shape parameters is not identical, and different sets of parameters can be obtained to satisfy the hydraulic diameter constraint. However, the variables are picked in a way that the variation of fin aspect ratio in comparison to the baseline case (circular) is minimized. The resultant mass and wetted surface area of each design case are presented in 4.6.

The way that the constraints and design variables are handled throughout this analysis is distinctive in the sense that the constraints are being very carefully accounted for. There was no such approach found in the literature that treats the design variables and constraints in a way in which the effect of the shape is isolated from other factors in a multi-variable design of experiment (DOE).

Table 4.4: Constant parameters of comparative analysis

Design case	$D_h(mm)$	$S_T(mm)$	$S_L(mm)$	N_T	N_L
case 1 (baseline circular)					
case 2 (drop-shaped)	2.2	4.2	3.6	28	38
case 3 (symmetric convex)					
case 4 (offset strip with rounded edges)					

Table 4.5: Shape parameters of the different pin-fin design cases
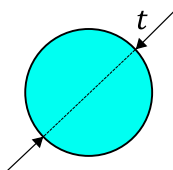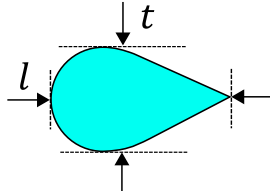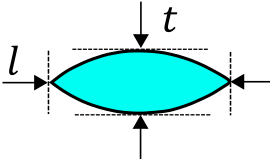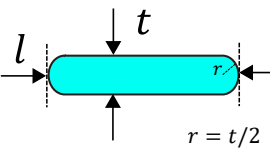
design case	shape geometry	shape parameters (mm)	fin height (mm)
case 1		$t = 2.2$	
case 2		$t = 2.2$ $l = 4.1$	6
case 3		$t = 1.8$ $l = 4$	
case 4		$t = 1.3$ $l = 4.6$	

91

Table 4.6: Comparison of design cases in terms of wetted surface area and mass

Design case	Total wetted area of the baseplate (cm^2)	percentage of surface area extension relative to the baseline (%)	Total mass of the baseplate (g)	percentage of mass increase relative to the baseline (%)
case 1	286.3	0	484.6	0
case 2	371.9	29.9	531	9.6
case 3	347.9	21.5	518.6	7.0
case 4	471.1	64.5	584.9	20.7

4.5 Computational Fluid Dynamics (CFD) Simulations

Computational Fluid Dynamics (CFD) simulation is used to analyze the design candidates as outlined in figure 4.15 and compare them in terms of the performance metrics mentioned in 2.2. ANSYS Fluent™ software is used for the CFD simulations.

4.5.1 CAD Model

In this section, an overview of the CAD model of the representative power module will be presented along with the 3D model of the cooling jacket, which is used to cool down the baseplate of the module. Additionally, the assumptions which are used to simplify the geometry will be pointed out.

The cooling jacket (shown in figure 4.18a) is designed based on the reference design available in the power module's application note [118]. Figure 4.18b shows a cross-section of the cooling system to illustrate the cooling jacket channel configuration as well as different components of the cooling system. As previously discussed, direct cooling of the baseplate is being employed for cooling of the current power electronic

module. Therefore no TIM is used. Since the baseplate is directly in contact with the cooling fluid, we shall ensure that the cooling jacket is properly sealed since any leakage can cause a catastrophic failure. For this reason, an o-ring that seats between the baseplate and cooling jacket top surface will be used to perfectly contain the coolant within the jacket. Having unnecessary small edges or faces will decrease the mesh quality and, therefore, the accuracy of the CFD calculation. Additionally, it will significantly increase the CPU time. Therefore the geometry should be cleaned simplified first. For this reason, all of the bolt holes of the baseplate are removed, and the fillets are eliminated. This simplified geometry is shown in figure 4.19a. Then the cooling jacket inlet and outlet faces are used to extract a watertight fluid volume geometry as shown in blue in figure 4.19b.
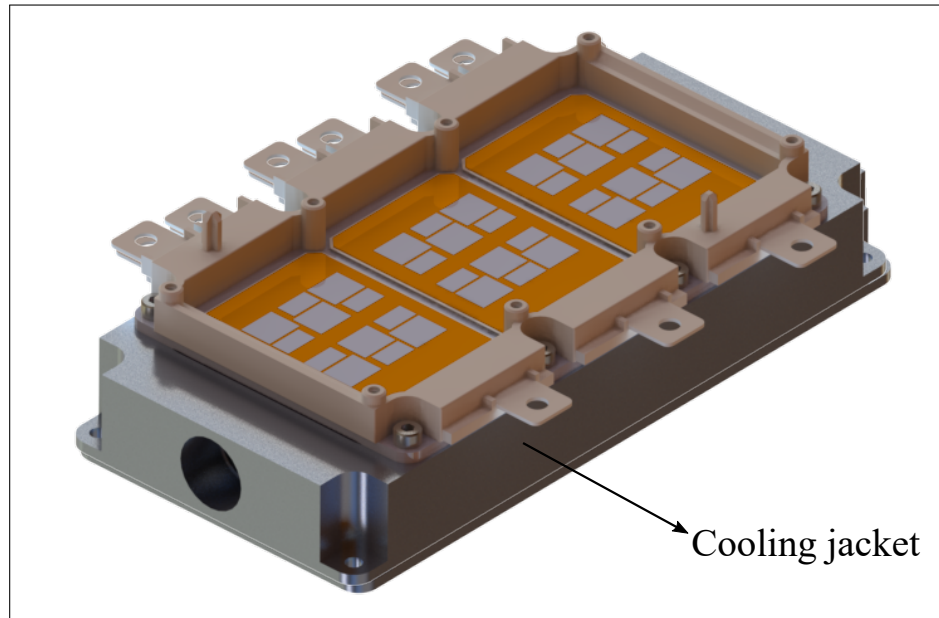
(a) Power module and cooling jacket assembly
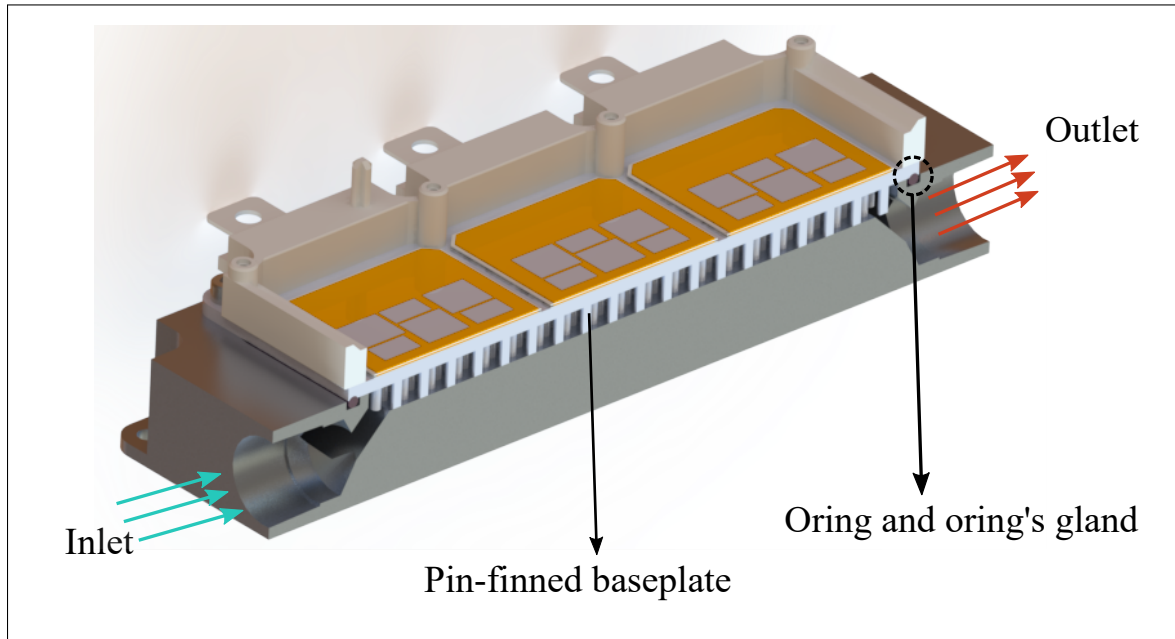
(b) Cross section of the power module and heatsink assembly

Figure 4.18: Power module and cooling jacket assembly and its corresponding components

(a) Simplified CAD model of the power module and cooling jacket

(b) Extracting a watertight fluid volume geometry
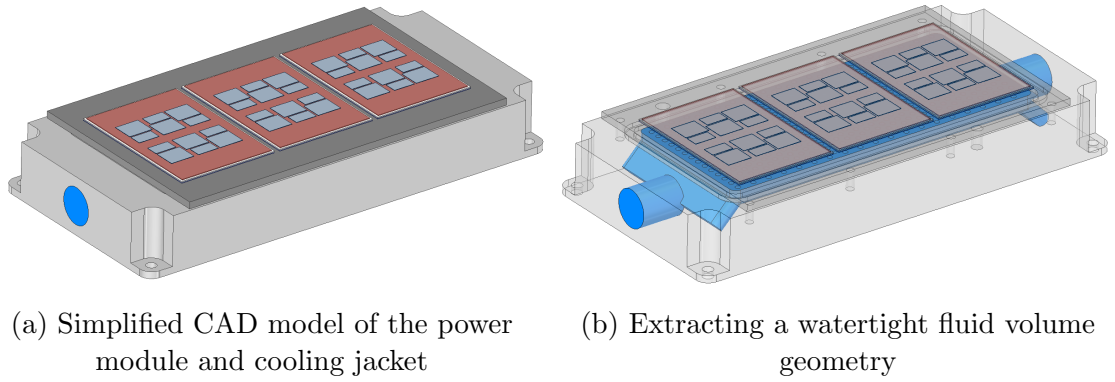
Figure 4.19: CAD model and fluid volume extraction

(a) case 1

(b) case 2

(c) case 3

(d) case 4
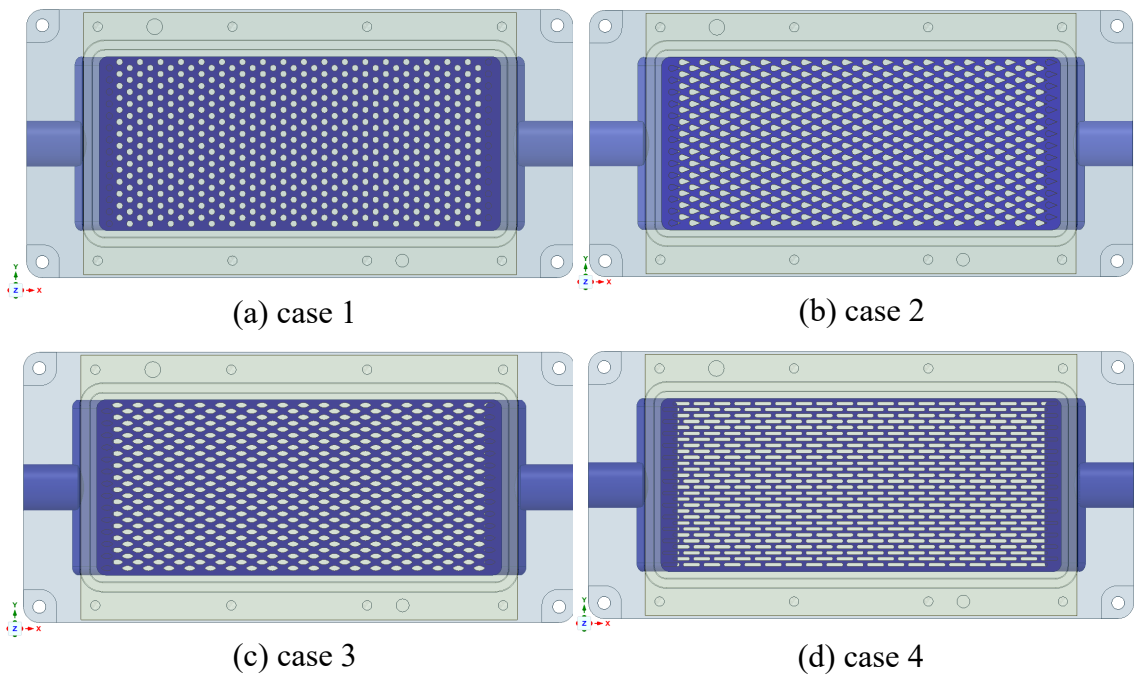
Figure 4.20: Different cases of pin-finned baseplate design

4.5.2   Theory

The heatsink analysis problem, in general, is a conjugate heat transfer problem meaning that both solid and liquid domains are available and they are interactively exchanging the heat. The heat conduction happening in the solid domain causes the heat to be conducted away from the heat sources (chips). Then the liquid convects the heat away from the solid domain using convective heat transfer. Convective heat transfer is a combination of diffusion and conduction that happens within the fluid domain.

The liquid considered as the cooling agent is the automotive coolant which is widely used and is a mixture of water and antifreze liquid (Ethylene Glycol) with standard volumetric mixture of 50%. It is also known as water ethylene glycol 50% or WEG50/50. This liquid is assumed to be incompressible.

Continuity Equation

The general form of continuity equation (also known as mass conservation) is shown in 4.5.1a.

$$\frac{\partial \rho}{\partial t} + \vec{\nabla}.(\rho \vec{V}) = 0 \tag{4.5.1a}$$

$$\frac{\partial \rho}{\partial t} + (\vec{\nabla}\rho).\vec{V} + \rho\vec{\nabla}.\vec{V} = 0 \tag{4.5.1b}$$

In the case of the compressible flow, we will have :

$$\frac{D\rho}{Dt} = \frac{\partial \rho}{\partial t} + (\vec{\nabla}\rho).\vec{V} = 0 \tag{4.5.2a}$$

$$\frac{\partial \rho}{\partial t} = -(\vec{\nabla}\rho).\vec{V} \tag{4.5.2b}$$

If we substitute 4.5.2b in 4.5.1a, it will result in:

$$\vec{\nabla}.\vec{V} = 0 \tag{4.5.3}$$

It is noteworthy to mention that there is a fundamental difference between incompressible flow assumption and incompressible fluid assumption. The mass conservation is derived for a control volume of an infinitesimal size that moves along the flow velocity. Then the total derivative of the density will turn into the material derivative. Since we want the total derivative of density to be zero in the control volume in a compressible flow, we set $\frac{D\rho}{Dt} = 0$. Apparently, this approach maintains generality since the partial derivative of the density with respect to time can still be nonzero. ($\frac{\partial \rho}{\partial t} \neq 0$). This illustrates that compressible fluids can still undergo incompressible flow. Therefore one can conclude that incompressible fluids will definitely undergo incompressible flows, whereas incompressible flows are not generally associated with incompressible fluids. Additionally, the continuity equation shown in 4.5.3 is true for both steady-state and transient incompressible flow as there is no such assumption incorporated when deriving the continuity equation [45], [119].

Momentum Equation

Another set of equations for solving a fluid flow is momentum equations. Momentum equations in a three-dimensional space result in the govering equations of motion for fluid flow. The general differential equations of motion in vector notation are as follows:

$$\rho \frac{d\vec{V}}{dt} = \vec{\nabla}.\underline{\sigma} + \rho \vec{f} \tag{4.5.4}$$

$\vec{f}$ is the body force per unit mass which is acting on the fluid (for instance, gravitational force) and, $\underline{\sigma}$ is the stress tensor.

According to Newton's law, stress tensor for an incompressible Newtonian fluid is:

$$\underline{\sigma} = -p\underline{E} + 2\mu\underline{S} \tag{4.5.5}$$

Where $\underline{E}$ is the divergence of product of density and velocity ($\vec{\nabla}.\rho\vec{V}$) and $\underline{S}$ is the rate of strain tensor:

$$\underline{S} = \frac{1}{2}(\vec{\nabla}\vec{V} + \vec{\nabla}\vec{V}^T) \tag{4.5.6}$$

Considering the continuity constraint ($\vec{\nabla}.\vec{V} = 0$) and by substituting the divergence of the stress tensor in the equation of motion, for $\mu \neq const$ we will have:

$$\rho\frac{d\vec{V}}{dt} = -\vec{\nabla}p + \mu\Delta\vec{V} + \vec{\nabla}\mu.2\underline{S} + \rho\vec{f} \tag{4.5.7}$$

Equation 4.5.2 is called the Navier-Stockes equation in honor of the mathematicians who came up with the formulation [45], [119].

Energy Equation

The energy equation is the last equation that must be solved in the conjugate heat transfer problem. The general differential form of energy equation for the fluid region in the absence of species diffusive terms is as follows:

$$\frac{\partial(\rho E)}{\partial t} + \vec{\nabla}.(\vec{V}(\rho E + p)) = \vec{\nabla}.(k_{eff}\vec{\nabla}T) + \vec{\nabla}.(\underline{\sigma}_{eff}.\vec{V}) + S_h \tag{4.5.8}$$

Where k_{eff} is the effective thermal conductivity (summation of molecular conductivity (k) and turbulent thermal conductivity(k_t)). σ_{eff} is the effective stress tensor. S_h is the volumetric heat source within the domain. E is the total energy as defined below:

$$E = h - \frac{p}{\rho} + \frac{V^2}{2} \tag{4.5.9}$$

h is the sensible enthalpy and for incompressible flows it is defined as:

$$h = \sum_j Y_j h_j + \frac{p}{\rho} \tag{4.5.10}$$

Y_j is the mass fraction of species j and:

$$h_j = \int_{T_{ref}}^{T} c_{p,j} dT \tag{4.5.11}$$

The first term on the right side of the equation 4.5.2 represents energy transfer due to conduction. The second term on the right-hand side represents viscous dissipation (work done by viscous forces).

In the solid domain, the energy transport equation is as follows:

$$\frac{\partial(\rho h)}{\partial t} + \vec{\nabla}.(\vec{V}\rho h) = \vec{\nabla}.(k\vec{\nabla}T) + S_h \tag{4.5.12}$$

h in the first term on the left-hand side of the equation 4.5.2 is the sensible enthalpy of the solid ($\int_{T_{ref}}^{T} c_p dT$). The second term on the left-hand side is the convective energy transfer due to the motion of the solid. Since, in our case, the solid region is static, this term is going to be zero. The first term on the right-hand side represents the divergence of the conduction heat flux ($-\vec{\nabla}.\vec{q}$) within the solid domain. The

conductive flux is obtained from the Fourier's law of conduction ($\vec{q} = -k\vec{\nabla}T$) where k is the thermal conductivity of the solid. The second term on the right-hand side of the equation is the volumetric heat source [120].

Fluid Flow Assumptions and Summary of Equations

The following assumptions are made to simplify the analysis:

- The flow is single-phase and the liquid is incompressible.

- The flow has reached steady-state condition.

- Natural convection and radiation to the surrounding environment is neglected. This is a realistic assumption due to the fact that the heat transfer rate of forced convection liquid-cooling is much higher than the heat transfer rate due to natural convection or radiation from the side walls.

- The gravitational forces and buoyancy effects are negligible compared to inertial forces and viscous forces of the forced convection.

- Viscous heating or the heat dissipation due to viscosity is assumed to be negligible.

By applying the abovementioned assumptions to the general form of continuity, momentum and, energy equations for the fluid region, these equations will boil down to

the following equations in cartesian coordinates [61], [121]:

$$\frac{\partial u_i}{\partial x_i} = 0 \tag{4.5.13a}$$

$$\frac{\partial(\rho u_i u_j)}{\partial x_j} = -\frac{\partial p}{\partial x_i} + \mu\frac{\partial^2 u_i}{\partial x_j^2} + \frac{\partial \mu}{\partial x_j}\left(\frac{\partial u_i}{\partial x_j} + \frac{\partial u_j}{\partial x_i}\right) \tag{4.5.13b}$$

$$\rho c_p\frac{\partial(T u_j)}{\partial x_j} = k_f\frac{\partial^2 T}{\partial x_j^2} + S_h \tag{4.5.13c}$$

For the solid region, the energy equation will be as follows:

$$k_s\frac{\partial^2 T}{\partial x_j^2} + S_h = 0 \tag{4.5.14}$$

4.5.3   Boundary Conditions

Temperature

The coolant temperature in automotive application is generally in the range of 65°C to 105°C [58], [122] . Nowadays, a dedicated cooling with a lower temperature than the engine cooling loop is being used to cool down electric motors and traction inverters [123], [124]. It is worth mentioning that due to the differences between the operating temperature of batteries, electric machines, and power converters, there is often a separate cooling circuit for battery cooling. Moreover, air conditioning systems have a separate loop for heating/cooling loads of the cabin [125]. The focus of discussion here is on the thermal management of the powertrain components. Therefore it is quite common to have two cooling circuits for powertrain cooling in EVs and three loops and for HEVs. However, there is a significant demand for the integration of

these cooling systems [125]. We can see engine cooling loops (primary loop) operating at temperatures around 105°C whereas the operating temperature for the motor drive cooling loop (secondary loop) is around 70°C. There is a general demand to push the secondary loop's operating temperature to higher temperatures so that it facilitates the integration of the motor drive to the engine. Another objective of doing so is to unify the cooling loops. This trend, however, imposes aggressive thermal requirements on both power electronic device manufacturers and cooling designers [126]. In this simulation, we have assumed that the power module will be used in an automotive cooling system that has a secondary cooling loop with low temperature.

Most power electronic modules can withstand temperatures as high as 150°C while electric machine insulations can tolerate up to 230°C [3]. Power converters are the most vulnerable components of the powertrain in terms of sensitivity to temperature variation and reliability issues associated with it [127], [128]. Thus power converters are usually the first components to be cooled when it comes to series cooling (e.g. Toyota Prius cooling loop). Therefore we are looking at temperatures around 65°C at the inlet of the power module. For the purpose of our simulation, a conservative inlet temperature of 75°C is assumed for the inlet of the module's cooling system. This assumption is made due to the fact that there is a trend toward using high-temperature cooling loops for power electronics. Therefore instead of assuming 65°C, which is the minimum value of the range, we have assumed a slightly higher inlet temperature.

Flow Rate

The coolant flow rate in automotive cooling loop applications is typically in the range of 1 to 14 liter per minute (LPM). Ning et al. in [128] have used 4 LPM and 8 LPM flow rates for analyzing two different cold plates for different power modules. Hamut et al. have regulated the flow rate of a water-based cooling circuit in the range of 1-10 kg/min, which is equivalent to 1-10 LPM [129]. In [130] different thermal management system configurations are investigated using an equivalent flow rate of 13.6 LPM for the WEG loop. Chinthavali et al. have developed a 10 kW automotive inverter using a novel metal 3D-printed power module with integrated cooling and have tested the cooling system at 1.5 gpm (5.7 lpm) [75]. Other studies have used flow rates in the same range as mentioned earlier. For instance, in [131] authors have used 2 and 5 LPM flow rates in their experiments. All in all, the range of 6-14 LPM flow rates are selected for the purpose of our CFD simulation. Each design candidate will be analyzed at five different flow rate levels (6, 8, 10, 12, and 14 LPM).

Fluid Properties and Heat Removal Capacity

The power loss of the chips is applied to the chip bodies in volumetric source terms. All of the circumferential walls of the system are considered adiabatic. Even though this assumption is not the case in a real-world situation, it is more conservative than the non-adiabatic wall situation. This is due to the fact that, in reality, the heat loss to the surrounding will further decrease the junction temperature. Considering the fact that the system is assumed to be adiabatic, the total power dissipated by the power module should be eventually absorbed by the fluid. If we write the total

energy balance at the system level, we will have:

$$P = \dot{m}C\Delta T \tag{4.5.15}$$

P is the total power absorbed by the fluid, and $\dot{m}$ is the mass flow rate. The term $\dot{m}C$ in equation 4.5.15 is called the heat removal capacity of the fluid. Considering the total power loss to be $P = 4482\ W$ and the coolant's specific heat to be $C = 3495\ J/kg.K$ (at 75°C) and the minimum flow rate of 6 LPM, the total temperature rise of the fluid from inlet to outlet will be calculated as follows:

$$\Delta T = \frac{P}{\dot{m}C} = \frac{4482\ W}{0.1\ kg/s \times 3495\ J/kg.K} = 12.8°\ C \tag{4.5.16}$$

The temperature rise for 8, 10, 12 and, 14 LPM flow rates will be 9.6°C, 7.6°C, 6.4°C and, 5.4°C respectively. The effect of this temperature difference on the fluid properties of interest is summarized in table 4.7. As it can be seen from the table, this much temperature variation will not cause significant variation in density, specific heat, and thermal conductivity since the relative variation is less than 1%. Hence, in our numerical simulations, the variation of these properties with temperature is considered negligible, and ρ, C_p and k are assumed constant. On the contrary, viscosity variation is more than 10% and can be as high as 20% at lower flow rates. Therefore, temperature-dependent viscosity is employed using piece-wise linear interpolation.

Regime of the Flow

From the fluid regime perspective, the inlet cross-section area is the minimum cross-section of the fluid domain. Hence, the highest velocity happens to be at the inlet section with a 16 mm diameter circle. Therefore, for determining the flow regime,

Table 4.7: Variation of WEG50/50 properties due to temperature variation from inlet to outlet

	flow rate (lpm)	6	8	10	12
% Variation relative to the inlet temperature (75°C)	ρ	-0.9	-0.7	-0.5	-0.4
	C_p	1.4	1.0	0.8	0.7
	k	0.9	0.7	0.6	0.6
	μ	-20.5	-16.1	-12.8	-10.8

the Reynolds number is evaluated at the inlet. Table 4.8 shows the Reynolds number at different flow rates at an inlet temperature of 75 °C. Based on the turbulent flow criteria for internal flows ($Re > 10000$) one can clearly conclude that the flow is almost exclusively turbulent at 8, 10, and 12 lpm flow rate. However, at 6 lpm flow rate, the flow is in the transitional region ($2300 < Re < 10000$) while being quite close to the turbulent end as opposed to the laminar region. Considering the fact that the downstream pin-fin structure itself will cause significant perturbation and mixing for the flow, this flow rate will be simulated using turbulent models. It is noteworthy that both laminar and turbulent flow structures can be seen in transitional flows with turbulent effects being dominant as the Reynolds number (Re) gets closer to 10000. Additionally, turbulent models are able to capture transitional flows with acceptable accuracy.

The prantdl number (ratio of momentum diffusivity to thermal diffusivity) which controls the ratio of thermal boundary layer thickness to hydraulic boundary layer thickness is shown in table 4.8. These values are calculated at mean fluid temperature. Since the values are in the range of 8.6-9.2 for the evaluated range, we can ensure that the thermal boundary layer is much thicker than the hydraulic boundary layer.

Table 4.8: Reynolds number at different inlet flow rates

Flow rate (lpm)	6	8	10	12	14
Re	7758	10345	12931	15517	18103
Pr	8.6	8.8	9	9.1	9.2

Thus, once we ensure that the near-wall mesh size is fine enough for capturing the hydraulic boundary layer (through y_+ value), it will perfectly capture the thermal boundary layer effects.

4.5.4   Turbulent Modeling

In general, there are three classes of turbulence models. The first category is statistical approaches such as Reynolds average Navier-Stockes (RANS) and Unsteady RANS (URANS). The second category is the Scale Resolving Simulations (SRS), where larger-scale eddies are resolved, and smaller scales are modeled. The third class is the Direct Numerical Simulation (DNS) where the full spectrum of turbulence scales are resolved, which is extremely costly due to computational burdens and is out of reach for most industrial and scientific applications. The main reason those turbulence models are used in the first place is that the CPU time in DNS computation grows with Re^3 and the computational cost becomes extremely high as Reynolds number gets higher. This is due to the fact that Navier-stockes equations are highly non-linear and highly coupled to each other. To this date even SRS approaches are still out of reach for most engineering applications due to wall clock time, human effort and, marginal gains in accuracy. Statistical approaches, on the other hand, such as RANS, are extremely efficient and affordable. In these methods, the flow velocity is decomposed into mean and fluctuating values. Conservation equations are then

derived for mean variables. Since average quantities have less variation in time and space, the computation becomes affordable.

After such decomposition, the additional momentum transport terms will appear that behave like additional stresses. These additional terms $(\rho\overline{u_i u_j})$, which are the consequence of information loss due to averaging, are called "Reynold stresses" and are unknown. The filtering process does not solve the problem since it introduces the same number of unknowns as the number of equations. The derivation of exact equations for Reynolds stresses is possible but will introduce triple velocity correlations that make the computation even harder. Therefore some empirical information is required to close the problem, which is referred to as "turbulence closure problem." Boussinesq's generalized eddy viscosity hypothesis correlated the shear stress to a turbulent viscosity (μ_t) and turbulent kinetic energy(k) as below:

$$\tau_{ij} = \mu_t \left(2S_{ij} - \frac{2}{3}\frac{\partial u_k}{\partial x_k}\delta_{ij} \right) - \frac{2}{3}\rho k\delta_{ij} \qquad (4.5.17)$$

Where $S_{ij} = \frac{1}{2}(\frac{\partial u_i}{\partial x_j} + \frac{\partial u_j}{\partial x_i})$ and δ_{ij} is the Kronecker delta.

Thus the turbulence closure problem boiled down to the challenge of coming up with empirical models for μ_t and k. Later Menter F.R. came up with some models, and by combining them with Boussinesq's concept, a two-equation semi-empirical turbulence model was developed. Another well-known two-equation turbulence model is the $k-\varepsilon$ model, which has its own advantages and disadvantages. $k-\varepsilon$ is stronger in predicting the outer boundary layer effects, whereas $k-\omega$ is more powerful in viscous sublayer and flow separation prediction. Menter Baseline (BSL) turbulence model blend $k-\varepsilon$ in the outer boundary layer and $k-\omega$ near boundary layer using a standard blending function. Later on, Menter suggested a modification to the baseline

model considering the fact that shear stress was not limited to the boundary layer. Therefore, SST (Shear Stress Transport) model was built upon the BSL model using a shear stress limiter term [132], [133]. Menter continiously worked on tuning the turbulence model constants and also suggested a production rate limiter. The latest result of his state-of-the-art model was published in 2003 and has been an industrial standard for two-equation turbulence modeling since then . The following equations are the governing equation of $k - \omega\ SST$ model [134], [135] :

$$\frac{\partial(\rho k)}{\partial t} + \frac{\partial\left(\rho u_j k\right)}{\partial x_j} = P - \beta^*\rho\omega k + \frac{\partial}{\partial x_j}\left[(\mu + \sigma_k\mu_t)\frac{\partial k}{\partial x_j}\right] \tag{4.5.18}$$

$$\begin{aligned}\frac{\partial(\rho\omega)}{\partial t} + \frac{\partial\left(\rho u_j\omega\right)}{\partial x_j} =& \frac{\gamma}{v_t}P - \beta\rho\omega^2 + \frac{\partial}{\partial x_j}\left[(\mu + \sigma_\omega\mu_t)\frac{\partial\omega}{\partial x_j}\right] \\ &+ 2\left(1 - F_1\right)\frac{\rho\sigma_{\omega 2}}{\omega}\frac{\partial k}{\partial x_j}\frac{\partial\omega}{\partial x_j}\end{aligned} \tag{4.5.19}$$

Where $v_t = \frac{\mu_t}{\rho}$ is the kinematic turbulent viscosity and $P = min(\tau_{ij}\frac{\partial u_i}{\partial x_j}, 10\beta^*\rho\omega k)$ is the production rate term.

Let ϕ_1 represent any constant associated with original $k - \varepsilon$ model $(\sigma_{k1}, \sigma_{\omega 1}, \beta_1, \gamma_1)$ and ϕ_2 represent any constant associated with transformed $k - \omega$ model $(\sigma_{k2}, \sigma_{\omega 2}, \beta_2, \gamma_2)$, the corresponding constant in the blended model will be:

$$\phi = F_1\phi_1 + (1 - F_1)\phi_2 \tag{4.5.20}$$

Where the blending function F_1 can be computed as below:

$$F_1 = \tanh\left(\text{arg}_1^4\right) \tag{4.5.21a}$$

$$\text{arg}_1 = \min\left[\max\left(\frac{\sqrt{k}}{\beta^*\omega d}, \frac{500\nu}{d^2\omega}\right), \frac{4\rho\sigma_{\omega2}k}{CD_{k\omega}d^2}\right] \tag{4.5.21b}$$

$$CD_{k\omega} = \max\left(2\rho\sigma_{\omega2}\frac{1}{\omega}\frac{\partial k}{\partial x_j}\frac{\partial \omega}{\partial x_j}, 10^{-10}\right) \tag{4.5.21c}$$

d is the distance to the nearest wall. Turbulent eddy viscosity can be computed from the following relations:

$$\mu_t = \frac{\rho a_1 k}{\max\left(a_1\omega, SF_2\right)} \tag{4.5.22a}$$

$$S = \sqrt{2S_{ij}S_{ij}} \tag{4.5.22b}$$

$$F_2 = \tanh\left(\text{arg}_2^4\right) \tag{4.5.22c}$$

$$\text{arg}_2 = \max\left(2\frac{\sqrt{k}}{\beta^*\omega d}, \frac{500\nu}{d^2\omega}\right) \tag{4.5.22d}$$

Model constants are summarized in table 4.9.

Table 4.9: Turbulent model's constants

model	constant			
$k - \varepsilon$	$\gamma_1 = 5/9$	$\beta_1 = 0.075$	$\sigma_{k1} = 0.85$	$\sigma_{\omega1} = 0.5$
$k - \omega$	$\gamma_2 = 0.44$	$\beta_2 = 0.0828$	$\sigma_{k2} = 1$	$\sigma_{\omega2} = 0.856$
SST	$\beta^* = 0.09$		$a_1 = 0.31$	

Chapter 5

Comparative Analysis of Different Pin Fin Configurations

In this chapter, first, the CFD settings, including grid topology, numerical aspects of the simulation, and solver settings, are discussed. Discretization error is investigated afterward, and a grid convergence study is carried out. The result of the CFD simulations for each design is presented next. For each design case, pressure and temperature contours will be plotted at the nominal flow rate of 10 lpm. A summary of output parameters of interest will be provided. Then two characteristic curves of the heatsinks (pressure vs. flow rate and thermal resistance vs. flow rate) are plotted for each case. In the benchmarking section, all four design cases will be compared in terms of the performance metrics discussed in 2.2 at different flow rates, and explanations will be provided on how design candidates are performing compared to one another. Then the potential underlying reasons for such performance will be discussed. In the simulation verification, it has been tried to find matching analytical or experimental data from the literature to verify the results of each case.

5.1   CFD Settings

5.1.1   Grid Topology and Numerical Errors

The power module substrate, the baseplate, and the fluid domain are meshed separately to obtain more flexibility in the meshing step. The conformal mesh is used for the power devices and substrate layers, meaning that these components have meshed as a single body. The nonconformal mesh is used at the interface between the substrate and baseplate and the interface between baseplate and fluid domain. Hexahedral elements are used for the power module domain, and the hex dominant method is employed for the baseplate. Tetrahedral elements are used for the fluid domain since the complexity of this domain does not allow for hexahedral or swept meshing. Inflation layers (near-wall mesh refinement) are applied to the fluid domain walls using initially 12 layers with a growth rate of 1.2. Smooth transition (transition ratio 0.272) is applied to smoothly blend the near-wall structured mesh with the unstructured tetrahedral mesh far from the walls. Hence, a hybrid grid is obtained for the fluid domain (shown in figure 5.1a, 5.1b and, 5.2).

In general, there are three types of errors associated with CFD simulations as opposed to experimental studies. First and foremost is the numerical error. The second source of error is the modeling error. For example, in this case, the two-equation k-ω SST model is solved instead of solving the Reynolds shear transport equations. The amount of information that is missing when using reduced order turbulent models as opposed to the actual governing equations will cause the modeling error. The third source of error is the systematic error. In general, there are some uncertainties associated with each experimental study, such as measurement errors.

Other sources of systematic uncertainty include but not limited to domain extent, operating condition, manufacturing, and in-service variance.

To be able to identify the modeling error and systematic error associated with the CFD calculations, one shall first ensure that the numerical error is eliminated. The numerical error can be categorized into three types of errors. First is the truncation (round-off error) that is associated with the machine precision and the number of digits right of the decimal point. To reduce such error, double-precision numerics are used for all of the calculations. The second source of numerical error is the incomplete iteration error or residual convergence error that is associated with the way the iterative matrix solvers work. To alleviate such error, normally, a convergence criterion is set so that the iterative solver will continue until such convergence criteria are met. In our study, convergence criteria for continuity, x-velocity, y-velocity, z-velocity, k and, ω residuals are set to 10^{-3}. The convergence criterion for energy residual is set to 10^{-6}. The last and the most important error is the discretization error. Discretization error is caused by the fact that the governing equations are being solved in a finite-sized grid instead of an infinitely fine mesh. The difference between the exact solution of a continuum value on an infinitely fine mesh and the converged solution on a finite-sized grid is called the discretization error. Mesh independency check ensures that the continuum value can be estimated with an acceptable error band on a reasonably fine mesh. That is why mesh independency check is an integral part of any CFD calculation. This will be discussed in depth in the section 5.2.

A body sizing of 0.2 mm is applied to the chip and the solder underneath the chips to better capture the temperature distribution on these small bodies. This ensures that the global mesh size does not create large elements on the chips. Such a fine

element size is not required for the substrate layers; therefore, no specific body sizing has been applied to the substrate. Hence, the global mesh size (maximum element size 1mm) controls the substrate layers' element size. As shown in the figure 5.1a, the automatic algorithm smoothly transitions from small cells on the chip to larger cells on the substrate. A body sizing of 0.5mm is applied to the baseplate to ensure that heat spreading effects are properly captured within that region. A body sizing is also applied to the fluid domain. This body sizing is the subject of the mesh convergence study discussed in the section 5.2. Based on the result from the section 5.2 a body sizing of 0.5mm is selected for the fluid domain for all the design cases.

Initially, 8 layers of boundary layer refinement were being used for the grid convergence study. However, during the study, it was noticed that the area-average y_+ value is the range of 2.5–1.9 from mesh1 to mesh5. Since ideally, we want to $y_+ < 1$ to properly capture boundary layer effects, we chose to use 12 layers of mesh refinement near the wall. Even though grid convergence study is done using 8 layers of refinement, each case's final run at each flow rate is done on grids that have 12 layers of refinement. Thus, a conservative error estimation is presented. In all cases, the computed average y_+ is less than one.

5.1.2   Solver Settings and Computation

The coupled scheme is used for velocity coupling. The second-order upwind scheme is used for momentum, energy and, turbulence quantities. The pressure discretization scheme is second order. Gradient calculation is based on Green-Gauss Node Based scheme.

The simulations has been run on a machine with 96.0 GB of RAM and 2 Intel(R)

Table 5.1: Wall clock time of the simulations

Simulation step	Meshing	Pre-processing /setup	CFD run	Post-processing	Total/case
Approximated time (hr)	2	2	8	3	15
Total time	$25 \times 15 = 375 \ hr$				

Xeon(R) CPU (E5-2440 @ 2.44 2.4GHz). The computation has been done in parallel mode using 16 nodes of logical processors.

On average, each simulation run time is approximately 7 hours. The mesh computation takes approximately 2 hours for each case, including the human effort. Pre-processing setup and post-processing of the result take approximately 2 hours and 3 hours, respectively, for each case. The total number of simulation cases is 25. Four design cases, with each one having five different runs at five different flow rates plus five runs for the grid convergence study, add up to 25 in total. Table 5.1 is the summary of the approximated wall clock time for running different cases of the comparative analysis.
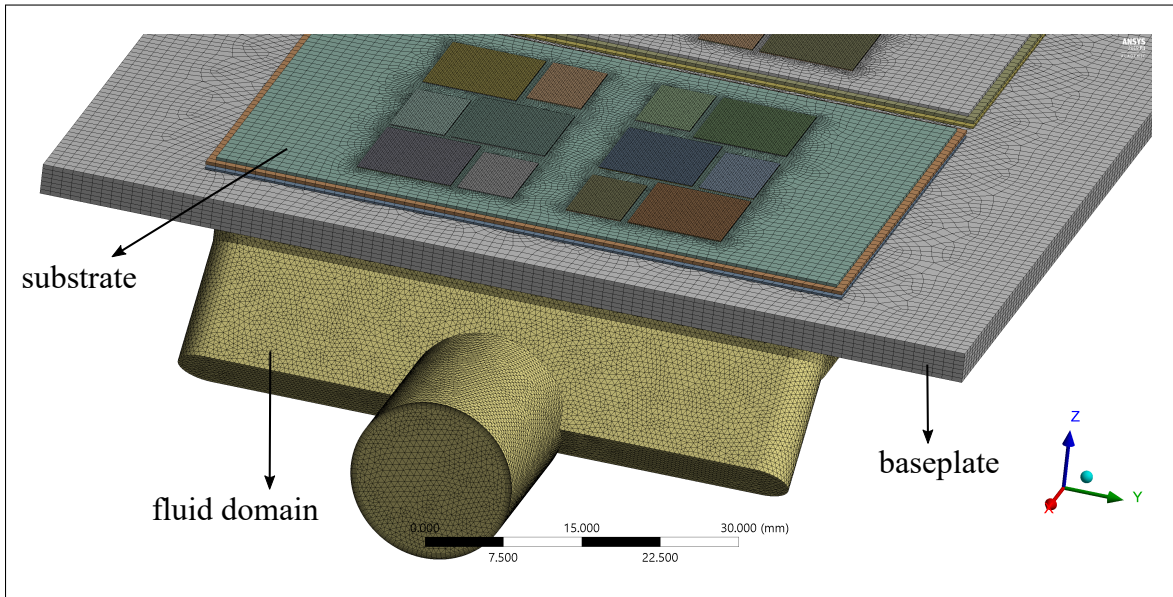
(a) Overview of the grid and different domains
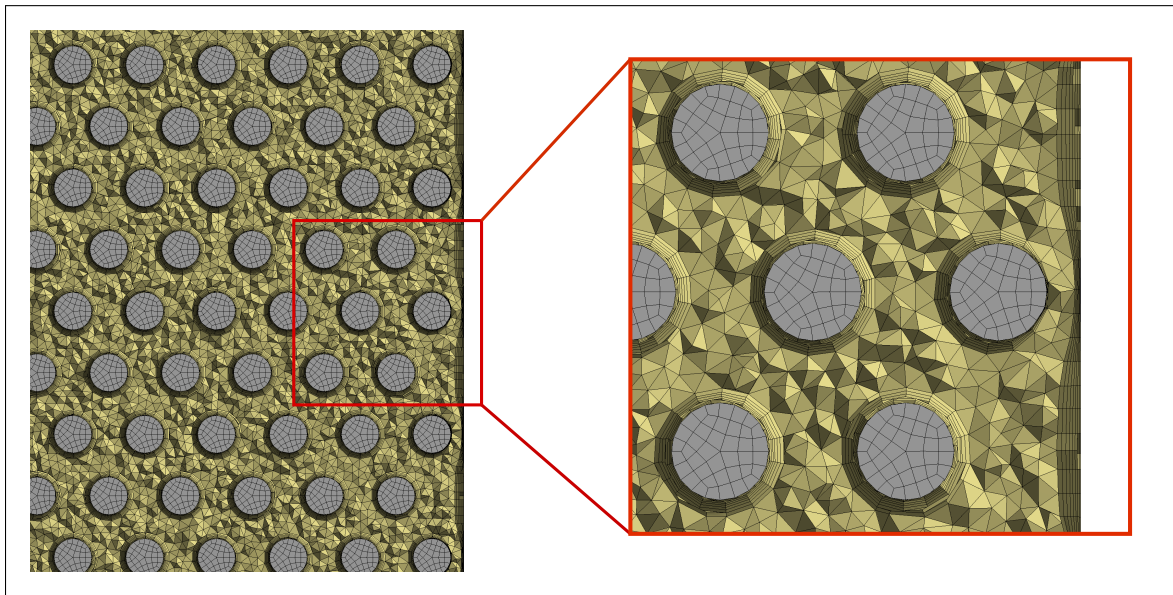
(b) Cross section of circular pin-fin design and its corresponding boundary layer mesh

Figure 5.1: Overview of the mesh
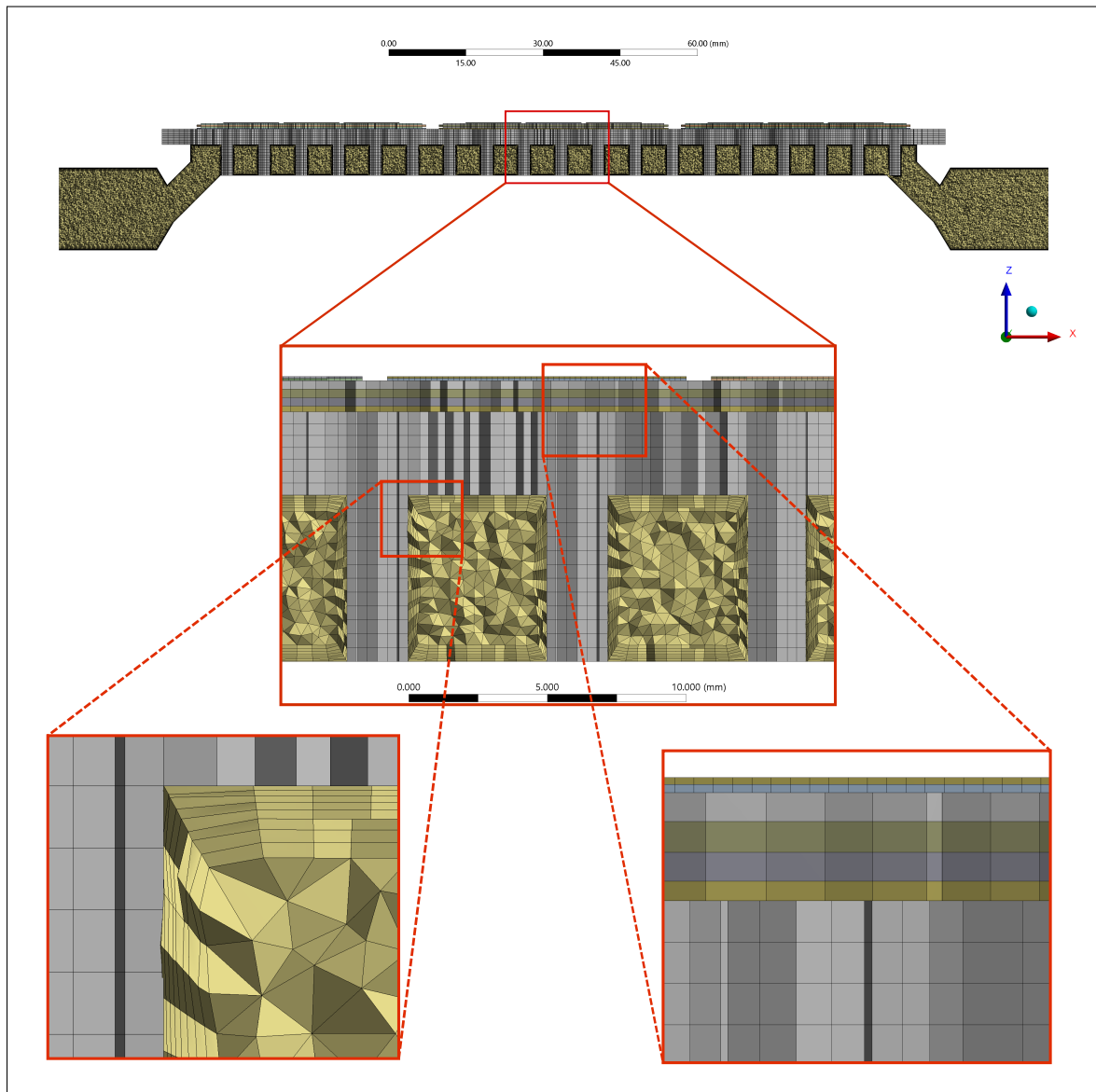
Figure 5.2: Cross section of circular pin-fin design and its corresponding boundary layer mesh

5.2   Discretization Error and Grid Convergence Study

Let f_1 be the solution of a parameter of interest on the fine grid and f_2 be the solution of the same parameter on the coarse grid. Normally the relative error (ϵ defined as below) is being reported in almost all of the grid convergence studies in CFD:

$$\epsilon = \frac{f_2 - f_1}{f_1} \tag{5.2.1}$$

In a uniform structured grid with a fine grid spacing of h_1 and coarse grid spacing of h_2 grid refinement ratio is defined as $r = \frac{h_2}{h_1}$. Based on the generalized theory of Richardson Extrapolation, the estimate of the exact solution (from fine and coarse grid solution) can be obtained as follows:

$$f[exact] \simeq f_1 + \frac{f_1 - f_2}{r^p - 1} \tag{5.2.2}$$

Where p is the order of discretization, which is equal to 2 for second-order schemes. In the case of using second-order schemes, Equation 5.2.2 has third-order accuracy. Grid refinement ratio requires commonality of the grid points on the coarse and fine grids; therefore, it is presumed that integer grid refinement is used.

A Grid Convergence Index (GCI) is developed based on the error estimator of the Richardson Extrapolation as below:

$$\text{GCI} = \frac{F_\text{s}|\epsilon|}{r^p - 1} \tag{5.2.3}$$

Where F_s is the safety factor of error estimation, which is normally in the range of 1–3. A safety factor of 1.25 is adopted in the current study based on [117]. Grid

refinement factor (r) in unstructured grids is commonly reported in terms of the total number of elements used in the coarse grid (N_2) and fine grid (N_1):

$$r = (\frac{N_1}{N_2})^{1/D} \qquad (5.2.4)$$

Where D is the dimensionality of the problem, which is equal to 3 in 3D problems.

Roache argues that although Grid Converge Index does not have the firm basis of a structured grid refinement, it is still preferable to simply reporting ϵ [136]. The error band will be computed as defined below [117]:

$$\text{Error band } = f_{\text{exact}} \pm f_{\text{exact}} \cdot GCI \qquad (5.2.5)$$

As it is apparent from the equation 5.2.5, GCI is equivalent to the relative error of the solution of the parameter of interest. However, it is worth stressing that GCI for unstructured grid refinement might be an overestimation or underestimation of the actual error band. Table 5.2 shows the grid convergence study on temperature.

Table 5.2: Grid convergence study for temperature

Fluid sizing (mm)	# of nodes (million)	# of cells (million)	$T_{j,max}$ (°C)	r	ϵ	GCI
1.2	0.328	0.776	147.6			
1	0.472	1.130	147.2	1.13	0.003	0.013
0.8	0.778	1.913	145.7	1.19	0.010	0.03
0.5	2.088	5.667	144.6	1.44	0.008	0.009

As seen from the table, as we refine the mesh from mesh1 (sizing 1.2mm) to mesh4 (sizing 0.5mm) the value of GCI goes down. If we select mesh4 (0.5mm) based on the $GCI_{3,4}$ the estimate of relative error in temperature is 0.9%, which is quite low.

Table 5.3: Grid convergence study for pressure

Fluid sizing	# of nodes (million)	# of cells (million)	Pressure drop (kPa)	r	ϵ	GCI
1.2	0.328	0.776	12.8			
1	0.472	1.130	12.0	1.13	0.060	0.283
0.8	0.778	1.913	11.3	1.19	0.057	0.180
0.5	2.088	5.667	10.6	1.44	0.017	0.083
0.4	3.3765	9.841	10.4	1.20	0.016	0.047

Table 5.3 shows the result of the grid convergence study on the total pressure drop. As seen from the table, as we refine the mesh from mesh1 (sizing 1.2mm) to mesh5 (sizing 0.4mm), the value of GCI goes down. If we select mesh4 based on the $GCI_{4,5}$ the estimate of relative error in pressure is 4.7%, which is acceptable (less than $1kPa$ for a pressure drop of $20kPa$). The result of this grid convergence study proves that with using a body sizing of $0.5mm$ on the fluid domain (mesh4) proper results can be obtained with an acceptable error band without having to increase the computation time substantially by further mesh refinement. It is worth noting that the grid convergence study is done for the circular design (case1). It is believed that the discretization error band will be within the same range for other design cases due to similarity. Maximum junction temperature and pressure drop are plotted against number of cells along with extrapolated exact solution and error band in figure 5.3.
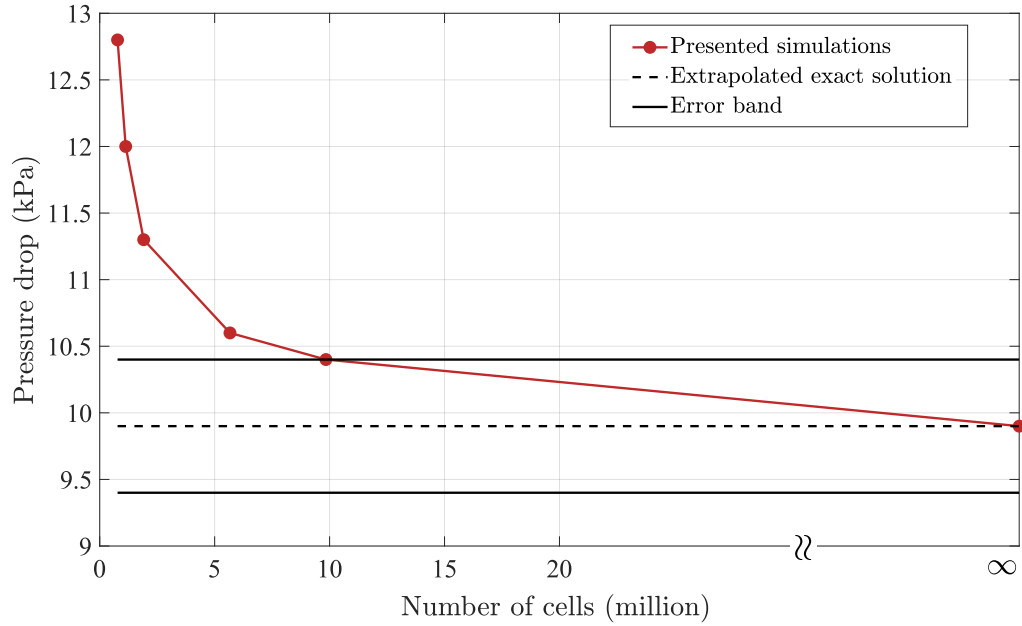
(a) Grid convergence study of pressure drop
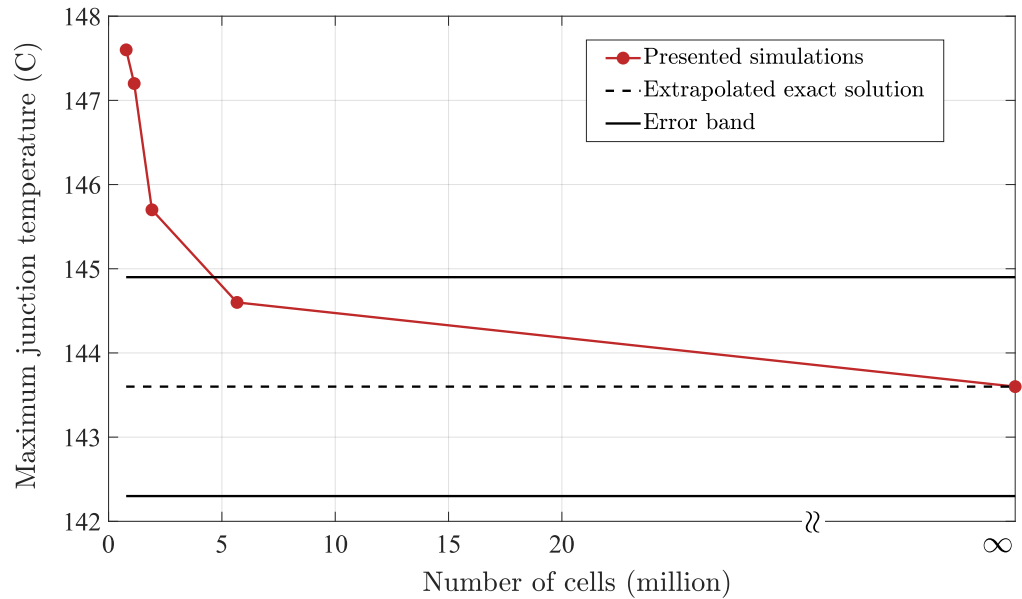
(b) Grid convergence study of temperature

Figure 5.3: Grid convergence study using generalized Richardson extrapolation

5.3   Case 1: Circular Pin-fins

Figure 5.4 shows the maximum and average temperature of the IGBT and diode in case1 design as well as their corresponding thermal resistances against flow rate.
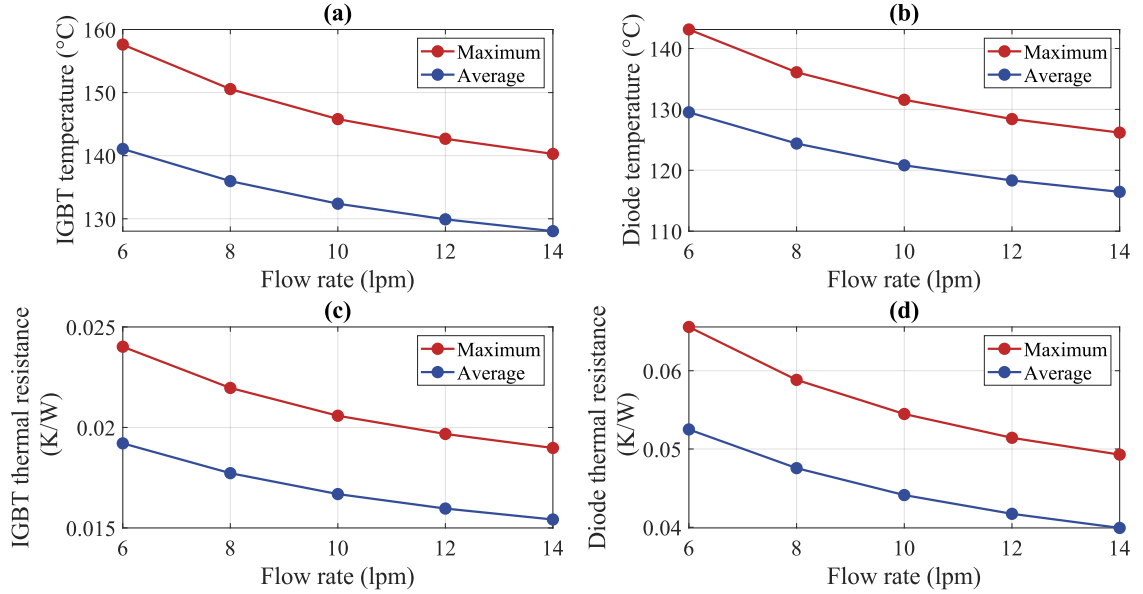
Figure 5.4: Temperature and thermal resistance of circular pin-fin design (baseline design)

Figure 5.5a shows the pressure drop against flow rate for case1 design. The figure includes the overall pressure drop of the cooling jacket (ΔP_t) as well as the pressure drop of the pin-fin section only (ΔP_{fin}). The data points from simulation are shown alongside the fitted power curves and the corresponding goodness-of-fit (R^2). Figure 5.5b shows the average heat transfer coefficient (HTC) on the interface wall against the inlet flow rate. The simulation data points are shown alongside the fitted power curves and the corresponding goodness-of-fit (R^2).

Figure 5.6 show the temperature and pressure contour of case2 design respectively at $10lpm$. It should be noted that since the temperature and pressure contours

can only be plotted for 2D objects, they are only plotted on the outer walls of the system. Therefore, the maximum temperature does not necessarily reflect the maximum junction temperature in each case. This is because of the fact that the power loss is applied as a volumetric heat source to the power devices; thus, the maximum temperature happens somewhere in the middle of the chip and inside it.

Figure 5.6 show the temperature and pressure contour of case1 design respectively at 10 lpm. The pressure and temperature distribution make intuitive sense for many reasons. First, the temperature distribution is not perfectly symmetrical. In fact, this has been quite expected since the fin configuration is not symmetrical due to the staggered fin array and the presence of an offset between the pin-fin rows. The hot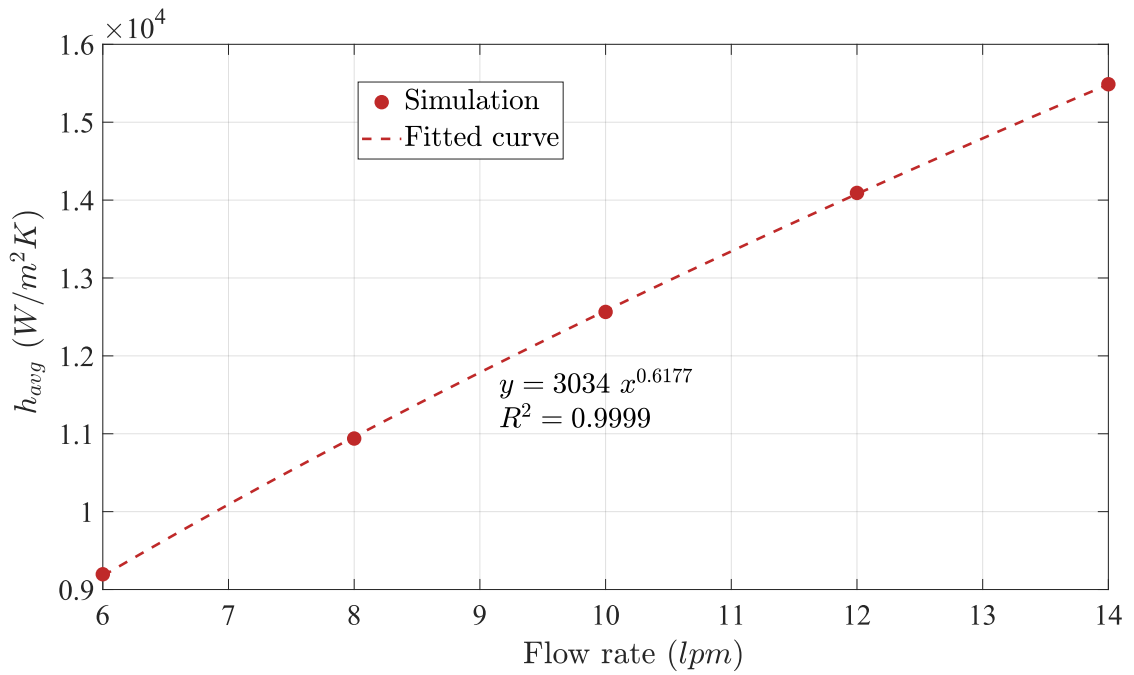 spot intensity is higher on IGBT chips compared to diodes, which was quite predictable because of the higher heat flux of IGBT. We can see that the temperature distribution of diodes is stretched toward the nearby IGBT, resulting from heat spreading. The same thing has happened for the IGBTs, which are located at the corners. The middle IGBT has the highest temperature and highest hot spot intensity. The far-left phase leg of the power module has the lowest temperature. The far-right phase leg has the highest temperature. This is quite understandable as the liquid gets warmer from inlet to outlet. The pressure drop results are also intuitively sensible, with the maximum pressure happening at the inlet and minimum pressure (almost zero gauge pressure) happening at the outlet. Similar effects are observed for other design cases as well. It should be noted that although the outlet boundary condition is set to zero gauge pressure, the boundary condition will be met with a certain tolerance. Therefore the outlet pressure is not exactly zero. This explains the slight difference between the maximum pressure on the contour and the pressure drop value.

$$y = 0.1303x^{1.918}$$
$$R^2 = 0.9999$$

$$y = 0.0992x^{1.884}$$
$$R^2 = 0.9999$$
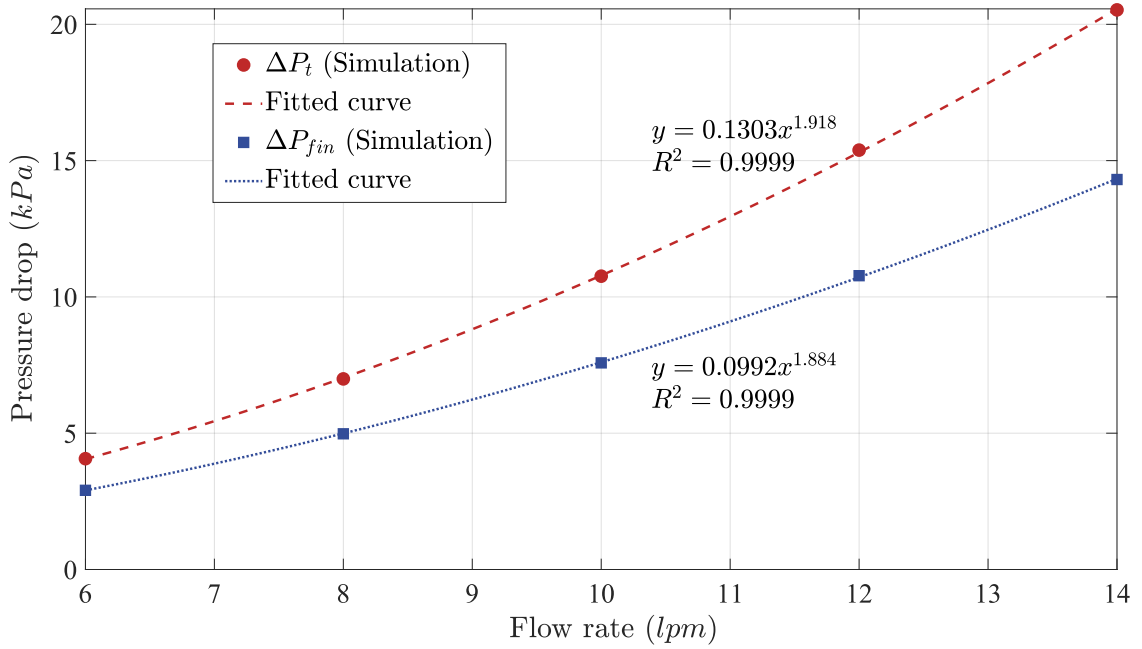
(a) Pressure drop of circular pin-fin design (baseline design)

$$y = 3034\ x^{0.6177}$$
$$R^2 = 0.9999$$

(b) Heat transfer coefficient of circular pin-fin design (baseline design)

Figure 5.5: Characteristic curves of case 1 design (baseline)
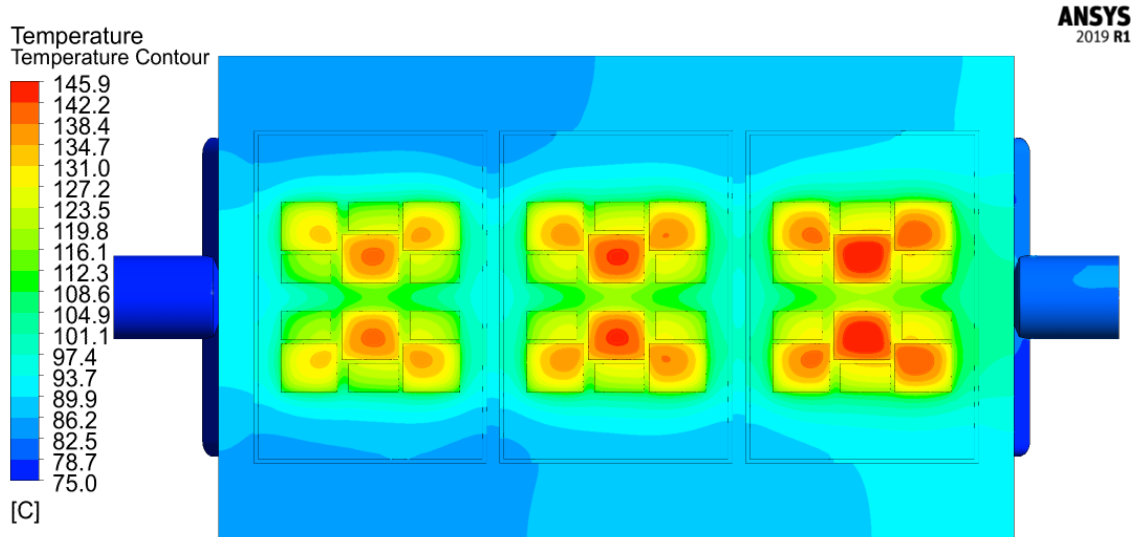
(a) Temperature contour of circular pin-fin design (baseline design)
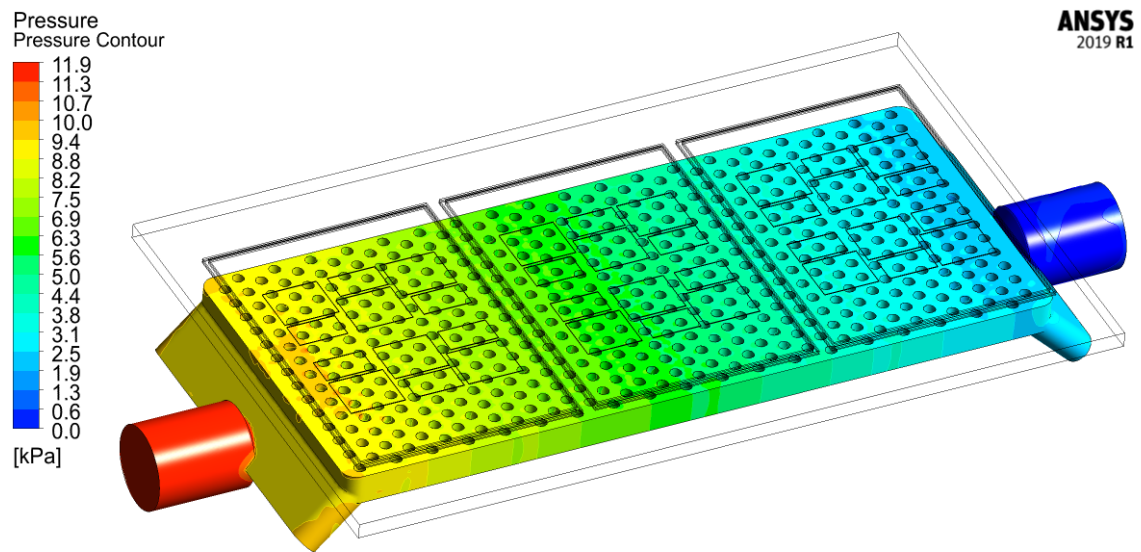
(b) Pressure contour of circular pin-fin design (baseline design)

Figure 5.6: Result of case1 (baseline) at average fow rate of 10 *lpm*

5.4   Case 2: Drop-shaped Pin-fins

Figure 5.7 shows the maximum and average temperature of the IGBT and diode in case2 design as well as their corresponding thermal resistances against flow rate.

Figure 5.7: Temperature and thermal resistance of drop-shaped pin-fin design

Figure 5.8a shows the pressure drop against flow rate for case2 design. The figure includes the overall pressure drop of the cooling jacket (ΔP_t) as well as the pressure drop of the pin-fin section only (ΔP_{fin}). The data points from simulation are shown alongside the fitted power curves and the corresponding goodness-of-fit (R^2). Figure 5.8b shows the average heat transfer coefficient (HTC) on the interface wall against the inlet flow rate. The simulation data points are shown alongside the fitted power curves and the corresponding goodness-of-fit (R^2).

Figure 5.9 show the temperature and pressure contour of case1 design respectively at 10 lpm.

(a) Pressure drop of drop-shaped pin-fin design

(b) Heat transfer coefficient of drop-shaped pin-fin design

Figure 5.8: Characteristic curves of case 2 design (drop-shaped)
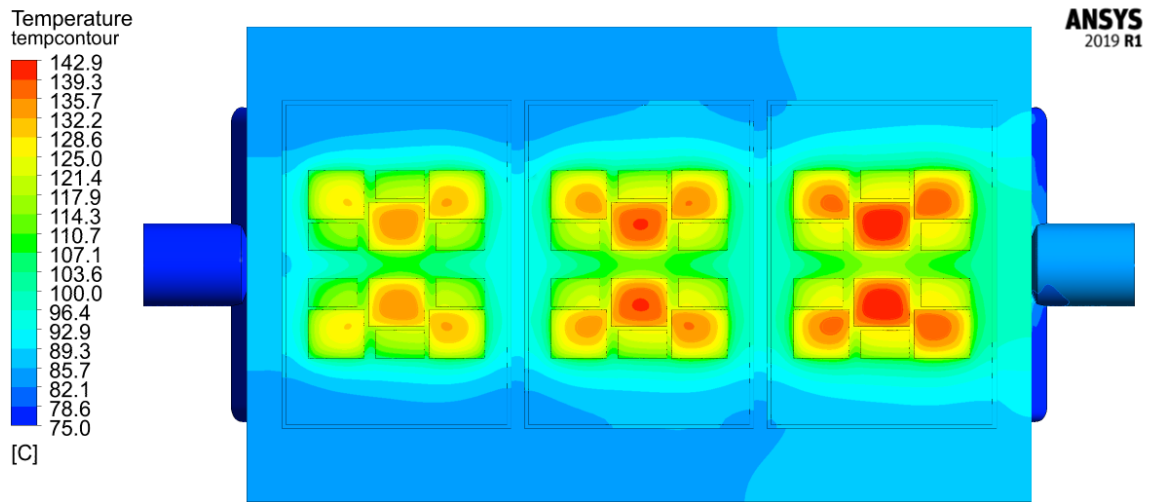
(a) Temperature contour of drop-shaped pin-fin design
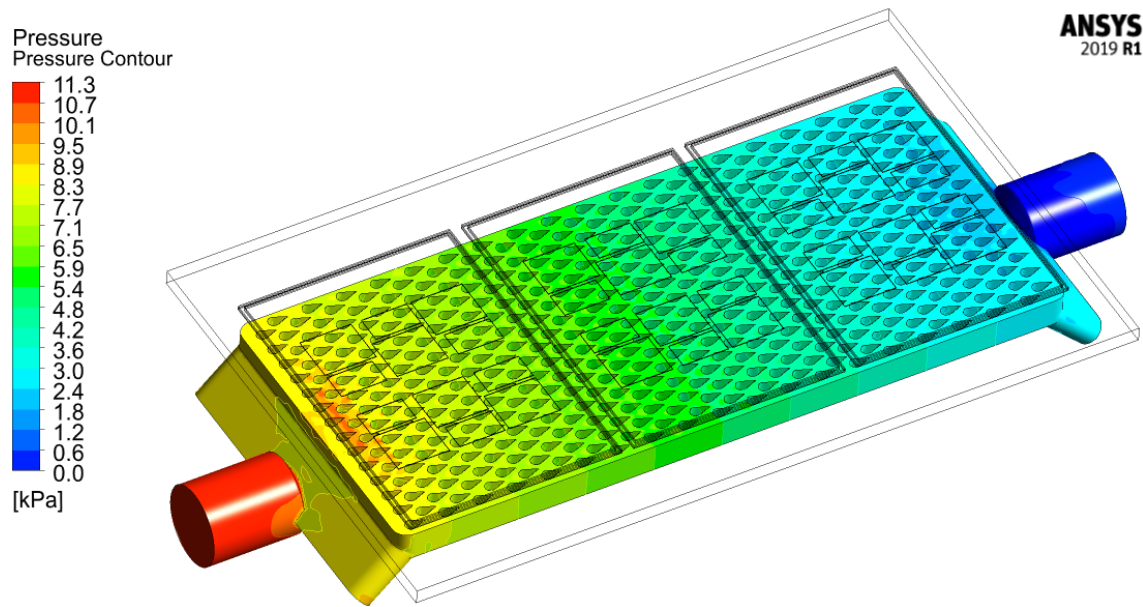
(b) Pressure contour of drop-shaped pin-fin design

Figure 5.9: Result of case2 (drop-shaped) at average fow rate of 10 *lpm*

5.5   Case 3: Symmetric Convex Pin-fins

Figure 5.10 shows the maximum and average temperature of the IGBT and diode in case3 design as well as their corresponding thermal resistances against flow rate.
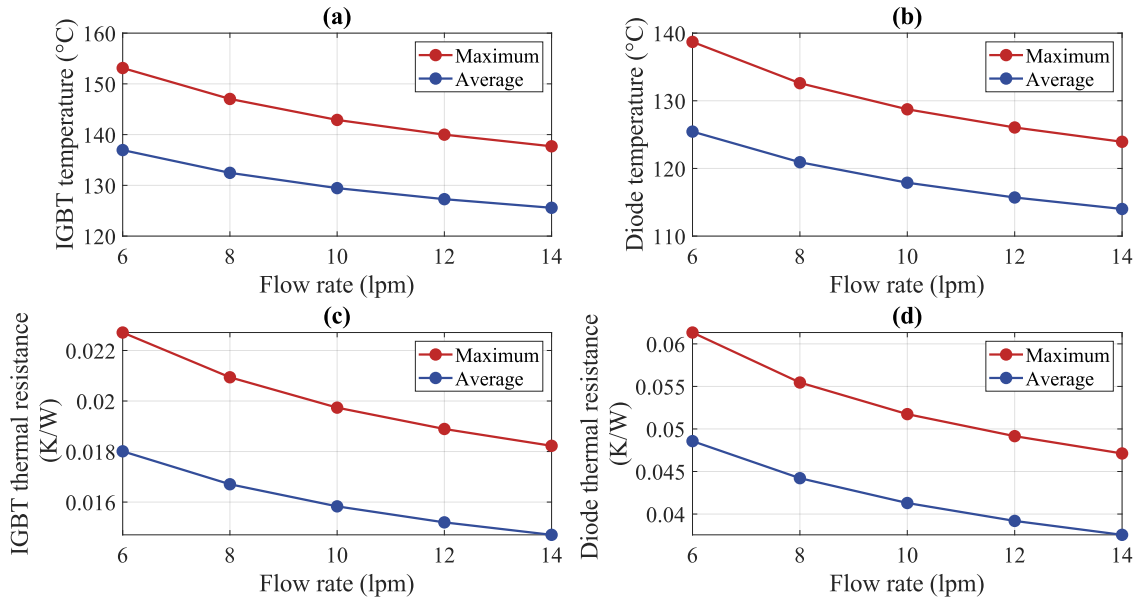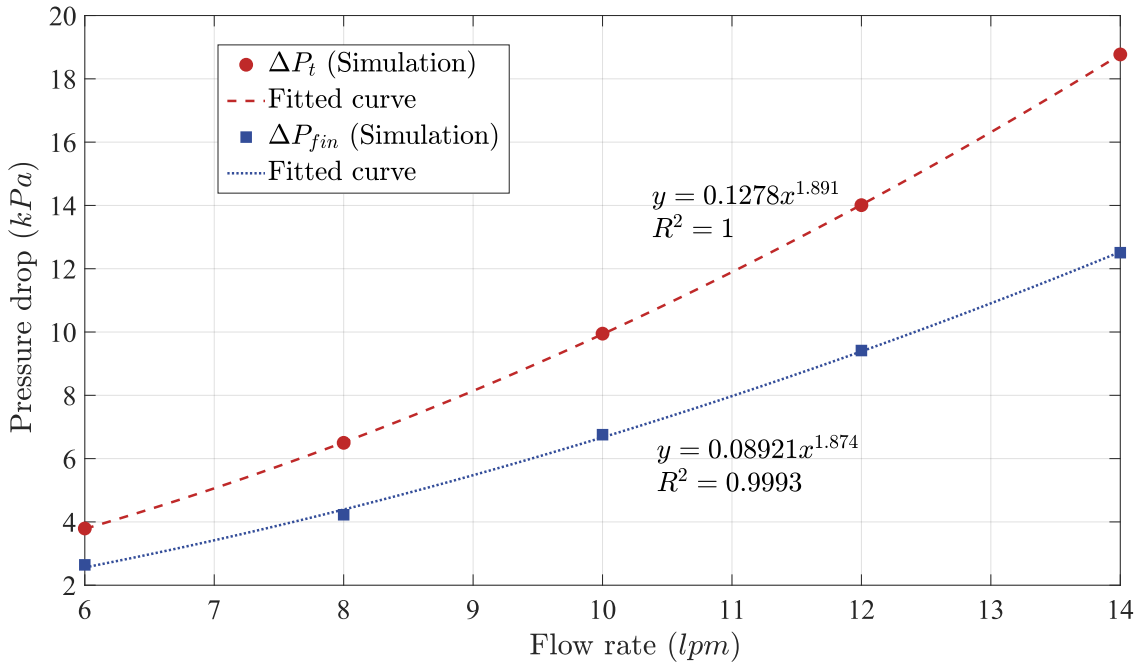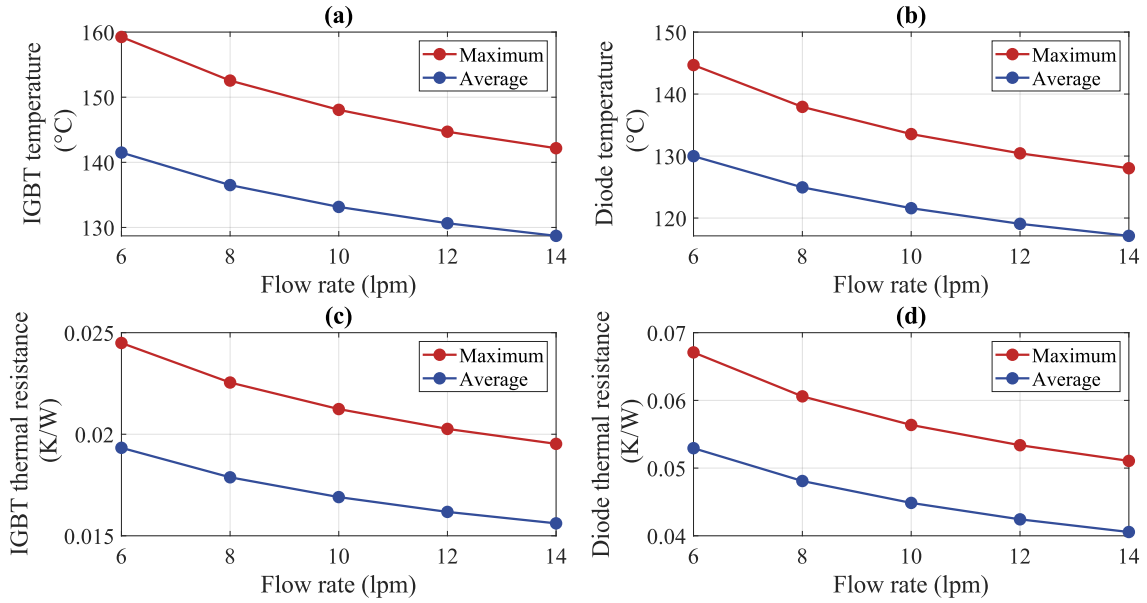

Figure 5.10: Temperature and thermal resistance of symmetric convex lens pin-fin design

Figure 5.11a shows the pressure drop against flow rate for case3 design. The figure includes the overall pressure drop of the cooling jacket (ΔP_t) as well as the pressure drop of the pin-fin section only (ΔP_{fin}). The data points from simulation are shown alongside the fitted power curves and the corresponding goodness-of-fit (R^2). Figure 5.11b shows the average heat transfer coefficient (HTC) on the interface wall against the inlet flow rate. The data points from simulation are shown alongside the fitted power curves and the corresponding goodness-of-fit (R^2).

Figure 5.12 show the temperature and pressure contour of case3 design respectively at $10lpm$.
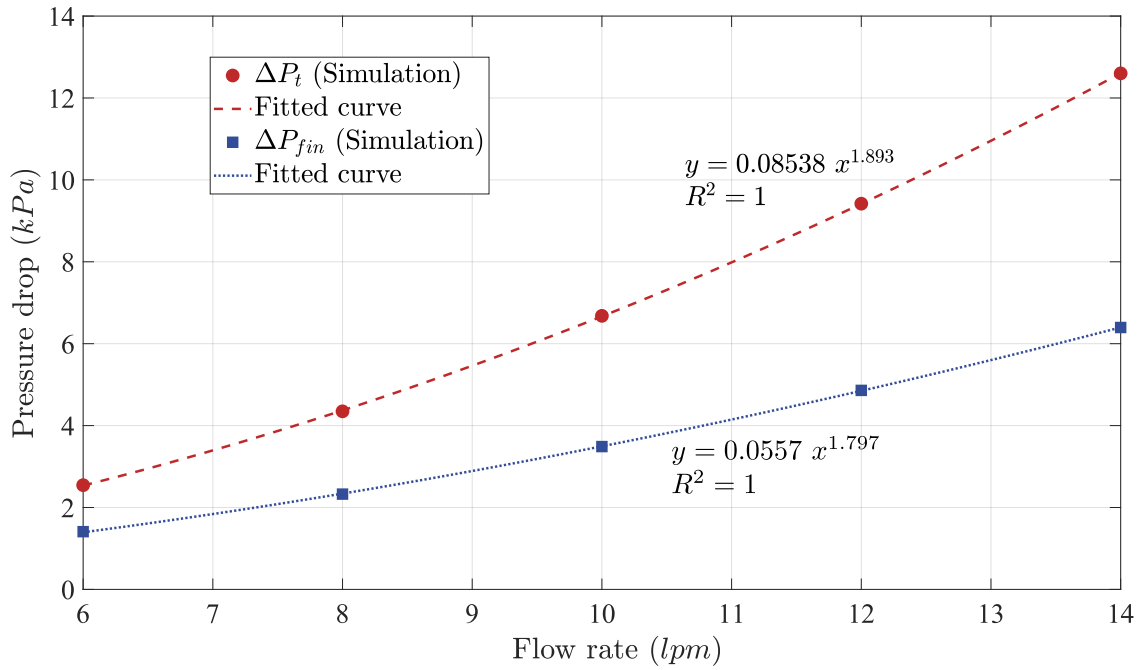
(a) Pressure drop of symmetric convex lens pin-fin design
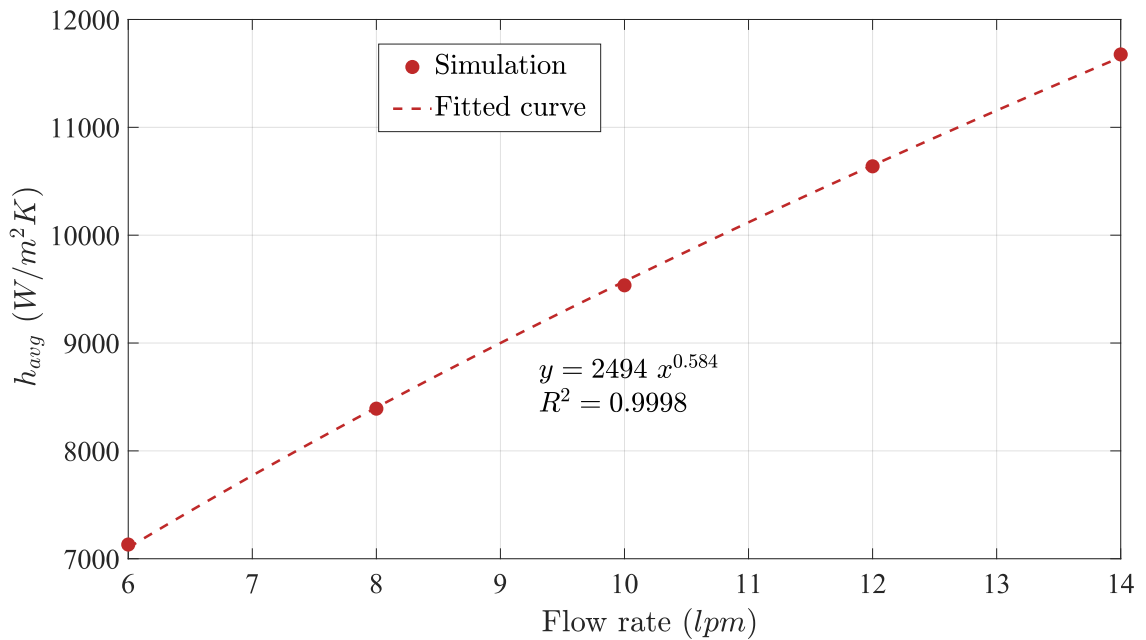
(b) Heat transfer coefficient of symmetric convex lens pin-fin design

Figure 5.11: Characteristic curves of case 3 design (symmetric convex lens)
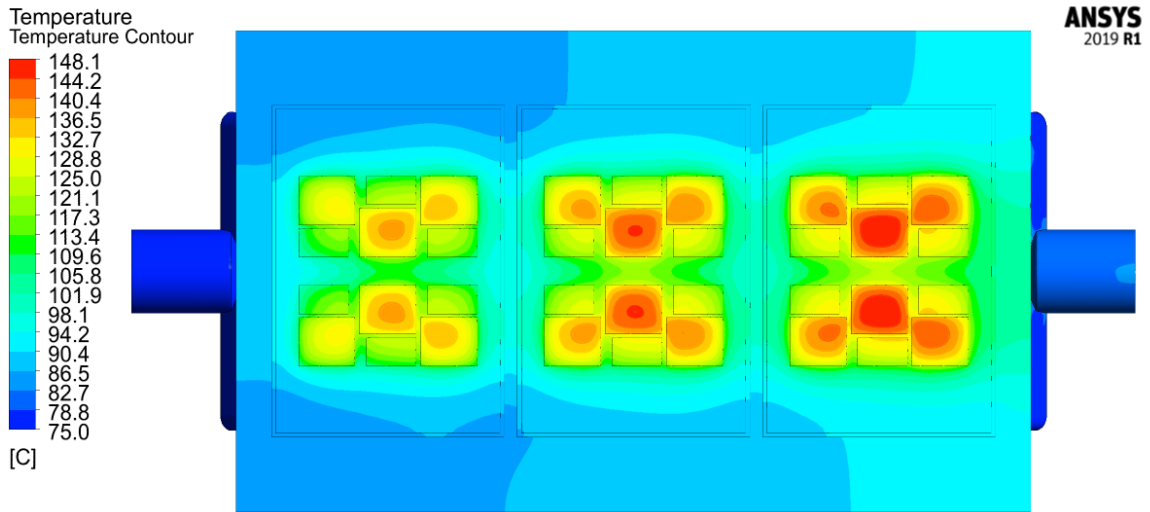
(a) Temperature contour of symmetric convex lens pin-fin design
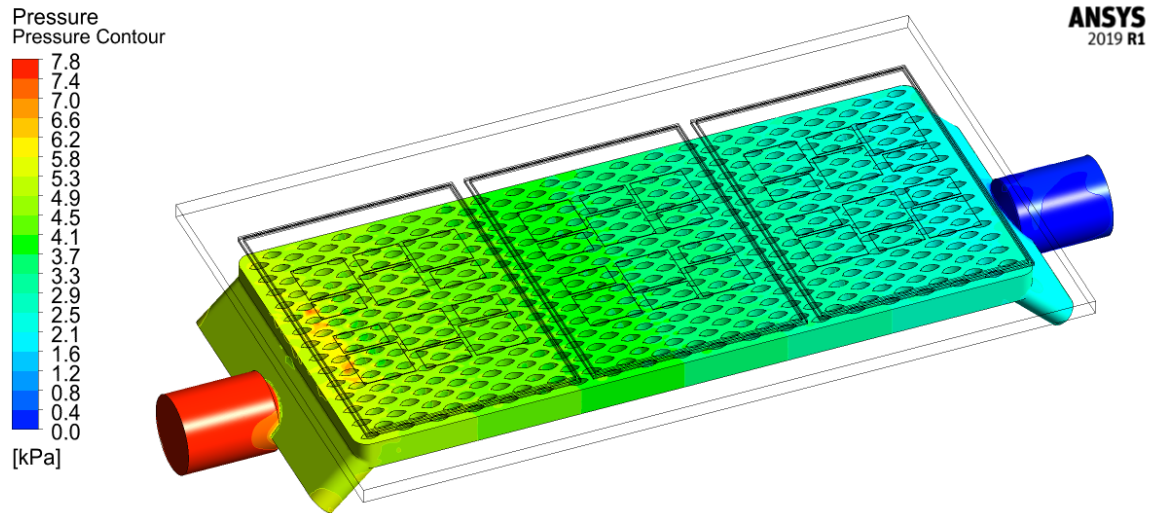
(b) Pressure contour of symmetric convex lens pin-fin design

Figure 5.12: Result of case3 (symmetric convex lens) at average fow rate of 10 *lpm*

5.6   Case 4: Offset Strip Pin-fins

Figure 5.13 shows the maximum and average temperature of the IGBT and diode in case4 design as well as their corresponding thermal resistances against flow rate.
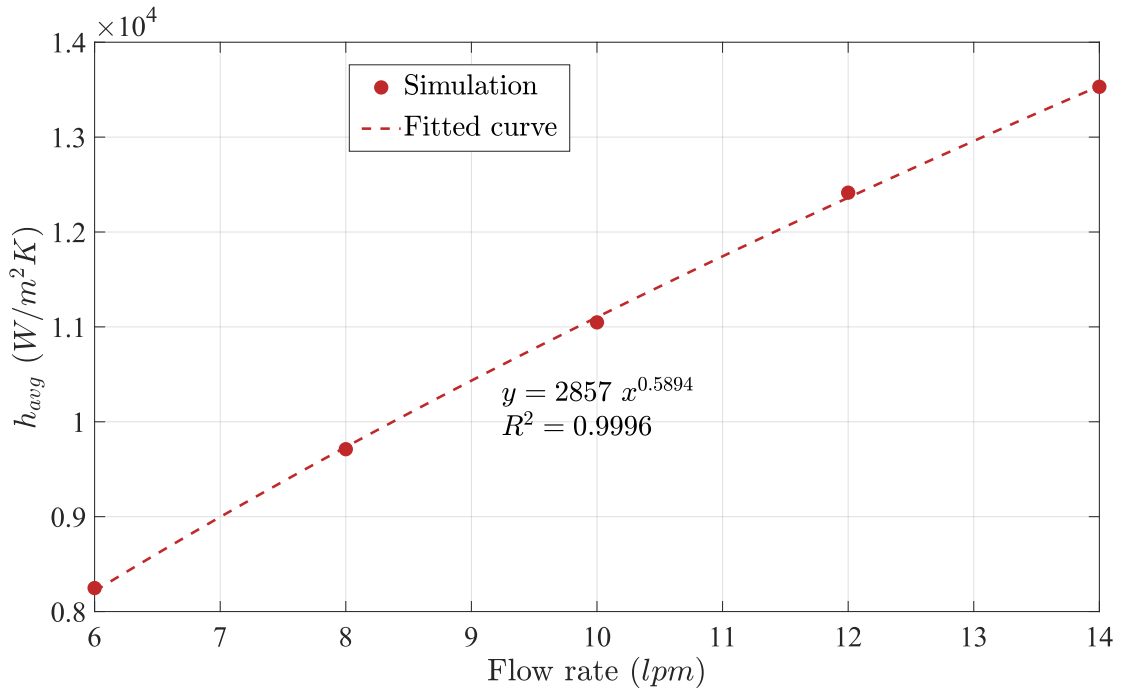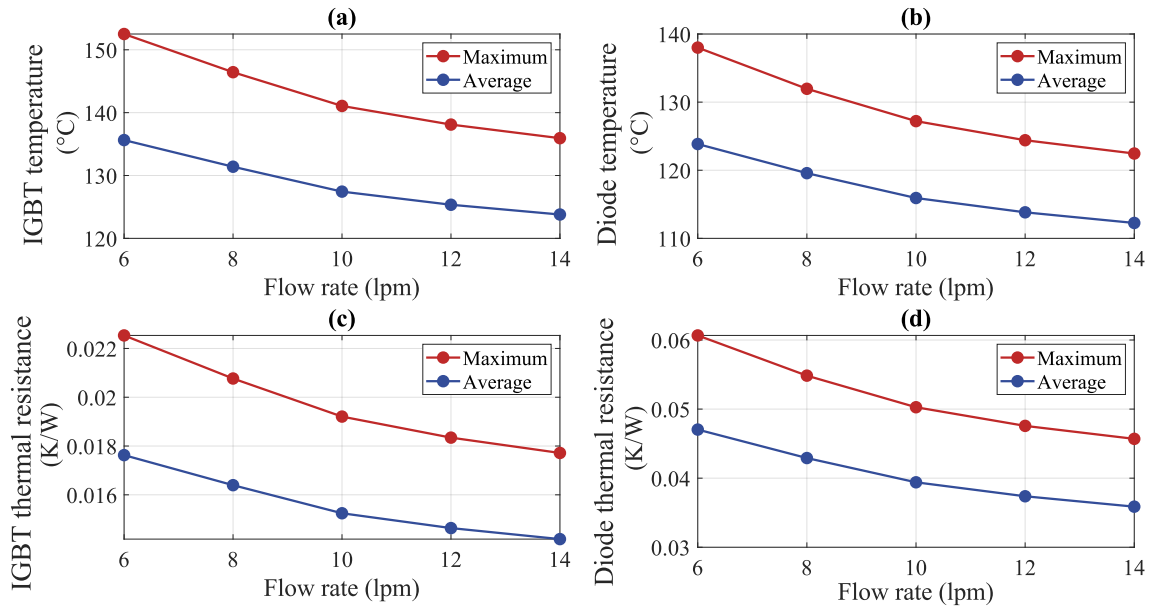

Figure 5.13: Temperature and thermal resistance of OSPF design

Figure 5.14a shows the pressure drop against flow rate for case4 design. The figure includes the overall pressure drop of the cooling jacket (ΔP_t) as well as the pressure drop of the pin-fin section only (ΔP_{fin}). The data points from simulation are shown alongside the fitted power curves and the corresponding goodness-of-fit (R^2). Figure 5.14b shows the average heat transfer coefficient (HTC) on the interface wall against the inlet flow rate. The simulation data points are shown alongside the fitted power curves and the corresponding goodness-of-fit (R^2).

Figure 5.15 show the temperature and pressure contour of case4 design respectively at $10lpm$.

$$y = 0.1586\ x^{1.873}$$
$$R^2 = 1$$

$$y = 0.135\ x^{1.8}$$
$$R^2 = 0.9999$$
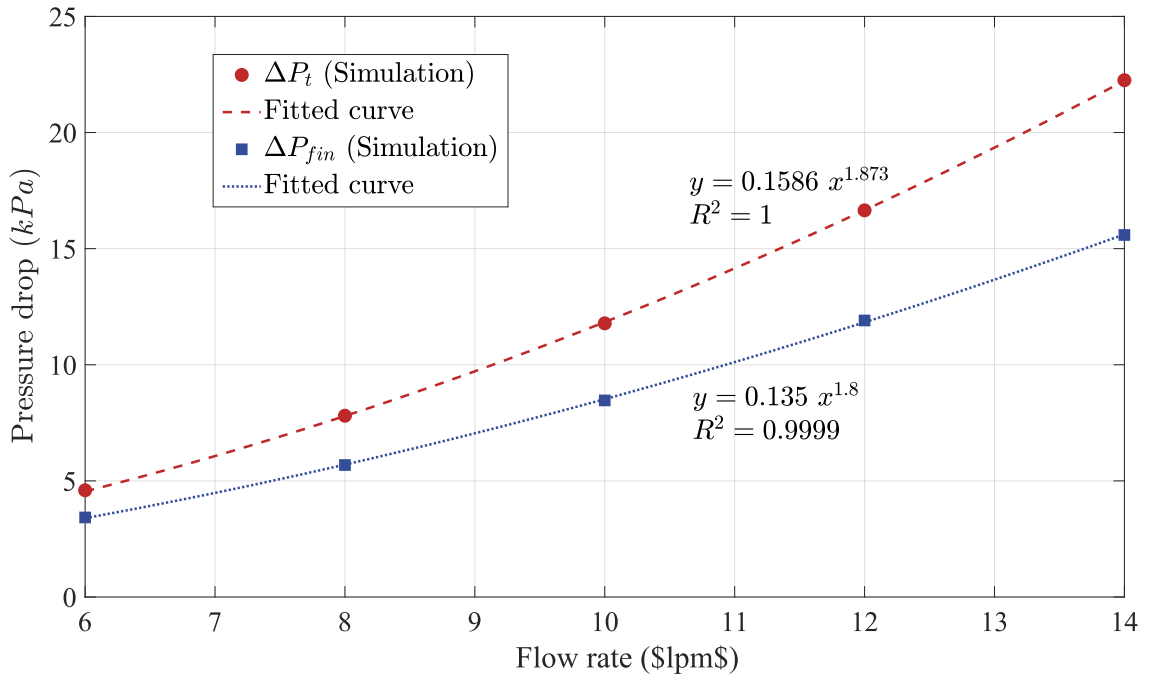
(a) Pressure drop of OSPF design

$$y = 2442\ x^{0.5909}$$
$$R^2 = 0.9998$$
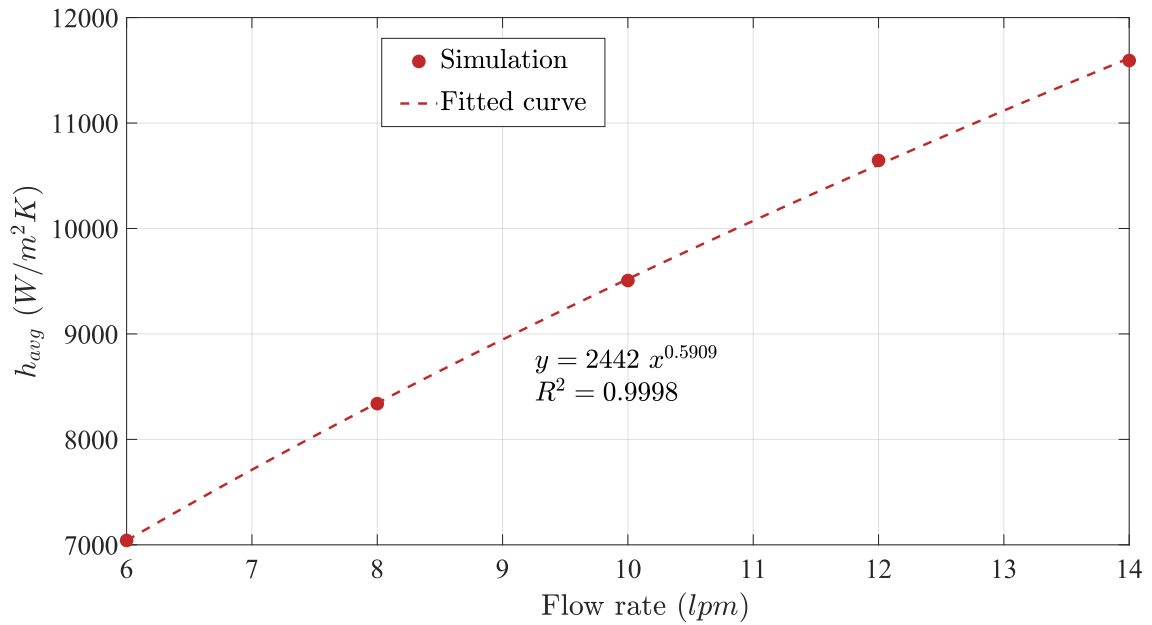
(b) Heat transfer coefficient of OSPF design

Figure 5.14: Characteristic curves of case 4 design (OSPF)

132
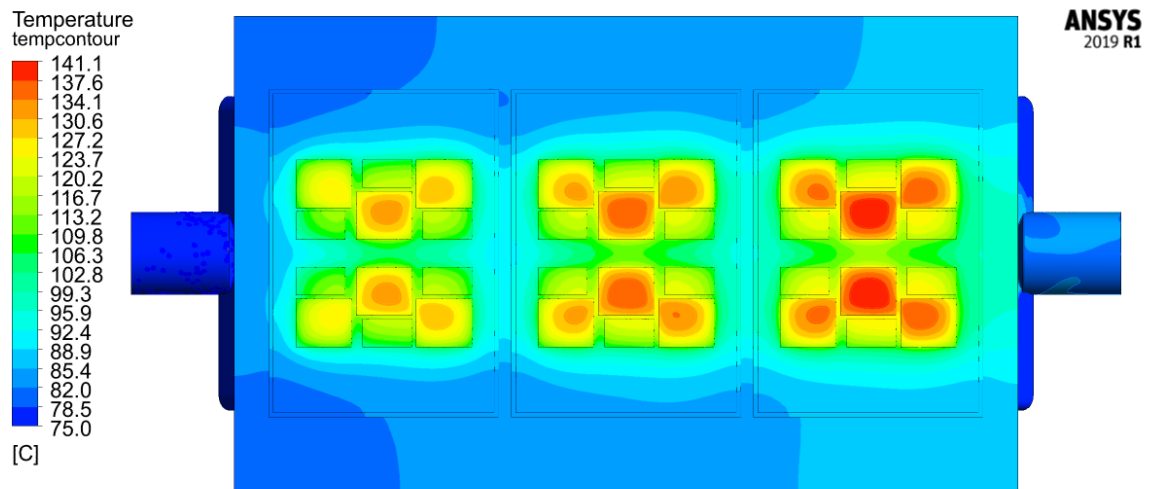
(a) Temperature contour of OSPF design
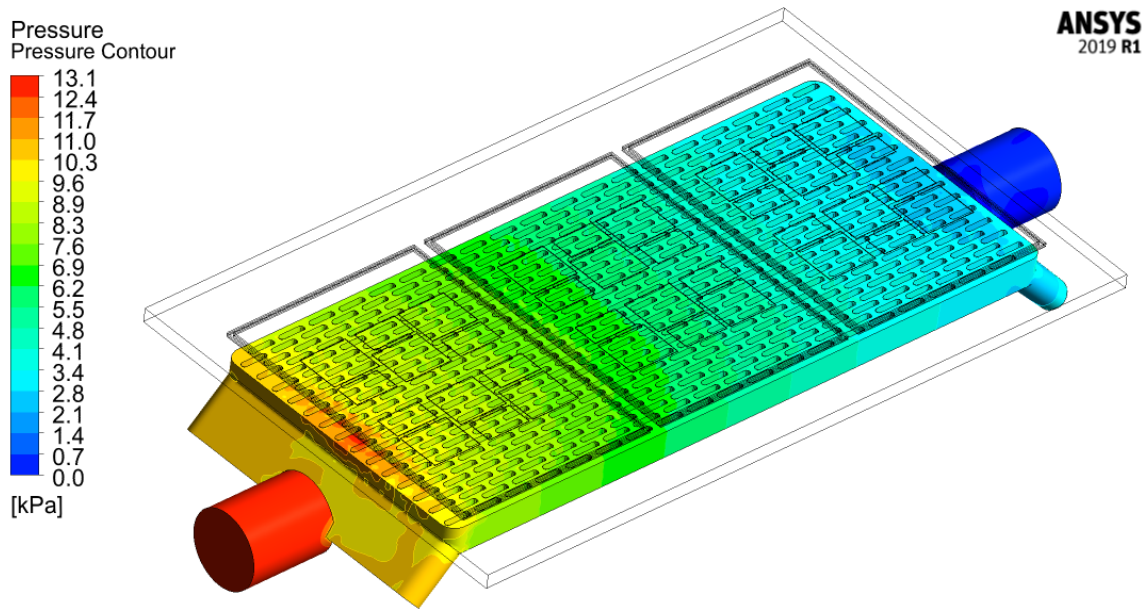
(b) Pressure contour of OSPF design

Figure 5.15: Result of case4 (OSPF) at average fow rate of 10 *lpm*

5.7   Benchmarking and Discussions

Figure 5.16 shows the overall pressure drop (5.16a) and thermal resistance (5.16b) of each design candidate against the inlet flow rate.

The first conclusion that can be immediately drawn from figure 5.16 is that the drop-shaped pin-fin has performed better than the circular baseline design. This can be inferred from the fact that not only case 2 has a lower pressure drop than case 1, but it also has a lower thermal resistance. This was quite expected due to the oblong shape of the drop-shaped fins. The circular shape creates a large wake region behind the pin, which results in a higher pressure loss. The wake region is smaller for the drop-shaped fin. This has been shown in figure 5.17. Although the fin hydraulic diameter is the same in both designs, the drop-shaped fin's peripheral surface area is higher than circular fin. This has contributed to the higher heat transfer rate in case 2 compared to case 1. Since the drop-shaped fin is extended along the stream-wise direction, the separation happens later on the fin surface as opposed to the circular design. This can be seen in the velocity contours of both designs.

Drawing conclusions about the thermal performance of other design cases relative to each other does not seem to be as easy as the comparison of cases 1 and 2. This is because the pressure drop in those cases is higher than the baseline and the thermal resistance is lower than the baseline. Therefore a thermal performance criterion is needed to finalize the comparative analysis. When evaluating the thermal performance of the four cases of pin-fin design, at a certain flow rate, the TPI (defined in equation 2.2.10) will boil down to:
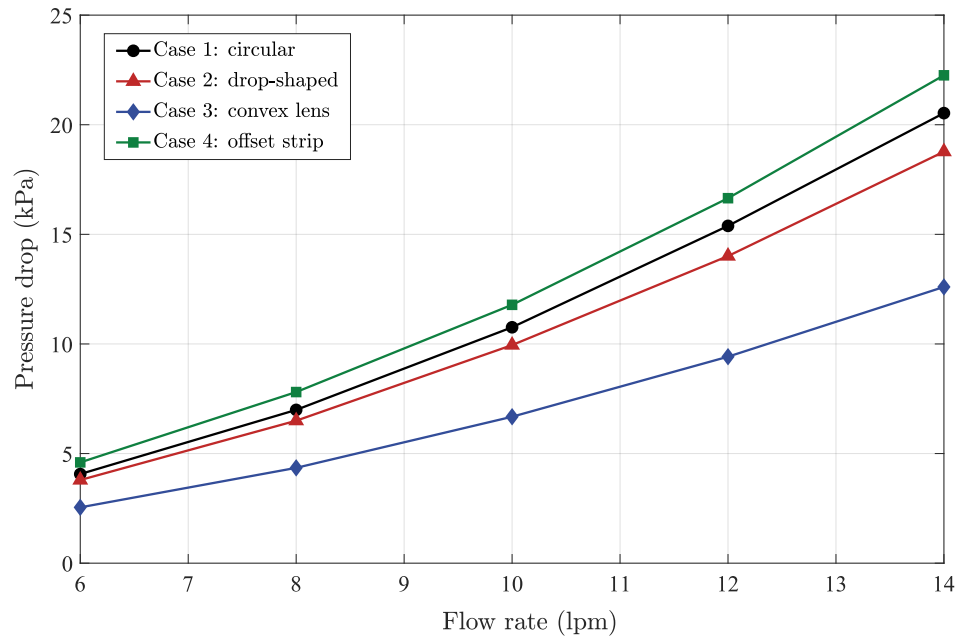
(a) Pressure drop comparison of design candidates
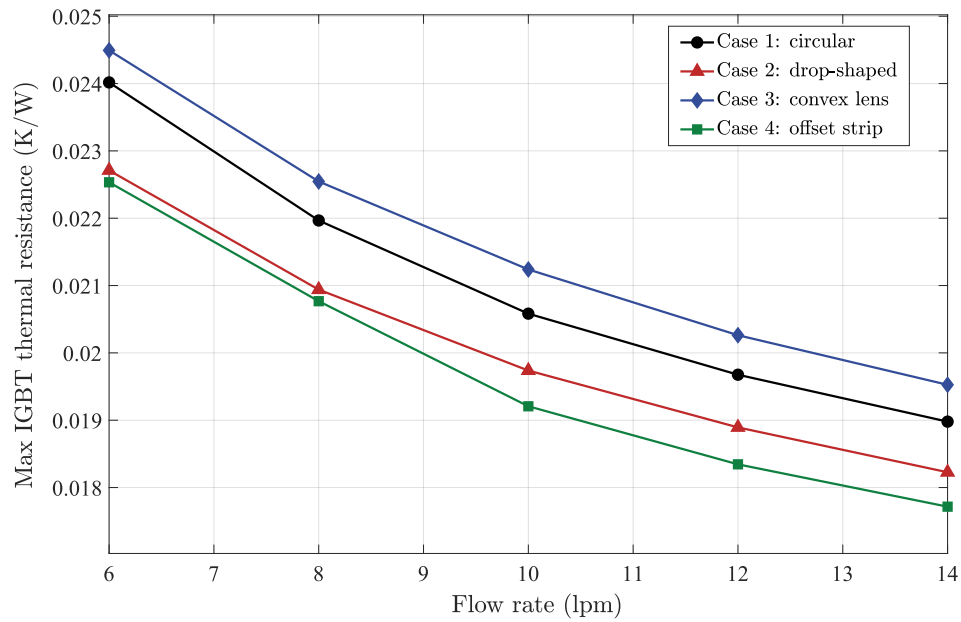
(b) Comparison of maximum junction to fluid thermal resistance (IGBT)

Figure 5.16: General benchmark of design cases
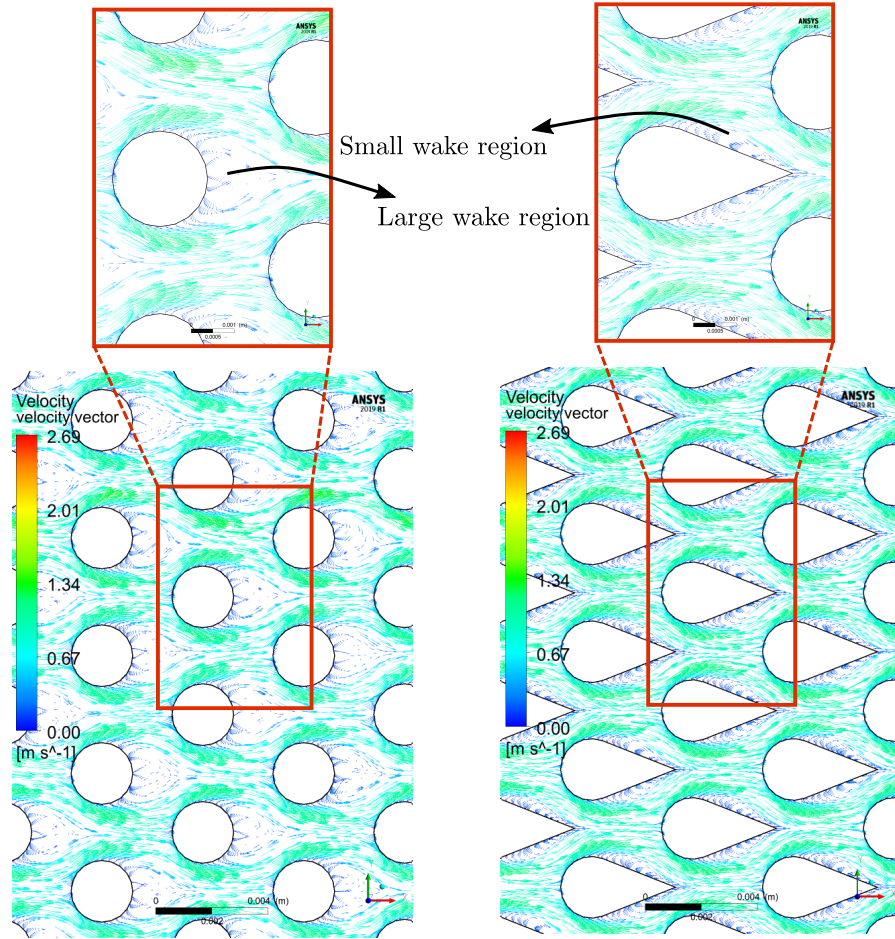
Figure 5.17: Comparison of velocity field for circular and drop-shaped fins at the pin-fin cross-section

$$\eta_{PF} = \frac{\overline{h_{eff}}/\overline{h_{0,eff}}}{(\frac{\Delta P_{fin}A_{min}^2}{\Delta P_{fin,0}A_{min,0}^2})^{1/3}} \qquad (5.7.1)$$

This is only true if we use the definition of 2.2.8 for computing the friction factor. In this definition, ΔP is the pressure drop associated with the pin-fin section only. The local Reynolds number based on the maximum velocity across the fin array can be obtained using the minimum cross-section area for each design case. The minimum

cross-section area is listed in table 5.4 as well as the minimum channel width and area enhancement of each design case.

Table 5.4: Area enhancement ratio, minimum surface area and channel width for different design cases

Design case	Case 1 (circular)	Case 2 (drop-shaped)	Case 3 (symmetric lens)	Case 4 (OSPF)
$A_{min}(mm^2)$	12	12	14.4	9.6
$d_{min}(mm)$	2	1.07	1.35	0.8
EA	3.33	4.33	4.05	5.48

There are two ways to go about the thermal performance evaluation. The first way is the one that is mentioned above (equation 5.7.1). Since the pin-fin section's pressure drop is used in this method, the approach maintains the generality and can be used for thermal evaluation in other studies. The result of this comparison is applicable to other studies where a different cooling jacket design is used (different inlet/outlet configuration) but the thermal performance of the pin-fin section is the main topic of interest. However, since the inlet/outlet channel configuration, as well as the type of fluid distribution, significantly affect the pressure drop, it is also important to consider their effect on the overall thermal performance assessment. For this reason, the second way of TPI calculation incorporates the overall pressure drop of the heatsink from inlet to outlet. If we use the loss coefficient definition of equation 2.2.7 and substitute it into equation 2.2.10, the simplified result will be as follows:

$$\eta_t = \frac{\overline{h_{eff}}/\overline{h_{0,eff}}}{(\frac{\Delta P_t}{\Delta P_{t,0}})^{1/3}} \tag{5.7.2}$$

137

Where ΔP_t and $\Delta P_{t,0}$ are total pressure drop of the candidate design and baseline design, respectively. The TPI based on the pin-fin section (η_{PF}) and the total pressure drop (η_t) is plotted against flow rate in figure 5.18.

As seen from figure 5.18a if we consider the TPI of pin-fin section case4 design (offset strip pin-fin) outperforms all the candidates. Then case2 and case3, and case1 come in descending order. On average, case4, case2, and case3 perform 39%, 20%, and 6% better than the baseline design, respectively.

If we switch to the overall thermal performance based on the total pressure drop, the comparative advantage of each design will stay the same. However, the quantified thermal performance advantage of each design will change. On average, case4, case2, and case3 are performing 20.7%, 18%, and 8.8% better than the baseline design, respectively.

Even though the TPI comparison is a notable contribution to the available literature in the field, it is not the only figure of merit that should be considered for heatsink comparison. Manufacturing cost and overall power density of the cooling system are as important. Since the heatsinks discussed in this study have the same geometrical envelope, the volumetric power density is the same for all of them. Therefore gravitational power density must be considered as another figure of merit.

To be able to provide a cost comparison, CNC machining is assumed for heatsink manufacturing. The total manufacturing cost is the summation of tool cost (C_T), material cost (C_M), and machining cost, which is roughly proportional to the machining time [64]:

$$C_{\text{total}} = C_T + C_M + t \times R \tag{5.7.3}$$
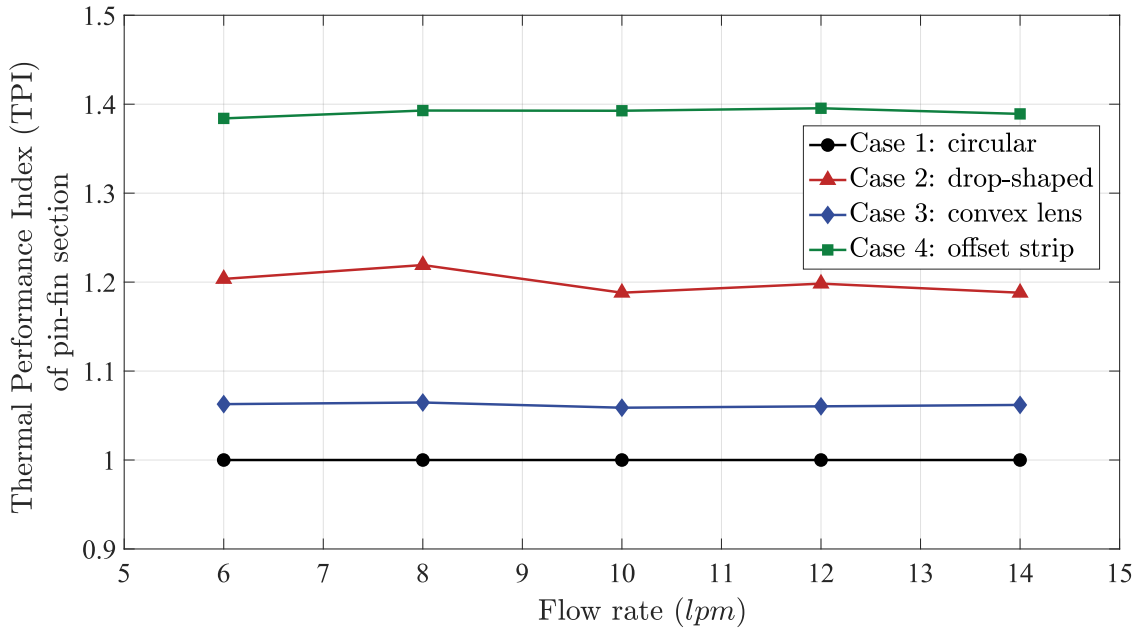
(a) Thermal performance index of the pin-fin section
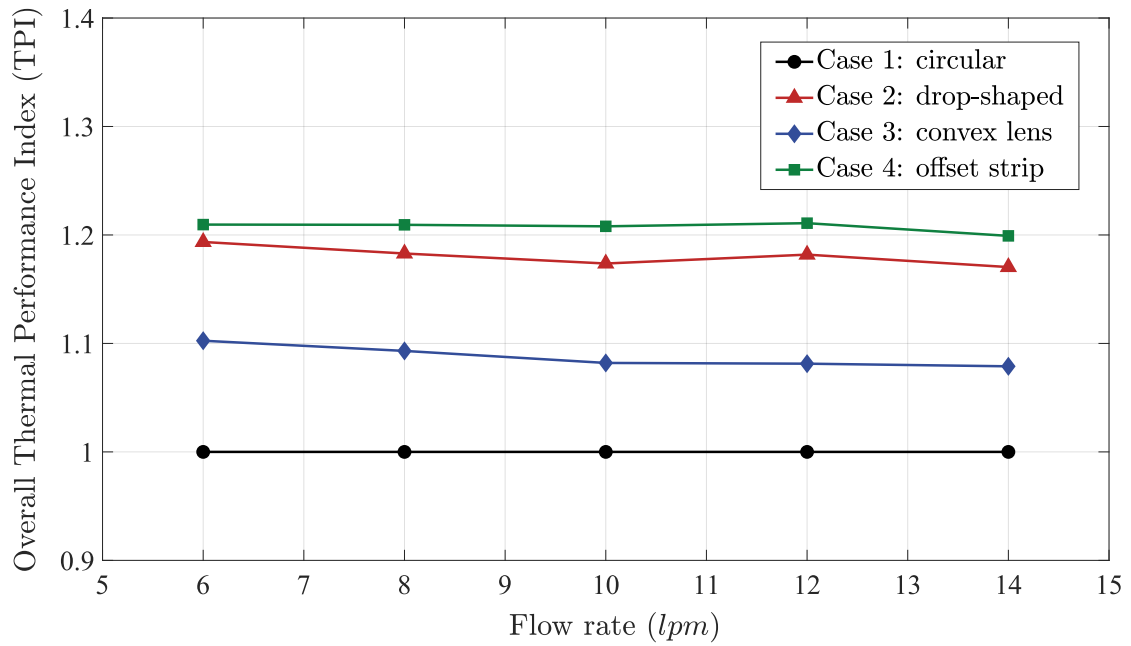
(b) Overall thermal performance index of each cooling jacket design

Figure 5.18: Thermal performance index (TPI) against flow rate

Where R is the constant of proportionality, which is not known and is not required for the comparative cost analysis.

Considering the fact that the machining cost is significantly higher than the tool cost and material cost, we can neglect the first two terms and estimate the manufacturing cost through machining time:

$$C_{\text{total}} \simeq t \times R \tag{5.7.4}$$

Machining time is the summation of the times allocated to setup, tool change, cleaning, and the actual machining. Considering the fact that CNC micro-machining will be used for fabrication, we can assume that the machining time is dominant; thus, we can simplify equation 5.7.5a and derive 5.7.5b.

$$t = t_{\text{machining}} + t_{\text{toolchange}} + t_{\text{setup}} + t_{\text{cleaning}} \tag{5.7.5a}$$

$$t \simeq t_{\text{machining}} \tag{5.7.5b}$$

In general, the machining time relates to the feed rate (F), and machining distance through the following equation:

$$t_{\text{machining}} = \frac{d_{machining}}{F} \tag{5.7.6}$$

Machining distance is the overall distance that the tool travels across the workpiece to complete the machining task. Apparently, machining distance is a function of tool geometry and workpiece geometry. Feed rate is a function of the material and strength of the tool and the workpiece in use. Since all of these parameters are constant for

the given heatsinks, the feed can be assumed the same for all design cases. Therefore, the relative machining time will be only a function of the tool geometry and the workpiece geometry. The end-milling tool geometry for each case will be specified by the minimum distance between the fins that are listed in table 5.4. Therefore the tool diameter should be equal to smaller than 2mm, 1.07mm, 1.35mm, and 0.8mm for case1 to case4, respectively. The total machining distance is equal to the machining distance of a single cut level times the number of cut levels. The cut level is a function of the depth of cut, which is normally a percentage of the tool diameter. It is often limited to 50% of the tool diameter. Therefore for a 0.8mm end-mill, the depth of cut for each cut level is 0.4mm. Thus, 15 cut levels are required to mill out the OSPF geometry for case4. In case 1, where the end-mill diameter is 2 mm, the depth of cut is 1mm; therefore, only 6 levels of cut are required. It is estimated that the machining distance of each cut level is the same for all design cases due to similarity. This assumption was tested in the Siemens NX CAM tool using the same feed rate for circular and OSPF design. The machining time for a single cut level was 42 minutes and 40 minutes for circular and OSPF design, respectively. Therefore the assumption of the same machining distance for each cutting level is valid. Thus, the machining time is proportional to the number of cut levels. Since the depth of cut was a fraction of tool diameter, one can conclude that the machining time is inversely proportional to the tool diameter:

$$t_{\text{machining}} \propto \frac{1}{d_{min}} \tag{5.7.7}$$

Equation 5.7.7 along with equation 5.7.4 provides an estimation of the relative cost of heatsink machining. It should be noted that specifying the constant of proportionality

is not deemed important as the cost comparison is the main objective. It is worth mentioning that machining of mini pin-fins is not economical for mass production and is only suited for prototyping or low to medium volume production [64]. For other manufacturing techniques such as casting or powder injection molding, since the mold cost is mainly a function of mold size and mass, it is highly expected to have almost comparable cost for all of the design candidates.

Table 5.5 is the summary of mass, cost, and thermal performance comparison of the design cases. All of the values are relative to the baseline circular design $(Cost_0, Mass_0)$.

Table 5.5: TPI, mass, and cost comparison of design candidates

	circular	drop-shaped	convex lens	OSPF
TPI	1	1.2	1.06	1.4
$Mass/Mass_0$	1	1.096	1.07	1.207
$Cost/Cost_0$	1	1.87	1.48	2.5

The values of table 5.5 are normalized and mapped to the range of 1–4 for better representation on a radar chart (figure 5.19). The estimated cost is based on end-milling operation and should be revised if other fabrication methods are in place. The radar chart could be used as a framework for thermal designers to choose the cooling option according to their needs. According to the chart. If the designer wants to trade-off a little of mass and cost to achieve better TPI, convex lens, cone-shaped or offset strip design could be selected, respectively. However, as per the chart, we can observe that by selecting the convex-lens shape, we are almost compromising as much cost and mass as the drop-shaped design. However, the gain of thermal performance

in drop-shaped design is much higher than the convex lens. Thus, one may want to choose drop-shaped over the convex lens for higher TPI gain. The choice of thermal performance and mass/cost trade-off entirely depends on the designer's decision and the manufacturer's long-term benefit. We should keep in mind that in an ideal case of comparison all of the factors including the thermal performance index must be translated into the cost. For instance, TPI can be translated into the life-time of the module and how much less spending could happen when having a more reliable power module.
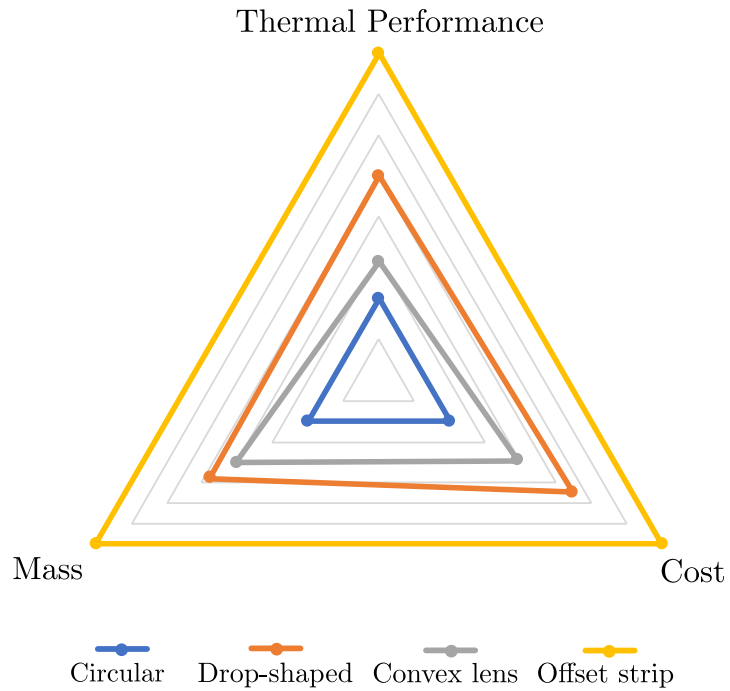
Figure 5.19: TPI, mass, and cost benchmark of design candidates

5.8   Simulation Verification

Unlike drop-shaped and symmetric convex fins, there are numerous studies that have analytically, numerically, or experimentally investigated circular pin-fins and offset strip fin heatsinks. Studies on symmetric convex fin heatsinks are centered around micro-scale fin geometries where the range of Reynolds number is entirely different than the mini-scale pin-fins [95], [103], [104], [105]. Therefore the results/correlations developed by the aforementioned studies can not be applied to the current study for further verification of the results. Studies such as the work of Zukauskas ([137], [138]), Metzger et al. ([139]), Manglik and Bergles ([111]), and Kays and London ([140]) have experimentally investigated circular pin-fins and offset strip fins. These studies' experimentations are mostly translated into empirical correlations to predict Nusselt number and pressure drop in the mentioned fin configurations.

For simulation verification of the current study, the circular pin-fin array is selected because of the well-established correlations developed for such fin arrays by Zukauskas [137]. These correlations are well-known and have been practically used in heat exchanger design for almost half a century. Since the methodology of CFD analysis is identical for all of the heatsink design candidates, once we gain confidence in the CFD result of the circular design, we can ensure that the results for other candidates are also reliable. Even though the simulation verification is confined to the baseline circular case in this study, the design with offset strip fins can also be verified against the correlations of Manglik and Bergles [111].

The empirical correlations specify pressure drop and nusselt number for an array of tube bundles where the tube length is assumed to very long compared to the tube diameter. Therefore end-wall effects are neglected. As mentioned earlier, it has been

shown that in high Reynolds number, end-wall effects become insignificant; therefore, the correlations will be able to sufficiently capture the physics. Nusselt number and pressure drop correlations are adapted from [137] :

$$\overline{Nu}_D = C_1 Re^m_{D,\max} Pr^{0.36} \left(\frac{Pr}{Pr_s}\right)^{1/4} \tag{5.8.1}$$

The latter equation is valid under the following conditions:

$$N_L \geq 20$$
$$0.7 \leq Pr \leq 500 \tag{5.8.2}$$
$$10 \leq Re_{D,\max} \leq 2 \times 10^6$$

Where:

$$Re_{D,\max} \equiv \rho V_{\max} D/\mu \tag{5.8.3a}$$
$$V_{\max} = \frac{S_T}{S_T - D} V \tag{5.8.3b}$$
$$\overline{Nu}_D = \frac{\overline{h}D}{k} \tag{5.8.3c}$$

Constants C_1 and m in equation 5.8.1 are functions of array geometry and local Reynolds number. For stagerred tube banks in the range Reynolds numbers available in this study $C_1 = 0.35(\frac{S_T}{S_L})^{1/5}$ and $m = 0.6$. The total power dissipation can be obtained from the following equation:

$$Q = \dot{m}c_p(T_o - T_i) = \overline{h}A_s \Delta T_{lm} \tag{5.8.4}$$

Where log mean temperature difference is defined by:

$$\Delta T_{1m} = \frac{(T_s - T_i) - (T_s - T_o)}{\ln(\frac{T_s - T_i}{T_s - T_o})} \tag{5.8.5}$$

V_{max} is known at each flow rate. Using V_{max} along with fluid properties at arithmetic mean temperature of the fluid in equation 5.8.3 we can obtain the local Reynolds number. By substituting the local Reynolds number in equation 5.8.1 we can obtain the average nusselt number on the surface. It should be noted that Pr number should be computed at the arithmetic mean temperature of the fluid, whereas Pr_s must be computed at the surface temperature. Q, T_i, T_o, are known at each flow rate and T_s is unknown. Therefore, an initial guess of surface temperature must be made in order to calculate the nusselt number. After obtaining the nusselt number, the average heat transfer coefficient $(\overline{h})$ will be known. By substituting $\overline{h}$ in equation 5.8.4 we can obtain the surface temperature. The obtained surface temperature does not necessarily match with the initial guess. Therefore, the same process should be done repeatedly until T_s will be obtained with acceptable convergence criteria. This process is programmed in a Matlab script, and the final results are summarized in table 5.6. As seen from the values, the results are in perfect agreement with the empirically-derived correlations. The relative deviation of surface temperature from empirically-derived correlations and CFD results is less than 1%. As a matter of fact, the surface temperature obtained from Zukauskas's correlation is less than the one obtained from CFD. This can be attributed to the fact that end-wall effects are not considered in the correlations. The no-slip condition will slow down the flow adjacent to the end-wall, which eventually decreases the heat transfer coefficient compared to the tube bundle situation. Thus, it was quite expected to have a higher surface

Table 5.6: Verification of simulation results against available empirical correlations

	Flow rate (lpm)	6	8	10	12	14
	$Re_{D,max}$	1374	1779	2184	2592	2990
Δp (Pa)	Empirical	2895	4973	7535	10669	14167
	CFD	2905	4978	7580	10778	14307
	Deviation (%)	0.3	0.1	0.6	1.0	1.0
T_s (°C)	Empirical	97.1	93.0	90.4	88.6	87.2
	CFD	98.4	94.1	91.3	89.3	87.8
	Deviation (%)	1.3	1.2	0.9	0.8	0.7

;

temperature when incorporating the end-walls.

The pressure drop of the tube bundle array can be obtained from the following empirical relationship:

$$\Delta p = N_L \chi \left(\frac{\rho V_{\max}^2}{2} \right) f \tag{5.8.6}$$

Where f is the friction factor and χ is the correction factor. Both values are functions of array geometry and Reynolds number. The values are taken from [93]. The pressure drop values are listed in table 5.6. As per the tabulated values, the pressure drop from the empirical correlation is less than its value from CFD simulation. The maximum deviation is 1.2%. Even though the values are quite comparable, the slight difference could be attributed to the end-wall effects. As it was expected, when end-walls are modeled, the pressure drop is more than the tube bundle situation.

Chapter 6

Conclusions and Future Work

In this chapter, a summary of the research findings is provided first. The contributions of the present study are outlined afterward. The potential future work of the current research is then highlighted, suggesting some improvements in various directions.

6.1 Summary

A general overview of the state-of-the-art and novel cooling techniques is presented in chapter two. The advantages and downsides of each cooling technique are critically reviewed. The rationales behind the choice of liquid-cooling are explained. Then an overview of different liquid-cooling techniques is presented. The underlying reasons for the selection of finned-type liquid-cooling are explained. Furthermore, performance metrics of a power module's cooling system in electrified vehicles are thoroughly discussed.

In chapter three, a general classification of various liquid-cooling cold plates is presented. Potential manufacturing techniques are then discussed with a particular

focus on the integrated baseplate cooling. The advantages and disadvantages of each fabrication method are outlined. Lastly, various fabrication methods are compared in terms of prototyping and mass production suitability.

In chapter four, an overview of different fin shapes is presented. Four different design candidates are then selected. The methodology of the comparative analysis is outlined. The steps which are taken to evaluate the performance of the design candidates are highlighted. The theory of the CFD calculation, automotive-specific operating conditions, and boundary conditions are discussed afterward.

This thesis aimed at enhancing the overall performance of a power electronic module's cooling system by integrating different mini pin-fin shapes in the direct cooling fashion. The main objective was met, and four different cases of pin-fin shapes (circular, drop-shaped, symmetric convex lens, and offset strip fins) were compared. The results showed that off-set strip pin-fins proved the best thermal performance. On average, offset strip, drop-shaped, and the convex lens performed 39%, 20%, and 6% better than the baseline design(circular), respectively. When incorporating the effect of the inlet and outlet housing, OSPF, drop-shaped, and convex lens performed 20.7%, 18%, and 8.8% better than the baseline design, respectively. The fact that the offset strip configuration outperforms the circular design is proved to be true [141] as well. This is in line with the power electronics' heatsinks that are in use in electrified vehicles in production. For instance, serpentine channels are employed in Nissan LEAF(MY2012) inverter [5]. Serpentine channels consist of either inline or staggered straight fins, which are housed by serpentine type channels. It should be noted that TPI is not the only figure of merit that must be considered when it comes to power modules in the automotive sector.

The study goes beyond the thermal performance and compares the design candidates in terms of mass and estimated machining cost. Such a collective comparison gives an overall view of the comparative advantage of each design in particular applications where mass and cost are deemed important. The final choice of the geometry depends on the designer's priority system and how much room is there for cost-performance trade-off. The result of the case 1 design is verified using empirical correlations from the literature. The maximum deviation is less than 1% and 1.2% for surface temperature and pressure drop, respectively. The deviation is attributed to the end-wall effects.

6.2   Contributions

There are three main contributions associated with this study: This study is conducted for liquid-cooled power electronic modules in the automotive application. This means that the available liquid, which is a 50% Water Ethylene Glycol mixture(WEG), is used as the cooling agent.

The study focuses on a range of length scales that is very specific to automotive heat sinks (mini-scale pin-fins), whereas numerous studies have been done on microchannels and micro-scale pin fins.

Various design candidates are considered for the comparative analysis. The particular combination of the circular, drop-shaped, symmetric convex lens, and offset strip geometries have not been compared in mini scale as far as the author's understanding. This is a noticeable contribution to what is already available in the literature. Most of the studies compare three design candidates at the most, whereas in this study, four different design candidates are analyzed and compared. The outcome of this study

will provide a broad insight into the pin-fin heat sink design for thermal designers.

The range of the Reynolds number that has been investigated for this study is specifically tailored for the automotive cooling circuits. Such investigation has not been carried out that focuses on this specific range of flow rates and Reynolds numbers. Many studies have only focused on the laminar and transitional flows.

The methodology of the comparative analysis is unique. The hydraulic diameter is kept constant amongst the different design candidates while the fin spacing is the same. We have elaborated on this matter in the methodology section. Such methodology can be used as a framework for thermal designers when assessing the effect of fin geometry on power electronic modules' cooling performance.

The performance evaluation is comprehensive in the sense that both thermal and hydraulic performance is considered as well as the heatsink mass and cost. A new treatment is applied to the Thermal Performance Index (TPI) that incorporates the effect of area enhancement. Such treatment has not been seen in past studies.

6.3   Future Work

The current study could be well expanded in many directions. Each direction will be discussed in a separate subsection.

6.3.1   Transient Thermal Analysis

Transient thermal analysis can be carried out to determine the cooling system's resiliency to transient harsh currents. Simulation-driven cooling system design based on steady-state thermal response aims to conduct away from the maximum power loss.

The maximum power loss is the maximum power that the module may experience in its operating condition. However, power modules usually experience maximum power loss for a short period of time and operate with continuous power loss over extended periods of time. Therefore, steady-state thermal design results in oversized heatsinks. Transient thermal analysis based on the load profile of the power module can eliminate this issue. Load profile of the power module can be obtained for different drive cycles in a system-level vehicle model. This will help in reducing the mass of the heatsink, and tailoring the heatsink for each specific application.

6.3.2   Temperature-Dependent Power loss and Thermal Coupling in CFD calculation

The initial power loss calculation in this study is junction temperature-dependent. However, the maximum power loss at the steady-state condition is used for the CFD analysis. A temperature-dependent power loss model can be applied in the CFD simulation. This will help with transient simulation where the junction temperature variation significantly affects the loss profile. However, when operating with a high-temperature coolant when the junction temperature is quite high, the junction temperature and loss coupling is loose.

6.3.3   Data Reduction Using Reduced Order Models

Reduced-order models such as lumped parameter thermal networks (e.g., Foster or Cauer network) can be obtained from CFD simulation data using curve fitting. Fast electrothermal models are real-time implementable and ideal for integration to the control algorithm of the module. Such models are capable of capturing the junction

temperature fluctuations due to load profile. Thus, they are beneficial for evaluating the reliability and lifetime of the module.

6.3.4   System-level Modeling of the Vehicle Thermal Management System

The current study is focused on the component-level analysis of the power electronic modules' cooling system. However, with the aid of reduced order thermal models such as lumped parameter thermal network, system-level modeling of the vehicle's entire thermal management system can be carried out. Doing such a system-level study is beneficial from many points of views. First and foremost, it will provide useful information about the system's performance difference due to seasonal fluctuations in ambinet temperature. Secondly, by incorporating the characteristic curve of the water pump into the model, we will be able to directly see the effect of different heat sink designs on the operating point of the pump.

6.3.5   Investigation of Other Fin Shapes

Other fin shapes, such as hydrofoil, elliptical shapes, and etc., can be added to the current investigation to provide a more comprehensive overview of the fin's shape effect on thermal performance. Such investigation has not been done for the range of flow rates and Reynolds numbers in this particular application.

6.3.6   Optimization of Fin Array

There are significant opportunities for optimization of fin array. As mentioned earlier, the objective of the current study was to present a framework for initial assessment of various fin shapes. This initial assessment will give the thermal designer an idea as to which fin shape is the best choice for a certain design. However, this initial evaluation does not necessarily introduce the optimal fin array. Significant amount of research has been dedicated to the tools and methods that are available for optimization of heat sinks [142]. Moving forward, the fin array optimization is an important step in finalizing the heat sink design.

6.3.7   Experimental Validation

Thermal Hydraulic Testing of the Heatsink

The numerical result of the comparative analysis could be further analyzed and validated using experimental studies.

Thermo-mechanical Testing of Additive-Manufactured Heatsink Samples

Experimental studies are required to understand the trade-off between the mechanical and thermal properties of an AM heatsink sample. Particularly the trade-off between the effect of heat treatment on thermal conductivity and hardness is deemed important in this study as discussed in 3.3.4.

6.3.8   Heatsink Design Approach

The current approach of simulation-driven heatsink design has been practiced for decades now. Despite the proven capability of the current approach, it has some major drawbacks. First and foremost, the current heatsink design approach is driven by intuition and the thermal designers' experience. The design process is highly iterative in nature and is based on trial and error. The human effort for coming up with an improved version of the design is a bottleneck. The new iteration must be evaluated again, and this iterative nature makes the entire design process very time-consuming. Heatsink optimization processes have been done on a case-by-case basis, while each technique has been tailored for a specific problem. There is a need for a powerful tool for heatsink design that could minimize the human effort and let the machine decide how the heatsink should evolve to obtain optimal performance.

Topology optimization (TO) was first introduced by Bendsøe and Kikuchi in 1998 in the field of structural mechanics. TO was trying to answer a basic question: how to place material within a predefined design domain to obtain the best stiffness with a certain amount of mass. Later on, the concept found its way to other fields of study, such as fluid flow and heat transfer. TO in conjugate heat transfer (CHT) problem is an effort to answer this fundamental question: how to place solid material and convective material (fluid) in a predefined domain so that we achieve the optimal heat transfer with a certain amount of conductive (solid) material. Despite the maturity of TO in structural design problems, it is yet rather immature in fluid mechanics problems to [143]. The underlying reason for that is the lack of enough computational resources to be able to do iterative design and CFD analysis. Sigmund and Maute in [144] present a comprehensive critical review on topology optimization approaches and

their strength and downsides. One of the burdens of TO application in heatsink design has been the manufacturability of the resulting complex optimal geometries. However, recent developments in metal 3D-printing technologies have provided a significant opportunity for TO to become a widely used engineering tool for designing optimal heat transfer systems [143].

Some of the studies that have been done on TO on liquid-cooling CHT problems in the past decade are summarized in table 6.1. It can be seen that the implementation of such studies is done using a customized code along with a FEM tool to solve the CHT problem in each step. Some of the widely-used TO methods that have been employed in these studies are Method of Moving Asymptotes (MMA), Globally Convergent MMA (GCMMA), Level-Set Method (LSM), Sequential Linear Programming (SLP), and Genetic Algorithm (GA).

Many TO studies have only focused on fluid flow or heat conduction problems. Dbouk in his literature survey, demonstrated that only 23% of the TO studies for optimal heat transfer systems have focused on conjugate heat transfer problems [143]. Out of these studies, only a small fraction of them have focused on turbulent flow simulation, whereas many studies have considered laminar flows due to low computational penalty. Due to the increasing power of computational resources, it is expected that in the not-too-distant future, the potential of TO techniques will be realized in conjugate heat transfer problem with turbulent flows. Therefore, another potential future work is to explore the possibilities of using TO in heatsink design with High-Performance-Computing (HPC) aid.

Table 6.1: Summary of some studies on liquid-cooling heatsink design using TO

Source	Year of Publication	Application	Numerical Simulation/ Experimentation	Optimization Algorithm	Tools/softwares used for TO	Manufacturing Method
Dede et al. [145]	2009	Electric Machines heatsinking	Numerical simulation	Method of Moving Asymptotes (MMA)	Comsol Multiphysics™ + Matlab™	3D-printing
Koga et al. [146]	2013	Generic Heatsinking	Numerical simulation + Experimental validation	Sequential Linear Programming (SLP)	Matlab™ + Ansys CFX™ for final simulation	EDM + CNC
Yaji et al. [147]	2014	Generic Heatsinking	Numerical simulation	Level-Set Method (LSM)	Not mentioned	3D-printing
Wu et al. [148]	2016	Power electronic (PE) heatsinking (SiC power devices)	Numerical simulation	Genetic Algorithm (GA)	Comsol Multiphysics™	3D-printing
Dokken et al. [149]	2018	Generic processors	Numerical simulation	micro-GA	Ansys Fluent™ + Matlab™	3D-printing
Zeng et al. [150]	2019	Electronics cooling	Numerical simulation + Experimental validation	Globally Convergent Method of Moving Asymptotes (GCMMA)	Comsol Multiphysics™	CNC

References

[1] J. Guo, "Modeling and design of inverters using novel power loss calculation and dc-link current/voltage ripple estimation methods and bus bar analysis," Ph.D. dissertation, McMaster University, 2017. (Cited on pages 1, 61, 63, 64, and 65.)

[2] *Electric Vehicle Outlook 2020*, BloombergNEF, 2020, [Accessed: 2020-12-10]. [Online]. Available: https://bnef.turtl.co/story/evo-2020/page/1 (Cited on pages 1 and 2.)

[3] A. Emadi, *Handbook of automotive power electronics and motor drives*. CRC press, 2017. (Cited on pages 2 and 102.)

[4] *"U.S. Drive Electrical and Electronics Technical Team Roadmap"*, U.S. Department of Energy, 2017, [Accessed: 2020-12-10]. [Online]. Available: https://www.energy.gov/sites/prod/files/2017/11/f39/EETT%20Roadmap%2010-27-17.pdf (Cited on pages 2 and 3.)

[5] J. Reimers, L. Dorn-Gomba, C. Mak, and A. Emadi, "Automotive traction inverters: Current status and future trends," *IEEE Transactions on Vehicular Technology*, vol. 68, no. 4, pp. 3337–3350, 2019. (Cited on pages 2 and 149.)

[6] J. Broughton, V. Smet, R. R. Tummala, and Y. K. Joshi, "Review of thermal packaging technologies for automotive power electronics for traction purposes," *Journal of Electronic Packaging*, vol. 140, no. 4, 2018. (Cited on pages 3, 10, 11, 12, 13, 14, 15, 24, and 70.)

[7] M. Ebadian and C. Lin, "A review of high-heat-flux heat removal technologies," *Journal of heat transfer*, vol. 133, no. 11, 2011. (Cited on pages 3, 12, 18, and 23.)

[8] Y. Wang, S. Jones, A. Dai, and G. Liu, "Reliability enhancement by integrated liquid cooling in power igbt modules for hybrid and electric vehicles," *Microelectronics Reliability*, vol. 54, no. 9-10, pp. 1911–1915, 2014. (Cited on p. 4.)

[9] B. Li, H. Kuo, X. Wang, Y. Chen, Y. Wang, D. Gerada, S. Worall, I. Stone, and Y. Yan, "Thermal Management of Electrified Propulsion System for Low-Carbon Vehicles," *Automotive Innovation*, pp. 299–316, 2020. (Cited on pages 9, 10, 15, and 16.)

[10] S. G. Kandlikar and C. N. Hayner, "Liquid cooled cold plates for industrial high-power electronic devices—thermal design and manufacturing considerations," *Heat transfer engineering*, vol. 30, no. 12, pp. 918–930, 2009. (Cited on pages 12, 38, 39, and 40.)

[11] P. Wang, P. McCluskey, and A. Bar-Cohen, "Two-phase liquid cooling for thermal management of igbt power electronic module," *Journal of Electronic Packaging*, vol. 135, no. 2, 2013. (Cited on pages 12, 14, and 22.)

[12] M. O'Keefe and K. Bennion, "A comparison of hybrid electric vehicle power electronics cooling options," *VPPC 2007 - Proceedings of the 2007 IEEE Vehicle Power and Propulsion Conference*, pp. 116–123, 2007. (Cited on pages 12, 22, and 33.)

[13] G. Wang, P. Cheng, and A. Bergles, "Effects of inlet/outlet configurations on flow boiling instability in parallel microchannels," *International Journal of Heat and Mass Transfer*, vol. 51, no. 9-10, pp. 2267–2281, 2008. (Cited on p. 12.)

[14] S. G. Kandlikar, "Fundamental issues related to flow boiling in minichannels and microchannels," *Experimental Thermal and Fluid Science*, vol. 26, no. 2-4, pp. 389–407, 2002. (Cited on p. 13.)

[15] D. B. Tuckerman and R. F. W. Pease, "High-performance heat sinking for vlsi," *IEEE Electron device letters*, vol. 2, no. 5, pp. 126–129, 1981. (Cited on p. 14.)

[16] C.-K. Liu, Y.-L. Chao, S.-J. Yang, R.-C. Fang, W.-K. Han, J. Tu, A. Lin, M. Yen, and C. Liao, "Direct liquid cooling for igbt power module," in *2014 9th International Microsystems, Packaging, Assembly and Circuits Technology Conference (IMPACT)*.   IEEE, 2014, pp. 41–44. (Cited on p. 14.)

[17] D. Sharar, N. R. Jankowski, and B. Morgan, "Review of two-phase electronics cooling for army vehicle applications," 2010. (Cited on pages 15, 16, and 17.)

[18] G. Natarajan and R. Bezama, "Microjet cooler with distributed returns," *Heat transfer engineering*, vol. 28, no. 8-9, pp. 779–787, 2007. (Cited on p. 15.)

[19] C. Qian, A. M. Gheitaghy, J. Fan, H. Tang, B. Sun, H. Ye, and G. Zhang, "Thermal Management on IGBT Power Electronic Devices and Modules," *IEEE Access*, vol. 6, pp. 12 868–12 884, 2018. (Cited on pages 15, 17, 22, and 25.)

[20] J.-X. Wang, Y.-Z. Li, S.-N. Wang, H.-S. Zhang, X. Ning, and W. Guo, "Experimental investigation of the thermal control effects of phase change material based packaging strategy for on-board permanent magnet synchronous motors," *Energy Conversion and Management*, vol. 123, pp. 232–242, 2016. (Cited on p. 15.)

[21] H. Bostanci, D. Van Ee, B. A. Saarloos, D. P. Rini, and L. C. Chow, "Spray cooling of power electronics using high temperature coolant and enhanced surface," in *2009 IEEE Vehicle Power and Propulsion Conference.* IEEE, 2009, pp. 609–613. (Cited on p. 15.)

[22] S. N. Joshi and E. M. Dede, "Two-phase jet impingement cooling for high heat flux wide band-gap devices using multi-scale porous surfaces," *Applied Thermal Engineering*, vol. 110, pp. 10–17, 2017. (Cited on p. 15.)

[23] P. R. Parida, S. V. Ekkad, and K. Ngo, "Impingement-based high performance cooling configurations for automotive power converters," *International Journal of Heat and Mass Transfer*, vol. 55, no. 4, pp. 834–847, 2012. (Cited on p. 15.)

[24] B. Webb and C.-F. Ma, "Single-phase liquid jet impingement heat transfer," in *Advances in heat transfer.* Elsevier, 1995, vol. 26, pp. 105–217. (Cited on p. 15.)

[25] D.-Y. Lee and K. Vafai, "Comparative analysis of jet impingement and microchannel cooling for high heat flux applications," *International Journal of Heat and Mass Transfer*, vol. 42, no. 9, pp. 1555–1568, 1999. (Cited on pages 15 and 20.)

[26] S. G. Kandlikar and A. V. Bapat, "Evaluation of jet impingement, spray and microchannel chip cooling options for high heat flux removal," *Heat Transfer Engineering*, vol. 28, no. 11, pp. 911–923, 2007. (Cited on pages 16 and 20.)

[27] A. Bhunia and C.-L. Chen, "Jet impingement cooling of an inverter module in the harsh environment of a hybrid vehicle," in *Heat Transfer Summer Conference*, vol. 47349, 2005, pp. 561–567. (Cited on p. 16.)

[28] G. Liang and I. Mudawar, "Review of spray cooling–part 1: Single-phase and nucleate boiling regimes, and critical heat flux," *International Journal of Heat and Mass Transfer*, vol. 115, pp. 1174–1205, 2017. (Cited on p. 17.)

[29] M. Fabbri, S. Jiang, and V. K. Dhir, "A comparative study of cooling of high power density electronics using sprays and microjets," *J. Heat Transfer*, vol. 127, no. 1, pp. 38–48, 2005. (Cited on pages 17 and 19.)

[30] M. Shaw, J. Waldrop, S. Chandrasekaran, B. Kagalwala, X. Jing, E. Brown, V. Dhir, and M. Fabbeo, "Enhanced thermal management by direct water spray of high-voltage, high power devices in a three-phase, 18-hp ac motor drive demonstration," in *ITherm 2002. Eighth Intersociety Conference on Thermal and Thermomechanical Phenomena in Electronic Systems (Cat. No. 02CH37258)*. IEEE, 2002, pp. 1007–1014. (Cited on p. 17.)

[31] I. Mudawar, "Assessment of high-heat-flux thermal management schemes," *IEEE transactions on components and packaging technologies*, vol. 24, no. 2, pp. 122–141, 2001. (Cited on p. 17.)

[32] M. Chyu, C. Yen, and S. Siw, "Comparison of heat transfer from staggered pin fin arrays with circular, cubic and diamond shaped elements," in *Turbo Expo: Power for Land, Sea, and Air*, vol. 47934, 2007, pp. 991–999. (Cited on p. 18.)

[33] L. Meysenc, M. Jylhakallio, and P. Barbosa, "Power electronics cooling effectiveness versus thermal inertia," *IEEE Transactions on Power Electronics*, vol. 20, no. 3, pp. 687–693, 2005. (Cited on pages 20 and 36.)

[34] A. G. Pautsch, A. Gowda, L. Stevanovic, and R. Beaupre, "Double-sided microchannel cooling of a power electronics module using power overlay," in *International Electronic Packaging Technical Conference and Exhibition*, vol. 43604, 2009, pp. 427–436. (Cited on p. 22.)

[35] I. Mudawar, D. Bharathan, K. Kelly, and S. Narumanchi, "Two-phase spray cooling of hybrid vehicle electronics," *IEEE Transactions on Components and Packaging Technologies*, vol. 32, no. 2, pp. 501–512, 2009. (Cited on p. 22.)

[36] A. Bhunia, S. Chandrasekaran, and C.-L. Chen, "Performance improvement of a power conversion module by liquid micro-jet impingement cooling," *IEEE Transactions on Components and Packaging Technologies*, vol. 30, no. 2, pp. 309–316, 2007. (Cited on p. 22.)

[37] M. Pais, L. Chow, and E. Mahefkey, "Surface roughness and its effects on the heat transfer mechanism in spray cooling," 1992. (Cited on p. 23.)

[38] I. Silverman, A. Yarin, S. Reznik, A. Arenshtam, D. Kijet, and A. Nagler, "High heat-flux accelerator targets: Cooling with liquid metal jet impingement," *International journal of heat and mass transfer*, vol. 49, no. 17-18, pp. 2782–2792, 2006. (Cited on p. 23.)

[39] H. Hirshfeld, I. Silverman, A. Arenshtam, D. Kijel, and A. Nagler, "High heat flux cooling of accelerator targets with micro-channels," *Nuclear Instruments and Methods in Physics Research Section A: Accelerators, Spectrometers, Detectors and Associated Equipment*, vol. 562, no. 2, pp. 903–905, 2006. (Cited on p. 23.)

[40] S. Narumanchi, M. Mihalic, K. Kelly, and G. Eesley, "Thermal interface materials for power electronics applications," in *2008 11th Intersociety Conference on Thermal and Thermomechanical Phenomena in Electronic Systems*. IEEE, 2008, pp. 395–404. (Cited on p. 24.)

[41] S. Yin, T. Wang, K.-J. Tseng, J. Zhao, and X. Hu, "Electro-thermal modeling of sic power devices for circuit simulation," in *IECON 2013-39th Annual Conference of the IEEE Industrial Electronics Society*. IEEE, 2013, pp. 718–723. (Cited on p. 26.)

[42] O. Alavi, M. Abdollah, and A. H. Viki, "Assessment of thermal network models for estimating igbt junction temperature of a buck converter," in *2017 8th Power Electronics, Drive Systems & Technologies Conference (PEDSTC)*. IEEE, 2017, pp. 102–107. (Cited on p. 26.)

[43] P. Azer, R. Rodriguez, H. Ge, J. Bauman, P. S. Ravi, and A. Emadi, "Time efficient integrated electro-thermal model for bidirectional synchronous dc-dc

converter in hybrid electric vehicles," in *2018 IEEE Transportation Electrification Conference and Expo (ITEC)*.   IEEE, 2018, pp. 55–62. (Cited on p. 26.)

[44] L. Zhou, J. Wu, P. Sun, and X. Du, "Junction temperature management of igbt module in power electronic converters," *Microelectronics Reliability*, vol. 54, no. 12, pp. 2788–2795, 2014. (Cited on pages 26 and 35.)

[45] B. R. Munson, T. H. Okiishi, W. W. Huebsch, and A. P. Rothmayer, *Fluid mechanics.*   Wiley Singapore, 2013. (Cited on pages 28, 76, 77, 97, and 98.)

[46] B. E. Short Jr, P. E. Raad, and D. C. Price, "Performance of pin fin cast aluminum coldwalls, part 1: Friction factor correlations," *Journal of Thermophysics and Heat Transfer*, vol. 16, no. 3, pp. 389–396, 2002. (Cited on p. 29.)

[47] E. M. Sparrow and S. Kang, "Longitudinally-finned cross-flow tube banks and their heat transfer and pressure drop characteristics," *International journal of heat and mass transfer*, vol. 28, no. 2, pp. 339–350, 1985. (Cited on p. 29.)

[48] B. E. Short Jr, D. C. Price, and P. E. Raad, "Design of cast pin fin coldwalls for air-cooled electronics systems," *J. Electron. Packag.*, vol. 126, no. 1, pp. 67–73, 2004. (Cited on p. 29.)

[49] S. Lau, Y. Kim, and J. Han, "Local endwall heat/mass transfer in a pin fin channel," *htff*, pp. 64–75, 1987. (Cited on p. 29.)

[50] W. Damerow, J. Murtaugh, and F. Burggraf, "Experimental and analytical investigation of the coolant flow characteristics in cooled turbine airfoils," 1972. (Cited on p. 29.)

[51] D. Metzger, Z. Fan, and W. Shepard, "Pressure loss and heat transfer through multiple rows of short pin fins," in *International Heat Transfer Conference Digital Library*.   Begel House Inc., 1982. (Cited on p. 29.)

[52] M. Jakob, "Heat transfer and flow resistance in cross flow of gases over tube bank," *Trans. ASME*, vol. 60, p. 384, 1938. (Cited on p. 29.)

[53] A. Koşar, C. Mishra, and Y. Peles, "Laminar flow across a bank of low aspect ratio micro pin fins," 2005. (Cited on p. 29.)

[54] Y. Peng, "Heat transfer and friction loss characteristics of pin fin cooling configurations," 1984. (Cited on p. 29.)

[55] J. Armstrong and D. Winstanley, "A review of staggered array pin fin heat transfer for turbine cooling applications," 1988. (Cited on p. 29.)

[56] A. Mohammadi and A. Koşar, "The effect of arrangement type and pitch ratio on the performance of micro-pin-fin heat sinks," *Journal of Thermal Analysis and Calorimetry*, vol. 140, no. 3, pp. 1057–1068, 2020. (Cited on pages 30 and 33.)

[57] T. İzci, M. Koz, and A. Koşar, "The effect of micro pin-fin shape on thermal and hydraulic performance of micro pin-fin heat sinks," *Heat Transfer Engineering*, vol. 36, no. 17, pp. 1447–1457, 2015. (Cited on pages 30, 33, and 73.)

[58] J. Hsu, M. Staunton, and M. Starke, "Barriers to the application of high-temperature coolants in hybrid electric vehicles," Oak Ridge National Laboratory (ORNL), Oak Ridge, TN, Tech. Rep., 2006. (Cited on pages 31 and 101.)

[59] A. Kosar and Y. Peles, "Tcpt-2006-096. r2: Micro scale pin fin heat sinks—parametric performance evaluation study," *IEEE Transactions on Components and Packaging Technologies*, vol. 30, no. 4, pp. 855–865, 2007. (Cited on pages 32, 73, 77, and 78.)

[60] W. Duangthongsuk and S. Wongwises, "A comparison of the thermal and hydraulic performances between miniature pin fin heat sink and microchannel heat sink with zigzag flow channel together with using nanofluids," pp. 3265–3274, 2018. (Cited on p. 32.)

[61] A. Sakanova and K. J. Tseng, "Comparison of pin-fin and finned shape heat sink for power electronics in future aircraft," *Applied Thermal Engineering*, vol. 136, pp. 364–374, 2018. (Cited on pages 33, 73, 77, 78, and 101.)

[62] D. H. Lee, D.-H. Rhee, K. M. Kim, H. H. Cho, and H.-K. Moon, "Heat transfer and flow temperature measurements in a rotating triangular channel with various rib arrangements," *Heat and mass transfer*, vol. 45, no. 12, pp. 1543–1553, 2009. (Cited on p. 33.)

[63] M.-C. Lu and C.-C. Wang, "Effect of the inlet location on the performance of parallel-channel cold-plate," *IEEE Transactions on components and packaging technologies*, vol. 29, no. 1, pp. 30–38, 2006. (Cited on p. 39.)

[64] B. A. Jasperson, Y. Jeon, K. T. Turner, F. E. Pfefferkorn, and W. Qu, "Comparison of micro-pin-fin and microchannel heat sinks considering thermal-hydraulic performance and manufacturability," *IEEE Transactions on Components and Packaging Technologies*, vol. 33, no. 1, pp. 148–160, 2009. (Cited on pages 43, 44, 46, 47, 49, 51, 58, 138, and 142.)

[65] M. P. Groover, *Fundamentals of modern manufacturing: materials, processes, and systems.* John Wiley & Sons, 2020. (Cited on pages 43, 44, 45, 46, 47, 49, 50, and 51.)

[66] G. Baumeister, R. Ruprecht, and J. Hausselt, "Microcasting of parts made of metal alloys," *Microsystem Technologies*, vol. 10, no. 3, pp. 261–264, 2004. (Cited on p. 44.)

[67] S. Chung, S. Park, I. Lee, H. Jeong, and D. Cho, "Replication techniques for a metal microcomponent having real 3d shape by microcasting process," *Microsystem Technologies*, vol. 11, no. 6, pp. 424–428, 2005. (Cited on p. 44.)

[68] G. Baumeister, K. Mueller, R. Ruprecht, and J. Hausselt, "Production of metallic high aspect ratio microstructures by microcasting," *Microsystem technologies*, vol. 8, no. 2-3, pp. 105–108, 2002. (Cited on p. 44.)

[69] G. Fu, N. Loh, S. Tor, B. Tay, Y. Murakoshi, and R. Maeda, "Injection molding, debinding and sintering of 316l stainless steel microstructures," *Applied Physics A*, vol. 81, no. 3, pp. 495–500, 2005. (Cited on p. 46.)

[70] C. S. Lin, Y. S. Liao, and S. T. Chen, "Development of a novel micro wire-edm mechanism for the fabricating of micro parts," in *Materials science forum*, vol. 505. Trans Tech Publ, 2006, pp. 235–240. (Cited on p. 49.)

[71] D. Herzog, V. Seyda, E. Wycisk, and C. Emmelmann, "Additive manufacturing of metals," *Acta Materialia*, vol. 117, pp. 371–392, 2016. (Cited on pages 52 and 53.)

[72] T. Kimura, T. Nakamoto, M. Mizuno, and H. Araki, "Effect of silicon content on densification, mechanical and thermal properties of al-xsi binary alloys fabricated using selective laser melting," *Materials Science and Engineering: A*, vol. 682, pp. 593–602, 2017. (Cited on p. 52.)

[73] T. D. Ngo, A. Kashani, G. Imbalzano, K. T. Nguyen, and D. Hui, "Additive manufacturing (3d printing): A review of materials, methods, applications and challenges," *Composites Part B: Engineering*, vol. 143, pp. 172–196, 2018. (Cited on p. 53.)

[74] T. Wu, A. A. Wereszczak, H. Wang, B. Ozpineci, and C. W. Ayers, "Thermal response of additive manufactured aluminum," in *2016 International Symposium on 3D Power Electronics Integration and Manufacturing (3D-PEIM)*. IEEE, 2016, pp. 1–15. (Cited on pages 53 and 56.)

[75] M. Chinthavali, C. Ayers, S. Campbell, R. Wiles, and B. Ozpineci, "A 10-kw sic inverter with a novel printed metal power module with integrated cooling using additive manufacturing," in *2014 IEEE Workshop on Wide Bandgap Power Devices and Applications*. IEEE, 2014, pp. 48–54. (Cited on pages 53, 55, and 103.)

[76] N. T. Aboulkhair, I. Maskery, C. Tuck, I. Ashcroft, and N. M. Everitt, "The microstructure and mechanical properties of selectively laser melted alsi10mg: The effect of a conventional t6-like heat treatment," *Materials Science and Engineering: A*, vol. 667, pp. 139–146, 2016. (Cited on pages 54 and 55.)

[77] K. Kempen, L. Thijs, J. Van Humbeeck, and J.-P. Kruth, "Mechanical properties of alsi10mg produced by selective laser melting," *Physics Procedia*, vol. 39, pp. 439–446, 2012. (Cited on p. 54.)

[78] L. Thijs, K. Kempen, J.-P. Kruth, and J. Van Humbeeck, "Fine-structured aluminium products with controllable texture by selective laser melting of pre-alloyed alsi10mg powder," *Acta Materialia*, vol. 61, no. 5, pp. 1809–1819, 2013. (Cited on p. 55.)

[79] N. T. Aboulkhair, M. Simonelli, L. Parry, I. Ashcroft, C. Tuck, and R. Hague, "3d printing of aluminium alloys: Additive manufacturing of aluminium alloys using selective laser melting," *Progress in materials science*, vol. 106, p. 100578, 2019. (Cited on p. 55.)

[80] W. Li, S. Li, J. Liu, A. Zhang, Y. Zhou, Q. Wei, C. Yan, and Y. Shi, "Effect of heat treatment on alsi10mg alloy fabricated by selective laser melting: Microstructure evolution, mechanical properties and fracture mechanism," *Materials Science and Engineering: A*, vol. 663, pp. 116–125, 2016. (Cited on p. 55.)

[81] N. T. Aboulkhair, C. Tuck, I. Ashcroft, I. Maskery, and N. M. Everitt, "On the precipitation hardening of selective laser melted alsi10mg," *Metallurgical and Materials Transactions A*, vol. 46, no. 8, pp. 3337–3341, 2015. (Cited on p. 55.)

[82] *HybridPACK ™ Drive Module Final Data Sheet*, Infineon Technologies AG, 2017. (Cited on p. 61.)

[83] N. Y. Shammas, "Present problems of power module packaging technology," *Microelectronics reliability*, vol. 43, no. 4, pp. 519–527, 2003. (Cited on p. 66.)

[84] M. Held, P. Jacob, G. Nicoletti, P. Scacco, and M.-H. Poech, "Fast power cycling test of igbt modules in traction application," in *Proceedings of Second International Conference on Power Electronics and Drive Systems*, vol. 1.   IEEE, 1997, pp. 425–430. (Cited on p. 66.)

[85] C. Chen, F. Luo, and Y. Kang, "A review of sic power module packaging: Layout, material system and integration," *CPSS Transactions on Power Electronics and Applications*, vol. 2, no. 3, pp. 170–186, 2017. (Cited on pages 67 and 68.)

[86] J. Lutz, "Packaging and reliability of power modules," in *CIPS 2014; 8th International Conference on Integrated Power Electronics Systems*.   VDE, 2014, pp. 1–8. (Cited on pages 67 and 70.)

[87] B. Bilgin, P. Magne, P. Malysz, Y. Yang, V. Pantelic, M. Preindl, A. Korobkine, W. Jiang, M. Lawford, and A. Emadi, "Making the case for electrified transportation," *IEEE Transactions on Transportation Electrification*, vol. 1, no. 1, pp. 4–17, 2015. (Cited on p. 68.)

[88] Y. Yang, L. Dorn-Gomba, R. Rodriguez, C. Mak, and A. Emadi, "Automotive power module packaging: Current status and future trends," *IEEE Access*, vol. 8, pp. 160 126–160 144, 2020. (Cited on p. 68.)

[89] K. R. Choudhury and D. J. Rogers, "Steady-state thermal modeling of a power module: An n-layer fourier approach," *IEEE Transactions on Power Electronics*, vol. 34, no. 2, pp. 1500–1508, 2018. (Cited on pages 69 and 70.)

[90] E. M. Dede, "Optimization and design of a multipass branching microchannel heat sink for electronics cooling," *Journal of Electronic Packaging*, vol. 134, no. 4, 2012. (Cited on p. 70.)

[91] D. Kusano, G. Tanabe, H. Hyuga, Y. Zhou, and K. Hirao, "High thermal conductivity silicon nitride substrates for power semiconductor applications," in *PCIM Europe 2016; International Exhibition and Conference for Power Electronics, Intelligent Motion, Renewable Energy and Energy Management*. VDE, 2016, pp. 1–8. (Cited on p. 70.)

[92] D. R. Askeland, P. P. Phulé, W. J. Wright, and D. Bhattacharya, "The science and engineering of materials," 2003. (Cited on p. 70.)

[93] T. L. Bergman, F. P. Incropera, A. S. Lavine, and D. P. DeWitt, *Introduction to heat transfer*. John Wiley & Sons, 2011. (Cited on pages 72 and 147.)

[94] N. Drakos, "Mit thermodynamics notes, heat exchangers," 2002, [Accessed: 2020-11-25]. [Online]. Available: https://web.mit.edu/16.unified/www/FALL/thermodynamics/notes/node131.html (Cited on p. 72.)

[95] A. Abdoli, G. Jimenez, and G. S. Dulikravich, "Thermo-fluid analysis of micro pin-fin array cooling configurations for high heat fluxes with a hot spot," *International Journal of Thermal Sciences*, vol. 90, pp. 290–297, 2015. (Cited on pages 73, 76, 78, and 144.)

[96] Q. Li, Z. Chen, U. Flechtner, and H.-J. Warnecke, "Heat transfer and pressure drop characteristics in rectangular channels with elliptic pin fins," *International Journal of Heat and Fluid Flow*, vol. 19, no. 3, pp. 245–250, 1998. (Cited on p. 73.)

[97] J. Boulares, "Numerical and experimental study of the performance of a drop-shaped pin fin heat exchanger," NAVAL POSTGRADUATE SCHOOL MONTEREY CA DEPT OF MECHANICAL ENGINEERING, Tech. Rep., 2003. (Cited on pages 74 and 75.)

[98] H. Nabati, "Optimal pin fin heat exchanger surface," Ph.D. dissertation, Mälardalen University, 2008. (Cited on p. 74.)

[99] ManikandanC and PachaiyappanS, "Engineering and Technology (A High Impact Factor," *International Journal of Innovative Research in Science*, vol. 5, no. 2, 2016. (Cited on p. 74.)

[100] Z. Chen, Q. Li, D. Meier, and H. J. Warnecke, "Convective heat transfer and pressure loss in rectangular ducts with drop-shaped pin fins," *Heat and Mass Transfer/Waerme- und Stoffuebertragung*, vol. 33, no. 3, pp. 219–224, 1997. (Cited on pages 74 and 75.)

[101] F. Wang, J. Zhang, and S. Wang, "Investigation on flow and heat transfer characteristics in rectangular channel with drop-shaped pin fins," *Propulsion and Power Research*, vol. 1, no. 1, pp. 64–70, 2012. [Online]. Available: http://dx.doi.org/10.1016/j.jppr.2012.10.003 (Cited on p. 74.)

[102] P. Breeze, *Power generation technologies.* Newnes, 2019. (Cited on p. 75.)

[103] S. R. Reddy and G. S. Dulikravich, "Inverse design of cooling of electronic chips subject to specified hot spot temperature and coolant inlet temperature," in *International Electronic Packaging Technical Conference and Exhibition*, vol. 56901. American Society of Mechanical Engineers, 2015, p. V003T10A019. (Cited on pages 76, 79, and 144.)

[104] S. R. Reddy, A. Abdoli, G. S. Dulikravich, C. C. Pacheco, G. Vasquez, R. Jha, M. J. Colaco, and H. R. Orlande, "Multi-objective optimization of micro pin-fin arrays for cooling of high heat flux electronics with a hot spot," *Heat Transfer Engineering*, vol. 38, no. 14-15, pp. 1235–1246, 2017. (Cited on pages 76, 79, and 144.)

[105] D. Yang, Z. Jin, Y. Wang, G. Ding, and G. Wang, "Heat removal capacity of laminar coolant flow in a micro channel heat sink with different pin fins," *International Journal of Heat and Mass Transfer*, vol. 113, pp. 366–372, 2017. (Cited on pages 77, 78, 79, and 144.)

[106] S. Ndao, Y. Peles, and M. K. Jensen, "Effects of pin fin shape and configuration on the single-phase heat transfer characteristics of jet impingement on micro pin fins," *International Journal of Heat and Mass Transfer*, vol. 70, pp. 856–863, 2014. (Cited on p. 77.)

[107] ——, "Effects of pin fin shape and configuration on the single-phase heat transfer characteristics of jet impingement on micro pin fins," *International Journal of Heat and Mass Transfer*, vol. 70, pp. 856–863, 2014. (Cited on p. 77.)

[108] A. Koşar and Y. Peles, "Boiling heat transfer in a hydrofoil-based micro pin fin heat sink," *International Journal of Heat and Mass Transfer*, vol. 50, no. 5-6, pp. 1018–1034, 2007. (Cited on pages 77 and 78.)

[109] "Lenses — Boundless Physics," [Accessed: 2020-12-04]. [Online]. Available: https://courses.lumenlearning.com/boundless-physics/chapter/lenses/ (Cited on p. 78.)

[110] L. B. Erbay, M. M. Öztürk, and B. Doğan, "Comprehensive study of compact heat exchangers with offset strip fin," *Heat Exchangers: Advanced Features and Applications*, p. 31, 2017. (Cited on p. 79.)

[111] R. M. Manglik and A. E. Bergles, "Heat transfer and pressure drop correlations for the rectangular offset strip fin compact heat exchanger," *Experimental Thermal and Fluid Science*, vol. 10, no. 2, pp. 171–180, 1995. (Cited on pages 80 and 144.)

[112] M. Wong, I. Owen, C. J. Sutcliffe, and A. Puri, "Convective heat transfer and pressure losses across novel heat sinks fabricated by Selective Laser Melting," *International Journal of Heat and Mass Transfer*, vol. 52, no. 1-2, pp. 281–288, 2009. [Online]. Available: http://dx.doi.org/10.1016/j.ijheatmasstransfer.2008.06.002 (Cited on p. 80.)

[113] A. Miremadi, A. Mehdizadeh, M. Arjomandi, S. Al-Sarawi, M. Kahrom, B. Dally, and D. Abbott, "Taguchi based performance analysis of an offset strip fin heat sink," 2010. (Cited on p. 80.)

[114] G. J. Michna, A. M. Jacobi, and R. L. Burton, "Friction factor and heat transfer performance of an offset-strip fin array at air-side reynolds numbers to 100,000," 2006. (Cited on p. 80.)

[115] F. Hong and P. Cheng, "Three dimensional numerical analyses and optimization of offset strip-fin microchannel heat sinks," *International Communications in Heat and Mass Transfer*, vol. 36, no. 7, pp. 651–656, 2009. (Cited on p. 80.)

[116] A. VYAS and A. B. Agrawal, "Offset-strip fin heat exchangers a conceptual review study," *International Journal of Engineering Research and Applications*, vol. 3, no. 1, pp. 1306–1312, 2013. (Cited on p. 80.)

[117] A. Yahyaee, A. S. Bahman, and F. Blaabjerg, "A modification of offset strip fin heatsink with high-performance cooling for IGBT modules," *Applied Sciences (Switzerland)*, vol. 10, no. 3, pp. 1–15, 2020. (Cited on pages 80, 117, and 118.)

[118] *AN-HPD-ASSEMBLY, HybridPACK ™ Drive*, Infineon Technologies AG, 2018. (Cited on p. 92.)

[119] D. Nikushchenko and V. Pavlovsky, "Fluid motion equations in tensor form," in *Advances on Tensor Analysis and their Applications.* IntechOpen, 2020. (Cited on pages 97 and 98.)

[120] *Ansys fluent theory guide*, ANSYS Inc., U.S.A., 2020. (Cited on p. 100.)

[121] A. A. Sonin, "Equation of motion for viscous fluids," 2001. (Cited on p. 101.)

[122] J. Ye, K. Yang, H. Ye, and A. Emadi, "A fast electro-thermal model of traction inverters for electrified vehicles," *IEEE Transactions on Power Electronics*, vol. 32, no. 5, pp. 3920–3934, 2016. (Cited on p. 101.)

[123] B. Bilgin and A. Emadi, "Electric motors in electrified transportation: A step toward achieving a sustainable and highly efficient transportation system," *IEEE Power Electronics Magazine*, vol. 1, no. 2, pp. 10–17, 2014. (Cited on p. 101.)

[124] C.-W. Park and A. K. Jaura, "Thermal analysis of cooling system in hybrid electric vehicles," SAE Technical Paper, Tech. Rep., 2002. (Cited on p. 101.)

[125] A. Lajunen, Y. Yang, and A. Emadi, "Recent developments in thermal management of electrified powertrains," *IEEE Transactions on Vehicular Technology*, vol. 67, no. 12, pp. 11 486–11 499, 2018. (Cited on pages 101 and 102.)

[126] H. Ye, Y. Yang, and A. Emadi, "Traction inverters in hybrid electric vehicles," in *2012 IEEE Transportation Electrification Conference and Expo (ITEC)*. IEEE, 2012, pp. 1–6. (Cited on p. 102.)

[127] R. Bayerer, "Advanced packaging yields higher performance and reliability in power electronics," *Microelectronics Reliability*, vol. 50, no. 9-11, pp. 1715–1719, 2010. (Cited on p. 102.)

[128] P. Ning, Z. Liang, and F. Wang, "Power module and cooling system thermal performance evaluation for hev application," *IEEE Journal of Emerging and Selected Topics in Power Electronics*, vol. 2, no. 3, pp. 487–495, 2014. (Cited on pages 102 and 103.)

[129] H. Hamut, I. Dincer, and G. Naterer, "Performance assessment of thermal management systems for electric and hybrid electric vehicles," *International Journal of Energy Research*, vol. 37, no. 1, pp. 1–12, 2013. (Cited on p. 103.)

[130] T. Kiss, J. Lustbader, and D. Leighton, "Modeling of an electric vehicle thermal management system in matlab/simulink," SAE Technical Paper, Tech. Rep., 2015. (Cited on p. 103.)

[131] S. Narumanchi, M. Mihalic, G. Moreno, and K. Bennion, "Design of lightweight, single-phase liquid-cooled heat exchanger for automotive power electronics," in *13th InterSociety Conference on Thermal and Thermomechanical Phenomena in Electronic Systems*. IEEE, 2012, pp. 693–699. (Cited on p. 103.)

[132] F. R. Menter, "Two-equation eddy-viscosity turbulence models for engineering applications," *AIAA journal*, vol. 32, no. 8, pp. 1598–1605, 1994. (Cited on p. 108.)

[133] F. Menter, "Zonal two equation kw turbulence models for aerodynamic flows," in *23rd fluid dynamics, plasmadynamics, and lasers conference*, 1993, p. 2906. (Cited on p. 108.)

[134] F. R. Menter, M. Kuntz, and R. Langtry, "Ten years of industrial experience with the sst turbulence model," *Turbulence, heat and mass transfer*, vol. 4, no. 1, pp. 625–632, 2003. (Cited on p. 108.)

[135] "The menter shear stress transport turbulence model, nasa turbulence modeling resource," [Accessed: 2020-12-20]. [Online]. Available: https://turbmodels.larc.nasa.gov/sst.html (Cited on p. 108.)

[136] P. J. Roache, "Perspective: a method for uniform reporting of grid refinement studies," *Journal of Fluids Engineering*, 1994. (Cited on p. 118.)

[137] A. Žukauskas, "Heat transfer from tubes in crossflow," in *Advances in heat transfer*. Elsevier, 1972, vol. 8, pp. 93–160. (Cited on pages 144 and 145.)

[138] A. Zukauskas and R. Ulinskas, "Heat transfer in tube banks in crossflow," 1988. (Cited on p. 144.)

[139] D. Metzger, R. Berry, and J. Bronson, "Developing heat transfer in rectangular ducts with staggered arrays of short pin fins," 1982. (Cited on p. 144.)

[140] W. M. Kays, A. L. London, and E. Eckert, "Compact heat exchangers," 1960. (Cited on p. 144.)

[141] S. Ndao, Y. Peles, and M. K. Jensen, "Multi-objective thermal design optimization and comparative analysis of electronics cooling technologies," *International Journal of Heat and Mass Transfer*, vol. 52, no. 19-20, pp. 4317–4326, 2009. (Cited on p. 149.)

[142] H. E. Ahmed, B. H. Salman, A. S. Kherbeet, and M. I. Ahmed, "Optimization of thermal design of heat sinks: A review," *International Journal of Heat and Mass Transfer*, vol. 118, pp. 129–153, 2018. [Online]. Available: https://doi.org/10.1016/j.ijheatmasstransfer.2017.10.099 (Cited on p. 154.)

[143] T. Dbouk, "A review about the engineering design of optimal heat transfer systems using topology optimization," *Applied Thermal Engineering*, vol. 112, pp. 841–854, 2017. (Cited on pages 155 and 156.)

[144] O. Sigmund and K. Maute, "Topology optimization approaches," *Structural and Multidisciplinary Optimization*, vol. 48, no. 6, pp. 1031–1055, 2013. (Cited on p. 155.)

[145] E. M. Dede, "Multiphysics topology optimization of heat transfer and fluid flow systems," in *proceedings of the COMSOL Users Conference*, 2009. (Cited on p. 157.)

[146] A. A. Koga, E. C. C. Lopes, H. F. V. Nova, C. R. De Lima, and E. C. N. Silva, "Development of heat sink device by using topology optimization," *International Journal of Heat and Mass Transfer*, vol. 64, pp. 759–772, 2013. (Cited on p. 157.)

[147] K. Yaji, T. Yamada, S. Kubo, K. Izui, and S. Nishiwaki, "A topology optimization method for a coupled thermal–fluid problem using level set boundary expressions," *International Journal of Heat and Mass Transfer*, vol. 81, pp. 878–888, 2015. (Cited on p. 157.)

[148] T. Wu, B. Ozpineci, and C. Ayers, "Genetic algorithm design of a 3d printed heat sink," in *2016 IEEE Applied Power Electronics Conference and Exposition (APEC)*. IEEE, 2016, pp. 3529–3536. (Cited on p. 157.)

[149] C. B. Dokken and B. M. Fronk, "Optimization of 3d printed liquid cooled heat sink designs using a micro-genetic algorithm with bit array representation," *Applied Thermal Engineering*, vol. 143, pp. 316–325, 2018. (Cited on p. 157.)

[150] S. Zeng and P. S. Lee, "Topology optimization of liquid-cooled microchannel heat sinks: An experimental and numerical study," *International Journal of Heat and Mass Transfer*, vol. 142, p. 118401, 2019. (Cited on p. 157.)